UNIVERSITY OF CALGARY

Photonic Entanglement for a Quantum Repeater

by

Jeongwan Jin

A THESIS

SUBMITTED TO THE FACULTY OF GRADUATE STUDIES

IN PARTIAL FULFILLMENT OF THE REQUIREMENTS FOR THE

DEGREE OF DOCTOR OF PHILOSOPHY

DEPARTMENT OF PHYSICS AND ASTRONOMY

CALGARY, ALBERTA

JULY, 2014

Abstract

Quantum Key Distribution (QKD) has opened a new avenue for secure communication, by allowing one to distribute a random secret key between two users that are connected through a public channel without revealing information to unauthorized parties. If a message is encrypted with the one time pad (a well-known crytography algorithm) using secret keys created by QKD, then the ciphertext is information-theoretically secure and thus unbreakable for adversaries. Despite its unprecedented security, loss in the physical channel has prevented QKD from being used over distances beyond a few hundred kilometers. Fortunately, quantum repeaters have opened a path for long-distance QKD by providing a means to establish entanglement between distant users.

The goal of this thesis has been to develop a source of entangled photon pairs that is suitable for quantum repeaters and then use it to test some of the fundamental building blocks of a quantum repeater : the heralded creation of entangled photons by means of entanglement swapping with properties that allow interfacing with optical quantum memories; the reversible mapping of quantum states from members of entangled photon pairs in and out of solid-state quantum memories; two-photon interference and a Bell state measurement with photons recalled from separate quantum memories. The demonstration of these key ingredients of a quantum repeater constitutes a significant step towards the establishment of entanglement over hundreds of kilometer distance, and hence long-distance QKD.

List of published papers, papers under review, and papers to be submitted

1. "Entanglement swapping with quantum-memory compatible photons", J. Jin, M. G. Puigibert, L. Giner, J. A. Slater, M. R. E. Lamont, V. B. Verma, M. B. Shaw, F. Marsili, S. W. Nam, D. Oblak and W. Tittel, *To be submitted*.

2. "Quantum storage of entangled telecom-wavelength photons in an erbium-doped optical fibre", E. Saglamyurek, J. Jin, V. B. Verma, M. B. Shaw, F. Marsili, S. W. Nam, D. Oblak, and W. Tittel, *Submitted*.

3. "Two-photon interference of weak coherent laser pulses recalled from separate solid-state quantum memories", J. Jin, J. A. Slater, E. Saglamyurek, N. Sinclair, D. Oblak, M. George, R. Ricken, W. Sohler and W. Tittel, *Nature Communications* **4**, 2386 (2013).

4. "Conditional detection of pure quantum states of light after storage in a Tm-doped waveguide", E. Saglamyurek, N. Sinclair, J. Jin, J. A. Slater, D. Oblak, F. Bussières, M. George, R. Ricken, W. Sohler and W. Tittel, *Physical Review Letters*, **108**, 083602 (2012).

5. "Broadband waveguide quantum memory for entangled photons", E. Saglamyurek, N. Sinclair, J. Jin, J. A. Slater, D. Oblak, F. Bussières, M. George, R. Ricken, W. Sohler and W. Tittel, *Nature*, **469** 512 (2011).

6. "Testing nonlocality over 12.4 km of underground fiber with universal time-bin qubit analyzers", F. Bussières, J. A. Slater, J. Jin, N. Godbout and W. Tittel, *Physical Review A*, **81** 052106 (2010).

Table of Contents

List of Tables

List of Figures and Illustrations

List of Symbols and Abbreviations

Symbol	Definition
AFC	Atomic Frequency Comb
AOM	Acousto-Optic Modulator
APD	Avalanche Photodiode
BB84	Bennett, Brassard 1984
BS	Beam Splitter
BSM	Bell-State Measurement
BW	Bandwidth
C	Concurrence
CAR	Coincidence-to-Accidental Ratio
CH	Clauser, Horne
CHSH	Clauser, Horne, Shimony, Holt
CNOT	Controlled NOT
CW	Continuous Wave
DM	Dichroic Mirror
DEMUX	Demultiplexed
EF	Entanglement of Formation
EIT	Electromagnetically Induced Transparency
Er	Erbium
F	Fidelity
FBG	Fiber Bragg Grating
FD	Frequency Doubled
FPF	Fabry Perot Filter
FWHM	Full Width at Half Maximum

GEM	Gradient Echo Memory
HOM	Hong, Ou, Mandel
HWP	Half-Wave Plate
InGaAs	Indium Gallium Arsenide
LOCC	Local Operations and Classical Communication
MEMS	Micro Electro-Mechanical Switches
MUX	Multiplexed
NDF	Neutral Density Filter
OTP	One-Time Pad
PBS	Polarizing Beam Splitter
PC	Polarization Controller
PF	Pass Filter
PPLN	Periodically-Poled Lithium Niobate
PS	Polarization Stabilizer
QED	Quantum Electrodynamics
QKD	Quantum Key Distribution
QPM	Quasi-Phase Matching
QST	Quantum State Tomography
QUBIT	Quantum Bit
QWP	Quarter-Wave Plate
RAM	Random Access Memory
RSA	Rivest, Shamir, Adleman
S	Bell Parameter
SAIT	Southern Alberta Institute of Technology
Si	Silicon
SNR	Signal-to-Noise Ratio

SNSPD	Superconducting Nanowire Single Photon Detector
SPDC	Spontaneous Parametric Down Conversion
TDC	Time-to-Digital Converter
Ti:Tm:LiNbO3	Titanium Thulium Lithium Niobate
Tm	Thulium
TM	Transverse Magnetic
UTBA	Universal Time-Bin Qubit Analyzer
V	Visibility

Chapter 1

Overview

Communication over a public channel without private information being revealed to unauthorized parties is extremely important as our every-day life becomes increasingly dependent upon electronic services, e.g. internet banking or electronic mail. Failure of secure communication can even be a treathening factor for national security in political, military, or diplomatic context. In modern societies, the security of most electronic communication has been guaranteed by a cryptographic protocol named RSA [1]. In two-party communication based on the RSA algorithm, the product of two large prime numbers is used to generate one public and one private key. Once a plaintext is encrypted using the public key and transmitted, the ciphertext will be correctly decrypted only by the private key. There is no known algorithm that, in a feasible amount of time, allows a third party to crack the RSA encryption by finding the private key. Finding the key is related to factoring the prime-number product. For instance, in 2010, a 768-bit RSA module was factored only after 2 years of operations using hundreds of machines [2]. Authors of that paper estimated that it would take 1,500 years to do the same job if a single core 2.2 GHz processor with 2 GB RAM had been used and they believe that breaking the current 1,024-bit RSA standard is about a thousand times harder. This appears long, but, clearly, current cryptosystems are secure only if the computational power of an attacker is limited. In other words, RSA is computationally secure. Moreover, P. Shor showed that large numbers can be factorized even in polynomial time if a quantum computer is employed [3], i.e. exponentially faster than the best known classical algorithm. Hence, the emergence of quantum computers is expected to immedicately threaten the security of conventional cryptosystems.

In 1882, F. Miller invented an encryption technique named one-time pad (OTP) where an encrypted message is generated by pairing a plaintext bit by bit with a random and secret key [4, 5]. In 1949, C. Shannon mathematically proved that it is impossible to break a ciphertext if it is encrypted with the OTP algorithm [6]. In other words, the OTP is proven to be information-theoretically secure, i.e. unbreakable even if an adversay has unlimited computational power, provided that a plaintext is paired with a truly random secret key and the key is used only once. However, to implement the OTP, one must generate a truly random key, which is a non-trivial requirement, and distribute it to users without it being revealed to adversaries. The practical problem of secure random-key distribution has prevented the OTP from being widely used as a real-world cryptosystem despite of its unique security.

Fortunately, the secure distribution of random secret keys has become possible with the emergence of a quantum key distribution (QKD). QKD exploits quantum physical properties of photons and allows creating perfectly correlated keys at different users without revealing information to unauthorized parties[7, 8]. In [8], quantum entanglement (explained in chapter 2) shared by two parties is measured in order to generate perfectly correlated keys. The security of the key is guaranteed by the violation of Bell's inequality [9, 10]. Hence, the randomness and secrecy of the key relies on quantum mechanical laws. The inequality is maximally violated if the shared keys are perfectly correlated. Any attempt of eavesdropping will inevitably reduce the entanglement. This causes a reduction, or even failure, of the Bell inequality violation, thus revealing the presence of an adversary in the communication channel. The shared secret key is further processed with the aid of classical postprocessing, i.e. error correction [11] and privacy amplification [12], in order to increase correlation and secrecy of the key, respectively. Once a secret key is securely generated using QKD a message can be encrypted using the OTP, thereby guaranteeing unconditional security of communication in the presence of adversaries.

One-Time Pad + Quantum-Key Distribution = Secure Communication

1.1 Long-Distance Quantum Communication

The longest distances for quantum communication are currently reported to be 144km [13, 14] and 200km [15] for free-space and optical-fibre based experiments, respectively. One of the major obstacles for realizing long-distance quantum communication protocols in a real-world setting is the transmission loss of the communication channel. For instance, if one imagines that a photon encoded with quantum information travels through 1,000 km long optical telecommunication fibre, which has a loss of 0.2 dB/km, then the probability that the photon reaches the destination would be only 10^{-20}. Hence, if one generates photons at a rate of 1 Ghz, i.e. 10^9 photons per second, the average time for a single photon to be sucessfully transmitted is about 3,000 years!

In classical communication, information can be encoded into different levels of an electrical signal, for instance, 0V (5V) for the bit value 0(1). This means that if the information is sent over a long distance through a lossy communication channel the signal can be easily recovered at any location of the channel using signal amplifiers. Unlike classical information, quantum information encoded into a degree of freedom of a single particle can not be amplified in accordance with one of the fundamental rules of quantum physics named the *no-cloning theorem* [16, 17]. Moreover, such quantum information is often very fragile against envorinmental decoherences such as interaction with other particles or surrounding fields.

A simple way of securing the transmission of classical information using quantum key distribution would be to interconnect many short-distance QKD links. A sender sends a message

over a long distance with the assistance of interim network nodes using a key shared by means of QKD with the next node. After the information is being encrypted, it is transmitted to the neighboring node. The first interim receiver then decrypts the information and re-encodes it with a key shared with the next node. He/She then forwards the ciphertext to the latter. This procedure iterates until the information is carried to the final receiver of the communication channel. Comunication distance is not a limiting factor and it could be arbitrary for this strategy. However, all interim receivers involved in this scheme must be trusted in order to guarantee the security of the information. This trusted-node based quantum network has been built in the United State (DARPA, [18]) and Europe (SECOQC, [19]).

1.2 Quantum Repeater

In 1998, H. -J. Briegel, W. D*ür*, J. I. Cirac, and P. Zoller [20] proposed a beautiful idea, the quantum repeater, that allows secure long-distance quantum communication without the need for trusted interim users. The proposal explains how quantum entanglement as a communication resource is successfully distributed between two users who are separated by a long distance. The idea is simply to concatenate heralded quantum entanglement links over many short distance by means of entanglement swapping, thereby generating quantum entanglement over the entire communication link. This is as if several small-size soap bubbles combine to making one large bubble.

Let us examine a modified (simple) quantum repeater protocol more closely. We consider the situation of two distant users, separated by a long distance L (divided into N shorter elementary links), who wish to establish quantum entanglement with the aid of $N-2$ interim users. First, as shown in Figure 1.1, each of the N elementary links prepares an entangled photon pair. Second, two neighboring links perform a Bell-state measurement (BSM) (ex-

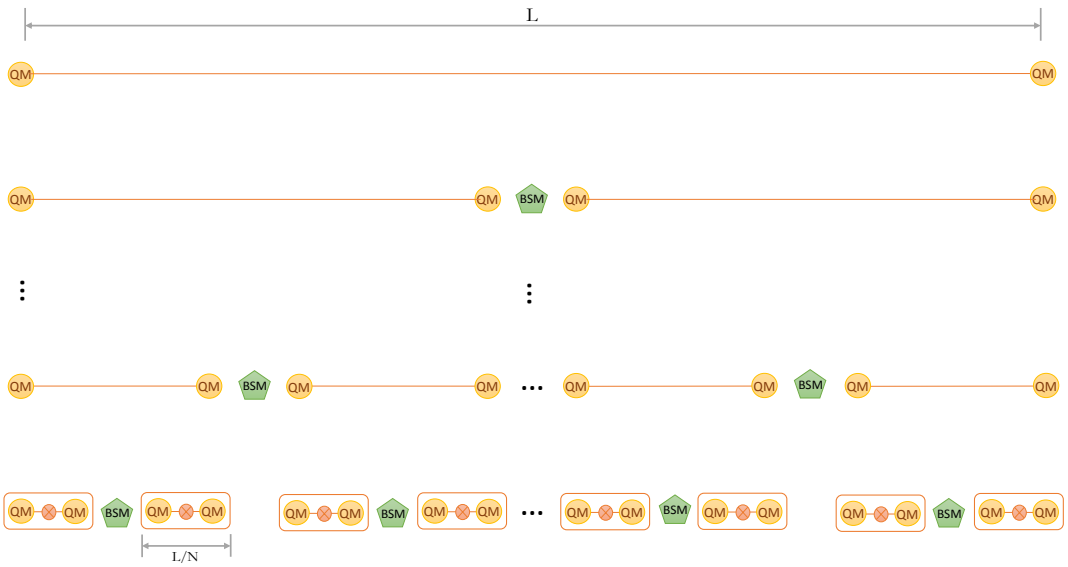

Figure 1.1: **A schematic diagram of a quantum repeater.** ⊗ represents sources of entangled photons, and QM and BSM denote quantum memories and Bell-state measurements, respectively.

plained in chapter 2) with two photons (one from each pair), allowing to generate quantum entanglement over the distance of two elementary links. This process, which is often referred to as entanglement swapping [21], continues until entanglement is established across the entire distance. In order to perform the BSM, entanglement across elementary links needs to be heralded and it must be possible to recall it on demand. We note that, owing decoherence during entanglement transmission, entanglement purification [22] is necessary as the distance between the end users is increased. However, current experimental effots, including in our group, often ignore this step as the amount of added errors (i.e. decoherence) is small over links of relevant length (e.g. a total length of 1000 km) and classical error correction, which is much simpler to implement than entanglement purification, suffices. Obviously, this makes our approach is not scalable. In other words, it allows overcoming channel loss, but not decoherence.

Quantum Repeater = On-demand Entanglement + Bell-state Measurement

If entanglement is not prepared in on-demand fashion, the repeater strategy works only if all N individual elementary links simultaneously prepare entanglement and this results in a transmission loss of $\underbrace{e^{-\alpha L/N} \times e^{-\alpha L/N} \times \cdots \times e^{-\alpha L/N}}_{N} = e^{-\alpha L}$, i.e. no better than a direct transmission, where α denotes the absorption coefficient of communication channel. One approach for on-demand entanglement is to prepare entanglement in a heralded manner and keep it in quantum memories until needed. Here, heralding means that one knows when entanglement is established. In the architecture discussed above, heralded entanglement and quantum memories capable of preserving entanglement are two key ingredients in building elementary repeater links.

On-demand Entanglement = Heralded Entanglement + Quantum Memories

Once each elementary link established entangled quantum memories, a BSM plays the role of bridging the links. In order to perform the BSM with two photons, one from each link and recalled from adjacent quantum memories, the memories must not modify the photonic wavefunction during storage. This is because a BSM requires two indistinguishable photons in all photonic degrees of freedom, i.e. spatial, spectral, temporal, and polarization modes.

This thesis is organized into 9 chapters. In chapter 1, I describe a quantum repeater for secure quantum communication over a long distance and explaine how a repeater can be built. Chapter 2 describes basic components for quantum communications : quantum entanglement, quantum memory and two-photon measurements. Chapter 3 demonstrates the experimental distribution of entangled photons over a real-world fibre links. Chapter 4 demonstrates entanglement swapping with quantum-memory compatible photons shown in

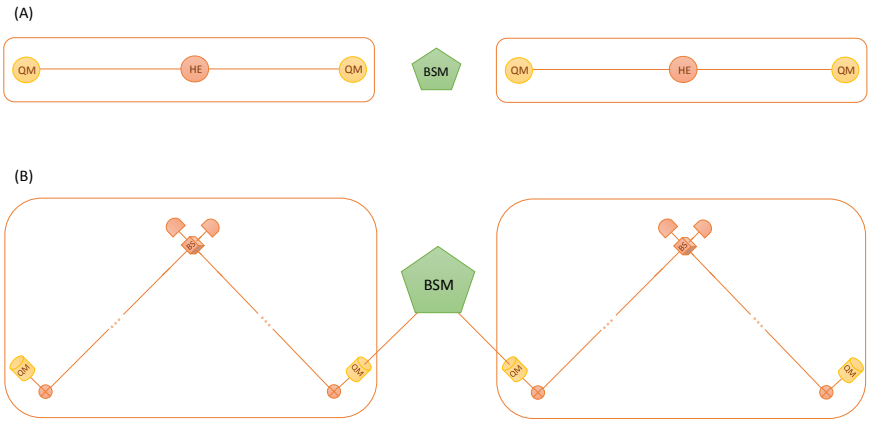

Figure 1.2: **Elementary link of quantum repeater (red box) and Bell-state measurement (green pentagon).** (A) Elementary link consists of heralded time-bin entanglement and two quantum memories. Two neighboring links are entangled by means of a BSM. HE and QM denote heralded entanglement and quantum memory, respectively. (B) Heralded entanglement is realized via entanglement swapping. The BSM is implemented by a beam splitter followed by single-photon detectors. $\otimes$ and BS denotes an entangled photon pair and a lossless symmetric beam splitter, respectively.

Figure 1.2, as required for building an elementary link of a quantum repeater. Chapter 5 demonstrates a solid-state quantum memory that allows the reversible mapping of photonic qubits. Chapter 6 and 7 demonstrate our quantum memories, interfacing with 795 nm and telecommunication-wavelength photons, are capable of preserving entanglement during storage, as required for an elementary link of a quantum repeater. Chapter 8 demonstrates two-photon measurements, i.e. two-photon interference and Bell-state measurement, with photons recalled from separate quantum memories as shown in Figure 1.2, as required to interconnect neighboring elementary links of a quantum repeater. Finally, I conclude in Chapter 9.

Bibliography

[1] R. Rivest, A. Shamir, L. Adleman, Communications of the ACM 21, 120 (1978).

[2] T. Kleinjung, K. Aoki, J. Franke, A. K. Lenstra, E. Thom, J. W. Bos, P. Gaudry, A. Kruppa, P. L. Montgomery, D. A. Osvik, H. te Riele, A. Timofeev, P. Zimmermann, Lecture Notes in Computer Science 6223, 333 (2010)

[3] P. Shor, SIAM J.Sci.Statist.Comput. 26, 1484 (1997)

[4] F. Rubina, Cryptologia 20, 359 (1996)

[5] S. M. Bellovin, Cryptologia 35, 203 (2011)

[6] C. Shannon, Bell System Technical Journal 28, 656 (1949)

[7] C. H. Bennett and G. Brassard, IEEE, New York, 175 (1984)

[8] A. K. Ekert, Phys. Rev. Lett. 67, 661 (1991)

[9] J. S. Bell, Physics 1 195 (1964)

[10] J. F. Clauser, M.A. Horne, A. Shimony, R.A. Holt, Phys. Rev. Lett. 23, 880 (1969)

[11] D. Pearson, AIP Conference Proceedings 734, 299 (2004)

[12] C. H. Bennett, G. Brassard, C. Crepeau, U. M. Maurer. IEEE Transactions on Information Theory 41, 6 (1995)

[13] R. Ursin, F. Tiefenbacher, T. Schmitt-Manderbach, H. Weier, T. Scheidl, M. Lindenthal, B. Blauensteiner, T. Jennewein, J. Perdigues, P. Trojek, B. Oemer, M. Fuerst, M. Meyenburg, J. Rarity, Z. Sodnik, C. Barbieri, H. Weinfurter, and A. Zeilinger, Nature Physics 3, 481 (2007)

[14] T. Schmitt-Manderbach, H. Weier, M. Furst, R. Ursin, F. Tiefenbacher, T. Scheidl, J. Perdigues, Z. Sodnik, C. Kurtsiefer, J. G. Rarity, A. Zeilinger, and H. Weinfurter, Phys. Rev. Lett., 98, 010504 (2007)

[15] T. -Y. Chen, J. Wang, Y. Liu, W.-Q. Cai, X. Wan, L.-K. Chen, J.-H. Wang, S.-B. Liu, H. Liang, L. Yang, C.-Z. Peng, Z.-B. Chen, and J.-W. Pan, Optics Express 18, 8587 (2010)

[16] W. Wootters and W. Zurek, Nature 299, 802 (1982)

[17] D. Dieks, Phys. Lett. A 92, 271 (1982)

[18] C. Elliott, A. Colvin, D. Pearson, O. Pikalo, J. Schlafer, and H. Yeh, Proc. SPIE 5815, 138 (2005)

[19] M. Peev et. al., New J. Phys. 11, 075001 (2009)

[20] H.-J. Briegel, W. Dr, J. I. Cirac, and P. Zoller, Phys. Rev. Lett. 81, 5932 (1998)

[21] M. Zukowski, A. Zeilinger, M. A. Horne, and A. K. Ekert, Phys. Rev. Lett. 26, 4287 (1993)

[22] C. H. Bennett, G. Brassard, S. Popescu, B. Schumacher, J. A. Smolin, and W. K. Wootters, Phys. Rev. Lett. 76, 722 (1996)

Chapter 2

Quantum Communication Components

This Chapter describes three key elements for quantum information and communication with quantum repeaters, namely quantum entanglement, quantum memory, and Bell-state measurement. The first section introduces the basics of entanglement. Since entanglment is not only a key ingredient for quantum repeaters but also a very important resource for fundamental tasks such as teleportation [1] and random number certification [2], it is useful to understand entanglement both qualitatively and quantitatively. The section starts by introducing the concept of a quantum bit (Qubit) and then entangled qubits together with the definition of entanglement. Next, an experimental method to generate time-bin entangled photonic qubits is introduced and various entanglement verification methods, i.e. the Bell inequality, quantum state tomography, and entanglement visibility are discussed. These methods allow one to verify the nonlocal features of quantum correlations (Chapter 3), the entanglement between independent photons (Chapter 4), and the entanglement-preserving capability of quantum memories (Chapter 6 and 7).

In the second section, memories for quantum storage are introduced. Quantum memory is known to be useful for a range of quantum information processing applications, including quantum computing, but here we focus on its use in a quantum repeater. The section starts with an explanation of the photon-echo based quantum storage protocol used for our solid-state memories, i.e. the atomic frequency comb (AFC). This protocol allows one to map a photon onto an atomic state and retrive it back onto a photonic state at a later time. Subsequently, the section introduces the quantum memory materials used in our implementations, more precisely a thulium-doped $LiNbO_3$ waveguide and an erbium-doped optical fibre. We

then describe their experimental operation and discuss the figures of merit for the memory performance, i.e. bandwidth, recall efficiency, storage time, multiplexing capacity, and storage fidelity. This knowledge is useful for understanding the experiments in Chapter 5 to 8.

Finally, the last section introduces two-photon measurements, starting with two-photon interference, as a natural method to verify the indistinguishability of two photons. Subsequently, our implementation of a Bell-state measurement with photonic time-bin qubits is discussed.

2.1 Quantum Entanglement

2.1.1 Qubit

In order to better understand entanglement, it is useful to introduce a quantum bit (qubit) as the quantum analogue of a classical bit. The computational basis of the qubit, $|0\rangle$ and $|1\rangle$, is defined using two levels of a quantum-mechanical system in any degree of freedom, e.g. the spin of an electron or the polarization of light. In contrast to a classical bit, a qubit can represent an infinite number of states by allowing the coherent superposition of the two basis states, i.e. $|\psi\rangle = cos(\frac{\theta}{2})|0\rangle + e^{i\phi}sin(\frac{\theta}{2})|1\rangle$ with $0 \leq \theta \leq \pi$ and $0 \leq \phi \leq 2\pi$ as shown in Figure 2.1.

In our implementations we use qubits defined in the temporal degree of freedom. Such a time-bin qubit is constituted of a single photon in a superposition of being generated in two well-defined temporal modes, the *early* bin $|e\rangle$ and *late* bin $|l\rangle$ of width $\Delta\tau$, and separated by $\Delta t > \Delta\tau$ as shown in Figure 2.2. The separation between two temporal modes must be larger than the coherence time of the photon. This ensures well-defined independent information-encoding bases. The probability of finding a photon in $|e\rangle$ and $|l\rangle$ is given by

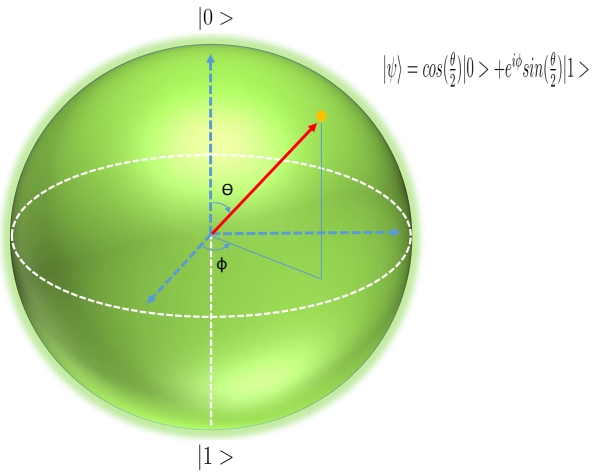

Figure 2.1: **Qubit representation.** A (red) vector represents a qubit and coherent superposition of two basis states ($|0\rangle$ and $|1\rangle$). For pure states, its tip lies on the surface of the sphere.

the absolute square of the probability amplitude coefficient, i.e. $\cos^2(\frac{\theta}{2})$ and $\sin^2(\frac{\theta}{2})$, respectively. When a photon travels through optical fibres, the temporal width of the photon may be broadened due to a wavelength-dependent chromatic dispersion. In the case of time-bin qubits, the broadening could perturb the state of the qubits if it exceeds the separation between two temporal bins. However, this decoherence can be circumvented by using a dispersion-compensating fibre that has an inversed sign and magnitude of dispersion with respect to that of standard optical fibres. On a positive note, time-bin qubits are immune to the typically significant depolarization effects induced during transmission through optical fibres [3]. Qubit encoding in photonic degrees of freedom is reviewed in [4].

2.1.2 Entanglement and Entangled Qubits

An entangled state [5] refer to the global state of a composite systems, that can not be written as a product of the states of the individual subsystems [6], i.e., for a bipartite system,

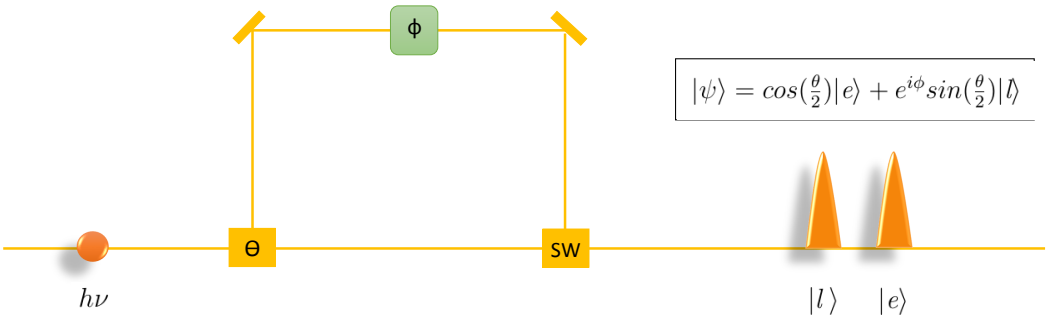

Figure 2.2: **Generation of a time-bin qubits** Coherent superposition of two temporal modes is realized using an imbalanced Mach-Zehnder interferometer with a relative phase of ϕ. $h\nu$ and $|e\rangle(|l\rangle)$ denotes the energy of a single photon and *early* (*late*) temporal bin, respectively. θ and SW denote a variable coupler and an optical switch.

$$|\psi\rangle_{AB} \neq |\psi\rangle_A \otimes |\psi\rangle_B \tag{2.1}$$

Entangled states allow the observation of quantum correlations. On the other hand, correlations that can be produced via unitary local operations and classical communication (LOCC) between individuals are classified as classical correlations. This is because LOCC do neither create nor increase entanglement [7]. Thus, LOCC provide one operational bound between classical and non-classical correlations. The strict operational classical-quantum boundary for correlations is reviewed in [8].

A time-bin entangled state of two qubits can be described as

$$|\psi\rangle_{AB} = cos(\frac{\theta}{2})|e\rangle_A \otimes |e\rangle_B + e^{i\phi} sin(\frac{\theta}{2})|l\,\rangle_A \otimes |l\,\rangle_B, \tag{2.2}$$

where $0 < \theta < \pi$ and $0 \leq \phi \leq 2\pi$. Here, $\otimes$ denotes the tensor-product operation and the subscripts A and B denote individual modes. If a photon is found in either $|e\rangle$ or $|l\,\rangle$ in mode A, then the other photon should reside in the same temporal bin in mode B. This happens with probabilities of $cos^2(\frac{\theta}{2})$ and $sin^2(\frac{\theta}{2})$ for $|e\rangle$ and $|l\,\rangle$, respectively. The entangled quantum system can not be described with only individual subsystems. In other words, the subsystems do not carry any information about the whole system, i.e. $\rho_A = \rho_B = \frac{\mathbb{I}}{2}$ where $\rho_{AB} = |\psi\rangle_{AB}\langle\psi|$ and $\rho_{A(B)} = Tr_{B(A)}(\rho_{AB})$. It is worth to note that there are four maximally entangled quantum states of two qubits, known as the *Bell* states :

$$\begin{aligned} |\Phi^{\pm}\rangle_{AB} &= \frac{1}{\sqrt{2}}(|ee\,\rangle_{AB} \pm |ll\,\rangle_{AB}) \\ |\Psi^{\pm}\rangle_{AB} &= \frac{1}{\sqrt{2}}(|el\,\rangle_{AB} \pm |le\,\rangle_{AB}). \end{aligned} \tag{2.3}$$

It is an astonishing property of entanglement that it exists regardless of the space and time separation of the particles in modes A and B. [9]. Entanglement encoded in photonic degrees of freedom is reviewed in [4].

2.1.3 Photon-Pair Source

Spontaneous Parametric Down-Conversion

One well-known technique for generating entangled photonic qubits is to use the nonlinear optical process of spontaneous parametric down-conversion (SPDC). In SPDC, a photon in

a strong light field propagating through an optical medium with a second-order nonlinearlity may split into a pair of photons that have total energies and momenta equal to the energy and momentum of the pump photon :

$$\begin{aligned} E_P &= E_A + E_B \\ \vec{k}_P &= \vec{k}_A + \vec{k}_B, \end{aligned} \tag{2.4}$$

where the subscript P identifies the photon belonging to the pump field and A, B as being members of the created pair. These relations describe the laws of energy and momentum conservation as shown in Figure 2.3.

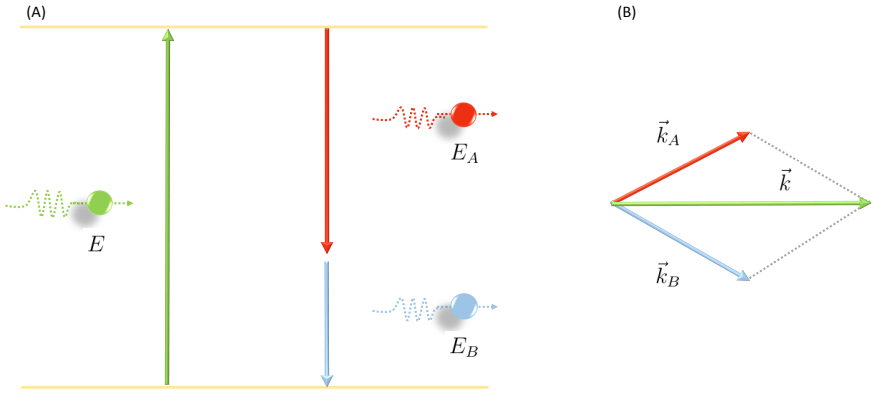

Figure 2.3: **Spontaneous parametric down-conversion** (A) Energy conservation. The energy of a pump photon (green) must be the same as the sum of the energies of the generated photons (red and blue). (B) Momentum conservation. Momentum vectors of generated photons are correlated by the law of momentum conservation.

In order to understand the physics of SPDC, let us consider the interaction Hamitonian of a nonlinear optical material. The time-independent interaction Hamiltonian for a param-

etically driven nonlinear medium that generates a non-degenerate photon pair is described by

$$H = \hbar\chi^{(2)}[E_P^\dagger ab - E_P a^\dagger b^\dagger], \tag{2.5}$$

where $\hbar$ is the Planck constant, $\chi^{(2)}$ the second-order component of the electric susceptibility of the medium, E_P the electric field operator of the pump light, and $a(b)$ the annhilation operator of a photon in mode A (B). The action of the corresponding time-evolution operator on a vacuum state generates a two-mode squeezed vacuum state [10]. :

$$|\psi\rangle_{AB} = e^{-iHt/\hbar}\ |0>= \sum_{n=0}^{\infty} \frac{1}{\cosh\zeta}\tanh^n\zeta\ |nn>_{AB}, \tag{2.6}$$

where t denotes time and n the number of photons per mode. Note that the time-evolution operator can be regarded as a squeezing operator with the squeezing parameter $\zeta = iE_p\chi^{(2)}t$, that is, $e^{-iHt/\hbar} = S(\zeta) = e^{[\zeta^\dagger ab + \zeta a^\dagger b^\dagger]}$. As the energy spectrum of the state obeys the Boltzmann distribution with a mean photon number of $< n >= \sinh\zeta$ in each mode, it is a thermal state that is generated via the process of SPDC [10]. For a weak nonlinear interaction ($\zeta \to 0$), the factor $\cosh\zeta$ approaches 1 so the probability of generating a single photon pair can be approximated by $\tanh^2\zeta$.

Quasi-Phase Matching

Because of chromatic dispersion, in real nonlinear materials, the wavenumber of the pump light is usually not the same as the sum of those of the generated photon pair, thereby leading to a phase mismatch between the waves. One well-known technique for overcoming this mismatching in a nonlinear medium is to use birefringent phase matching, by which

the phase mismatch is compensated with the aid of the birefringence of the material. The conversion efficiency, $\eta_{conversion} = N_{output}/N_{input}$, with this phase-matching approach is on the order of 10^{-13} [11].

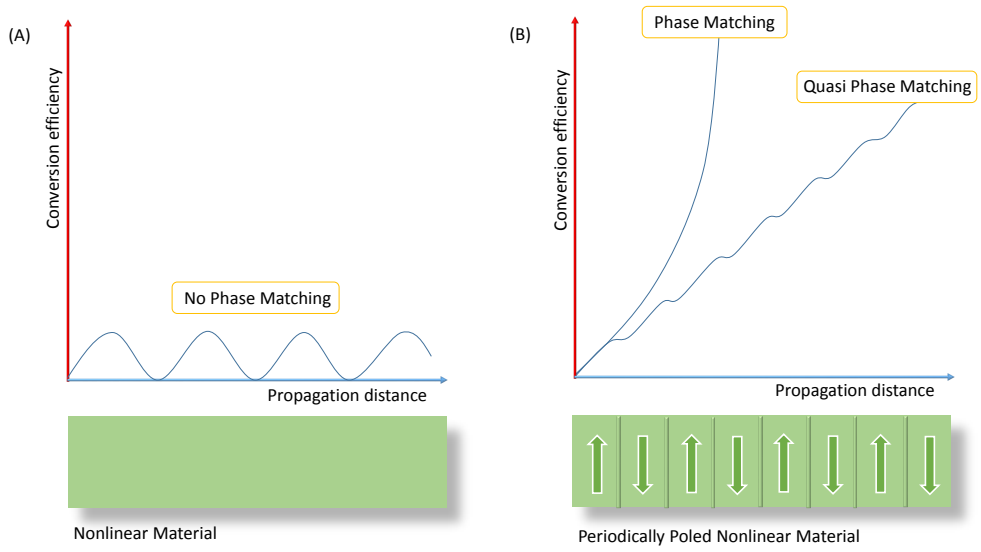

Figure 2.4: **SPDC efficiency comparison.** (A) No phase matching. (B) Quasi-phase matching with a periodically poled nonlinear material. Arrows denote the directions of the local electric dipole moments.

Another widely-used phase-matching method is that of quasi-phase mathcing (QPM) in which the phase mismatch is artifically cancelled by periodically reversing the polarity of the non-linearity over the entire length of the nonlinear medium. This periodic poling can be engineered by applying sufficiently strong electric fields periodically through the medium, causing a reversal of the local spontaneous polarization of the ferroelectric material. If conservation of momentum - that is, $\hbar k_p(n_p) = \hbar(k_A(n_A) + k_B(n_B) + \frac{2\pi}{\Lambda})$ where Λ stands for the period of poling - and of energy are simultaneously met, a high conversion efficiency can be achieved as illustrated in Figure 2.4 (B). The QPM efficiency can be calculated with the aid of the Sellmeier equation that allows computing the wavelength-dependent refractive index (n) of the considered material [12]. The conversion efficiency with a periodically poled

Lithium Niobate (PPLN) crystal, for instance, reaches to the order of $\eta_{conversion} = 10^{-9}$ in our implementation, which is superior to that achievable by means of using birefringent phase-matching.

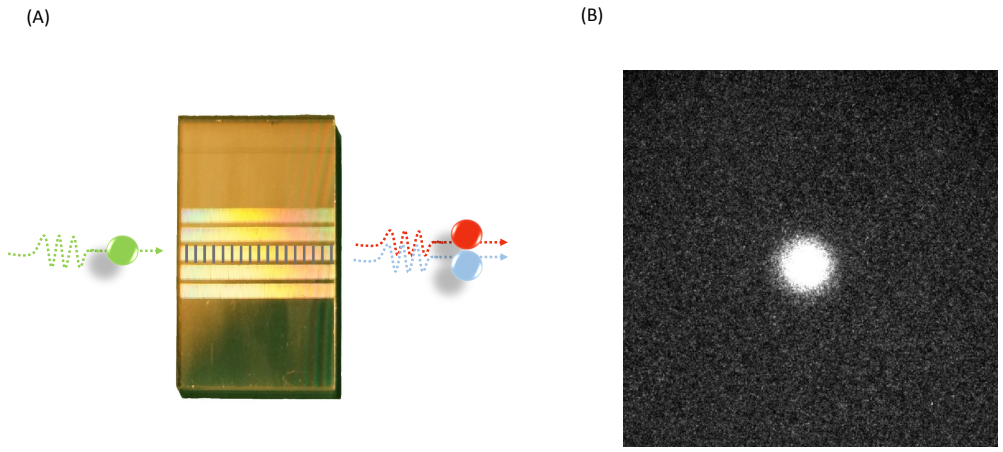

Figure 2.5: **Generation of photon pairs** (A) Picture of a periodically poled Lithium Niobate (PPLN) crystal (Covesion Ltd.). The crystal with a poling period of 7.0 micro-meter is heated to around 100 $^{\circ}C$ to generate a photon pair at 795 nm and 1532 nm with pump photons at 523 nm. (B) Spatial distribution of 795 nm photons generated using the PPLN via SPDC. The picture was taken by a single-photon camera (Deltaphotonics).

Time-bin entangled photon pair. : If two mutually coherent pump pulses separated by Δt interact with a PPLN crystal via SPDC, time-bin entangled photon pairs in the form of Equation 2.2 are generated as shown in Figure 2.6. In our implementation, we generate about 10 million pairs per second with an average pump power of 15 miliwatts.

Characterization of the output from SPDC source

The number of generated photon pairs per second, N_{pair}, can be calculated by taking the ratio of the product of the single photon counts (N_A, N_B) to the joint-detection counts (N_{AB}), i.e.

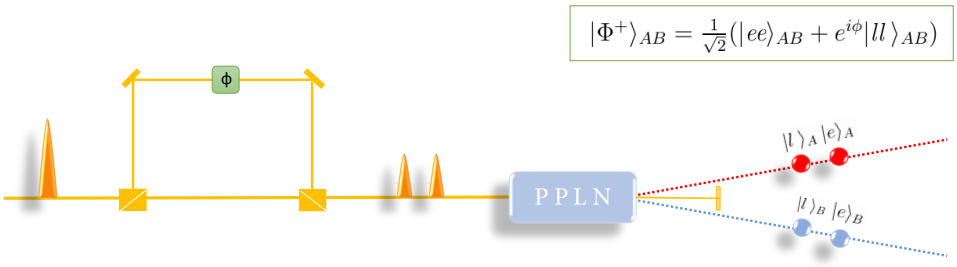

Figure 2.6: **Generation of photonic time-bin entanglement.** Two pump pulses are coherently superposed by the Mach-Zehnder interferometer and pump a PPLN in order to generate time-bin entanglement.

$N_{pair} = \frac{N_A \times N_B}{N_{AB}} = \frac{(N_{pair} t_A \eta_A) \times (N_{pair} t_B \eta_B)}{(N_{pair} t_A t_B \eta_A \eta_B)}$, where t_i and η_i denote transmission and detection efficiency, respectively. Dividing this value by the pump pulse repetition rate (R) further allows computing the probability of generating a photon pair per pump pulse, $P_{pair} = N_{pair}/R$. A second way to calculate the pair generation probability is to use a coincidence-to-accidental ratio (CAR) as shown in Figure 2.7 (A). A coincidence (accidental) count refers to a joint detection of two photons that stem from the same (different) pair(s). It is clear that if one member of a photon pair is detected then the other member should be present. On the other hand, the probability of detecting one photon conditioned on detecting another photon that does not originate from the same pair is approximately the same as the probability of generating a photon pair per pump pulse (assuming multiphoton events are negligible). Hence we can write $P_{pair} = 1/CAR = \frac{N_{acc}}{N_{coin}} = \frac{N_{pair} t_A t_B \eta_A \eta_B P_{pair}}{N_{pair} t_A t_B \eta_A \eta_B}$. Note that no knowledge about the loss of the channel and detection efficiency plays a role in either method. More details can be found in [13].

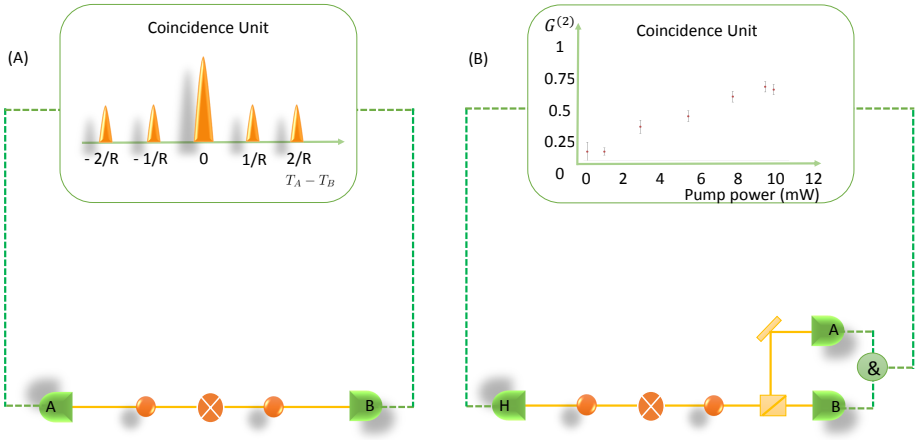

Figure 2.7: **Measurement setups for SPDC-source characterization.** $\otimes$ denotes a photon-pair source. (A) The measurement of coincidence-to-accidental ratio. This measurement allows to calculate the probability of generating a photon pair per pump pulse. $T_A(B)$ denotes the detection time of a photon at the detector A (B) and R the repetition rate of pump pulses. (B) The measurement of the auto-correlation function, $G^{(2)}$. The value approaches zero as the pump power decreases. H stands for a heralding signal.

While these two methods allow one to calculate the probability for generating a photon pair, a similar method allows one to find out whether or not the output characterizes as non-classical. This is done via a measurement of the heralded second-order auto-correlation function $G^{(2)}$. Figure 2.7 (B) shows the schematics of the $G^{(2)}$ measurement. If one member of a photon pair is detected, it heralds the presence of the other member. In other words, it heralds a single-photon state. Thus, if the single photon is directed to a beam splitter, then no coincidence between two outputs will happen. This yields $G^{(2)} = \frac{P_{A|H} \times P_{B|H}}{P_{AB|H}}$ equal to zero for a perfect single-photon source. For non-classical sources, this value ranges from 0 to 1. Note that Possinian- and thermal-statistics yield values of 1 and 2, respectively.

2.1.4 Entanglement Verification Tools

Measurements of quantum states are important as they play a key role in interpretating quantum mechanics as well as for applications of quantum information science. The most widely used method is that of a projective measurement. In this case, a quantum state is projected onto the eigenstate of an observable, i.e. a Hermitian operator. This means that the wavefunction is collapsed and becomes one bit of classical information. Pauli matrices, denoted as $\sigma_i (i = x, y, z)$, allow expressing the projection operator for any qubit. Pauli matrices are definded by $\sigma_1 \equiv \left(\begin{smallmatrix} 1 & 0 \\ 0 & 1 \end{smallmatrix}\right), \sigma_2 \equiv \left(\begin{smallmatrix} 0 & 1 \\ 1 & 0 \end{smallmatrix}\right), \sigma_3 \equiv \left(\begin{smallmatrix} 0 & -i \\ i & 0 \end{smallmatrix}\right), \sigma_4 \equiv \left(\begin{smallmatrix} 1 & 0 \\ 0 & -1 \end{smallmatrix}\right)$. For time-bin entangled qubits, the Mach-Zehnder interferometer combined with single-photon detectors realize the Pauli operations. Different operations can be implemented by setting different phases and beam-splitting ratios of the interferometer as shown in Figure 2.8. This measurement setup allows to perform various tests including the Bell inequality, quantum state tomography and measurement of entanglement visibility in order to verify the presence of entanglement in a quantum system. Those tests will be described in the following sections.

Owing to temperature fluctuation and mechanical vibration, the relative path-length difference between two the arms of an interferometer will change over time. This leads to an unstable phase of the interferometer during a measurement, i.e. a time-varying projection basis, described by the relation $\Delta\Phi = \Phi_l - \Phi_s = k\ (L_l - L_s)$, where k and L_l (L_s) denote the wavenumber of the incident light and the length of the long (short) arm of the interferometer, respectively. In order to stabilize the phase, we thermally and mechanically control the interferometer. First, we control the temperature of the interferometer by adjusting the current through a copper wire that allows heating a metal plate inside the interferometer using a commercial temperature controller (Thorlabs). Secondly, we send highly-coherent, frequency-stablized laser light (TeraXion) through the interferometer. To avoid crosstalk with the photons to be analyzed by the interferometer, we make sure that classical and

quantum light does not overlap, i.e. propagates along different spatial modes. The intensity of the interfering laser light, which depends on the phase of the interferometer, is detected by an optical detector. The detection signal is then sent to a data aquisition card (DAC) connected to a personal computer where a feedback loop is designed using labview software. If the signal voltage deviates from a set value, then a piezo, which is controlled by the DAC (National Instruments), displaces a mirror in one arm of the interferometer until the set and the actual voltage match. This allows compensating unwanted phase shift. Through the combination of temperature stabilization and active phase locking, we are able to maintain phase stability over several days.

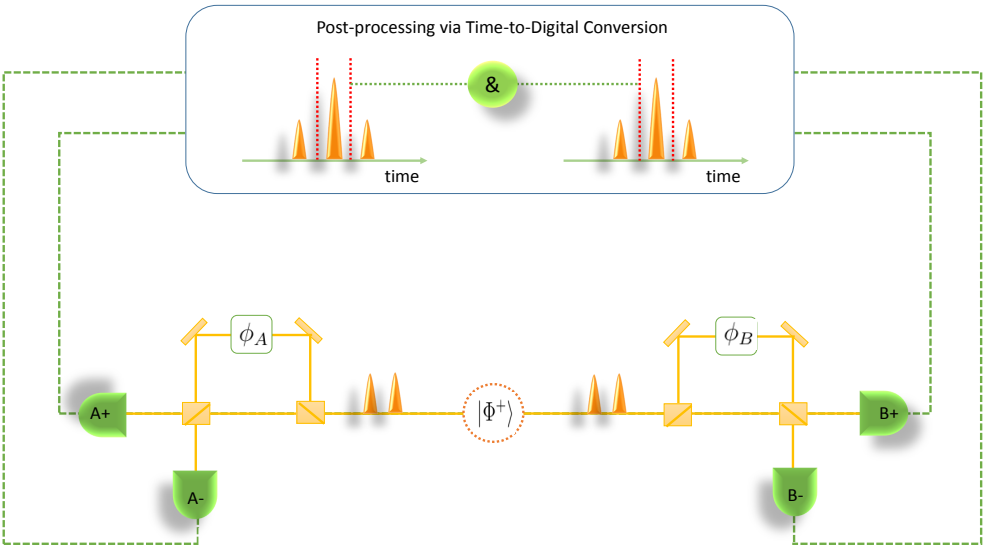

Figure 2.8: **A measurement setup for time-bin entangled photon pairs.** A projective measurement on each photon is implemented by independent Mach-Zehnder interferometers followed by single-photon detectors at each output. Detection signals are postprocessed using a time-to-digital converter(TDC) and a computer (not shown).

Bell Inequality

In 1935, A. Einstein, B. Podolsky, and N. Rosen argued that a quantum-mechanical description of an entangled physical system, e.g. following the example by Bohm [14] a pair of

spin-1/2 particle in a singlet state $|\psi\rangle_{AB} = \frac{1}{\sqrt{2}}(|\uparrow\downarrow\rangle - |\downarrow\uparrow\rangle)$, where the arrow denotes spin orientation, is incomplete. They then reached the conclusion that a so-called local hidden-variables theory, rooted in locality and realism, is required to complete the description of reality [15]. In 1964, J. S. Bell [16] formulated a mathematical inequality for which any correlations in the paradigm of locality and realism should be bounded by $|E(\boldsymbol{a},\boldsymbol{b}) - E(\boldsymbol{a},\boldsymbol{c})| \leq 1 + E(\boldsymbol{b},\boldsymbol{c})$, where E describes an expectation value of correlation. Furthermore, using the quantum mechanical prediction that $E(\boldsymbol{a},\boldsymbol{b}) = \langle\psi|(\sigma_A \cdot \boldsymbol{a})(\sigma_B \cdot \boldsymbol{b})|\psi\rangle = -\boldsymbol{a}\cdot\boldsymbol{b}$, he theoretically concluded that no deterministic local hidden-variables theory can agree with all statistical predictions of quantum physics for measurements on maximally entangled states such as the singlet states. This means that violation of the inequality reveals the presence of correlations that are not explainable with any classical theories, i.e. theories that satisfy the assumptions of reality and locality.

Bell's inequality was derived by considering Bohm's *Gedanken experiment* where a physical system consists of a pair of spatially separated spin-$\frac{1}{2}$ particles in a singlet state, generated by dissociation of spin-0 system. Thus Bell assumed not only determinism, i.e. $E(\boldsymbol{a},\boldsymbol{a}) = -1$ when measurement bases are parallel, but also that all particles are detected without any loss. This means that he did not take into account the possibility of experimental errors, e.g. particle leakage onto wrong basis and inefficient sampling. These assumptions have made it hard to perform experimental tests of quantum mechanics based on Bell's original inequality.

Fortunately, in 1969 J. F. Clauser, M. A. Horne, A. Shimony and R. A. Holt (CHSH) generalized Bell's inequality by relaxing the assumption of determinism, more specifically, by imposing the possibility that the other member of the pair can leak to an orthogonal channel when measurement analyzers are set up in parallel [17]. The CHSH-Bell inequality is described by

$$S = |E(\boldsymbol{a}, \boldsymbol{b}) + E(\boldsymbol{a'}, \boldsymbol{b}) + E(\boldsymbol{a}, \boldsymbol{b'}) - E(\boldsymbol{a'}, \boldsymbol{b'})| \leq 2. \tag{2.7}$$

Here the four correlation coefficients $E(\boldsymbol{a}, \boldsymbol{b}) = \frac{C(\boldsymbol{a},\boldsymbol{b}) - C(\boldsymbol{a},-\boldsymbol{b}) - C(-\boldsymbol{a},\boldsymbol{b}) + C(-\boldsymbol{a},-\boldsymbol{b})}{C(\boldsymbol{a},\boldsymbol{b}) + C(\boldsymbol{a},-\boldsymbol{b}) + C(-\boldsymbol{a},\boldsymbol{b}) + C(-\boldsymbol{a},-\boldsymbol{b})}$, where C denotes coincidence counts. We use this inequality throughout the experiments described in this thesis.

The CHSH-Bell inequality is equivalent to Bell's original inequality if the assumption of determinism holds. This family of Bell inequalities was further generalized to the case of non-determinism by J. S. Bell [18] and J. F. Clauser and M. A. Horne [19], to what is called the CH-Bell inequality. In contrast to Bell's original inequality, the CHSH-Bell inequality is more easily experimentally testable as it accepts the events of wrong-basis projection. However, it still assumes fair sampling of the produced particles. To avoid this assumption $2/(1 + \sqrt{2})$ of the particles should be sampled [20, 21]. Note that this bound of sampling efficiency is further lowered to 2/3 [22] for the CH-Bell inequality [19] if a non-maximally entangled state is considered.

Together with the assumption of fair-sampling, locality and free choice are the three major assumptions for the Bell-inequality family. The assumption of locality requires particles to be spacelike separated during measurement, preventing them from communicating at the speed of light. If the measurement duration of each of the particles is shorter than the time it takes light to travel between them, then this assumption ensures that there is no mutual influence on their measurement outcomes. The third assumption, free choice, says that the choices of measurement settings on each particle should be independent from each other. In other words, the technique of true random number generation is required to meet the criterion of free choice.

It is in general worthwhile to clearly understand all underlying assumptions to be able to not only implement genuine Bell inequality tests but also to realize faithful secure quantum communication. Experimentally, the locality loophole has been successfully closed using entangled photons by G. Weihs et.al. in 1998 [23] and the free choice loophole has been closed by T. Scheidl et al. in 2010 [24]. Fair-sampling loophole-free experiments have also been successfully conducted with trapped ions [25] and photons [26, 27] in 2001 and 2013, respectively. Experimental tests with closed loopholes are summarized in Table 2.1. To date, unfortunately, no experiment satisfying more than one assumption at the same time has been reported.

Loophole	Quantum System	Experiment
Locality	photons	G. Weihs et. al. (1998)
Free Choice	photons	T. Scheidl et. al. (2010)
Fair Sampling	trapped ions	M. A. Rowe et. al. (2001)
	photons	M. Giustina et.al. and B. G. Christensen et.al. (2013)

Table 2.1: Summary of experimental Bell tests with a closed loophole.

Quantum State Tomography

Quantum state tomography is the process by which any quantum system, including the spin of an electron, can be completely characterized using an ensemble of many identical particles [28, 29]. Multiple measurements in different bases allow reconstructing a quantum state, just as classical tomography allows a three-dimensional object to be rendered by scanning it from different physical directions. Quantum state tomorgraphy thus provides an alternate method to verify that a state is entangled.

Any two-qubit density matrix can be uniquely described by

$$\rho_{AB} = \frac{1}{2^2} \sum_{i=1}^{4} \sum_{j=1}^{4} S_{ij} \sigma_i^A \otimes \sigma_j^B, \tag{2.8}$$

where σ_i are the Pauli matrices defined in previous section. The Stokes parameters, S_{ij}, are given by $S_{ij} \equiv \mathrm{Tr}[(\sigma_i^A \otimes \sigma_j^B)\rho_{AB}] = (\lambda_i^+ P^A_{|\sigma_i^+\rangle} + \lambda_i^- P^A_{|\sigma_i^-\rangle}) \otimes (\lambda_j^+ P^B_{|\sigma_j^+\rangle} + \lambda_j^- P^B_{|\sigma_j^-\rangle})$, where $\lambda^{+(-)}$ denotes the eigenvalue corresponding to an eigenstate $|\psi\rangle_+ (|\psi\rangle_-)$ of a Pauli operator σ and $P^{A(B)}_{|\sigma^{+(-)}\rangle}$ the probability for a given state to be projected onto the corresponding eigenstate of the projector. At first glance, this seems to require $4^2 - 1$ measurement settings with two detectors for each particle as all 15 Stokes parameters need to be determined in order to reconstruct the density matrix. However, as the parameters whose subscript includes 0 can be derived from the ones with none-zero subscript the number of measurement settings can be reduced to 3^2, resulting in $3^2 \times 2^2$ measurement outcomes. Interestingly, this number of measurements can be even further decreased because of the fact that a density matrix itself has only $4^2 - 1$ free parameters, which implies that the same number of measurements should be sufficient to specify the corresponding state. Fortunately, this is possible due to the fact that the 36 measurement bases are not linerly independent.

By defining a set of 16 linearly independent 2-qubit measurement projectors, $|\psi_{mn}\rangle\langle\psi_{mn}|$, one can relate the joint-detection probabilities with the Stokes parameters S_{ij} : $P_{mn} = \langle\psi_{mn}|\rho_{AB}|\psi_{mn}\rangle = \frac{1}{2^2} \sum_{i=1}^{4} \sum_{j=1}^{4} M_{mn,ij} S_{ij}$ where the elements $M_{mn,ij}$ of the $4^2 \times 4^2$ matrix $\hat{M}$ are given by $M_{mn,ij} = \langle\psi_{mn}|\sigma_i^A \otimes \sigma_j^B|\psi_{mn}\rangle$. This allows writing the Stokes parameters in terms of the probabilities of performed measurements, $S_{ij} = 2^2 \sum_{m,n=1}^{4} (M^{-1})_{mn,ij} \ P_{mn}$ and, consequently, to express the density matrix in Equation 2.8 by

$$\rho_{AB} = \sum_{m,n=1}^{4} [\sum_{i,j=1}^{4} (M^{-1})_{mn,ij} \ \sigma_i^A \otimes \sigma_j^B] \ P_{mn} \tag{2.9}$$

Owing to imperfect experimental measurements such as small variations in the state preparation or imperfect measurement settings, the experimentally measured probabilities can produce a non-physical density matrix with negative eigenvalues. To prevent this, we employ a maximum-likelihood method [28, 29].

The reconstruction of a density matrix not only provides a description of a quantum state but also allows one to compute useful physical quantities including quantitative measures of entanglement. The first measure of the amount of entanglement present in a physical system is the *concurrence (C)* [30]. For an arbitrary 2-qubit mixed state, C is defined as $max\{\ 0,\ \lambda_1 - \lambda_2 - \lambda_3 - \lambda_4\ \}$ where the λs are eigenvalues, in decreasing order, of the hermitian matrix $\sqrt{(\sigma_y \otimes \sigma_y)\rho^*(\sigma_y \otimes \sigma_y)\rho}$. C ranges from 0 for a separable state to the maximum value of 1 for a maximally entangled state. This quantity also directly leads to one of the operational entanglement measures called *entanglement of formation (EF)* [31] that quantifies how many maximally entangled states are required to prepare a quantum state ρ_{AB} by the relation $EF \equiv H(\frac{1+\sqrt{1-C^2}}{2})$ with the *Shannon* entropy, $H(x) \equiv -x\log_2 x - (1-x)\log_2(1-x)$. Concurrence is further connected to the value of the Bell-parameter (S), defined in the previous subsection, by $S = 2\sqrt{1 + C^2}$.

Entanglement Visibility

Members of one generalized class of two-qubit states, namely the Werner states [32], are described as

$$\rho_{AB} = V|\Phi^+\rangle\langle\Phi^+| + \frac{1-V}{4}\mathbb{I}, \tag{2.10}$$

where V is the, so called, visibility of the entangled state $|\Phi^+\rangle_{AB} = \frac{1}{\sqrt{2}}(|ee\rangle + |ll\rangle)$ and $\mathbb{I}$ is the 4×4 identity matrix. This state is the convex mixture of a maximally entangled state and white noise and is invariant under any unitary operation of the form $U \otimes U$, that is, $\rho_{AB} = (U_A \otimes U_B)\rho_{AB}(U_A^\dagger \otimes U_B^\dagger)$). The visibility is equal to 1 for the Bell states and 0 for the maximally mixed state. Experimentally, if the photonic time-bin entangled qubits written in Equation 2.3 are measured by the scheme shown in Figure 2.8, then the probability of joint detection can be represented as $P_{coin} = 1 + V\cos(\Delta\phi)$, where $\Delta\phi = \phi - \phi_A - \phi_B$. The visibility (V) can be computed by $V = (N_{AB}^{max} - N_{AB}^{min})/(N_{AB}^{max} + N_{AB}^{min})$, where $N_{max(min)}$ denotes maximum (minimum) counts of the joint detections as shown in Figure 2.9.

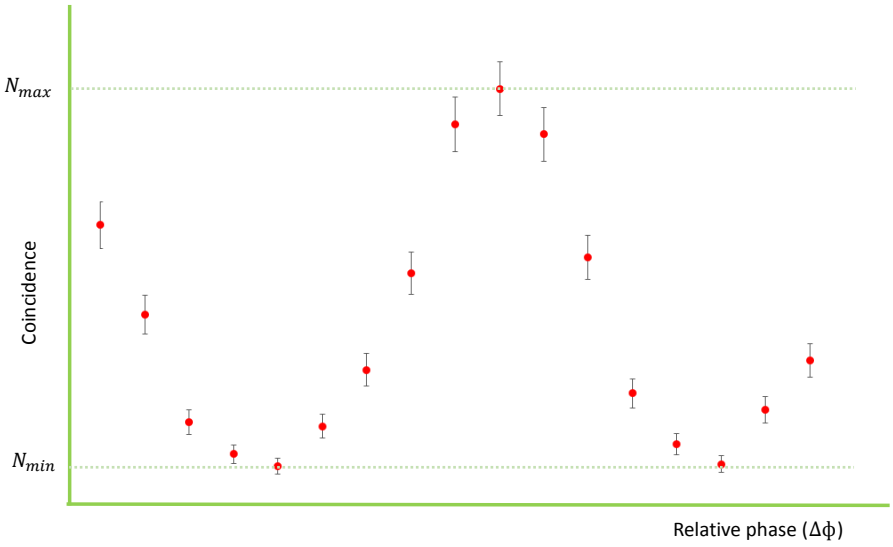

Figure 2.9: **Experimentally measured joint detections as shown in Figure 2.8.**

It is worth noting that the visibility of entanglement can be connected to concurrence (C). For the state in Equation 2.10, it is represented by $C = max\{(3V - 1)/2, 0\}$. The visibility can further be used to make statements of the inseparability and nonlocality of a quantum system. For instance, the Werner state is non-separable, i.e. entangled, if $V > 1/3$, and the

state reveals nonlocal properties if the visibility is greater than $1/\sqrt{2}$ as shown in Figure 2.10. The latter simply bridges the visibility and the CHSH-Bell parameter defined in Equation 2.7 by the relation, $S = 2\sqrt{2}\ V$. In addition, the state in Equation 2.10 can be parametrized in terms of fidelity (F), that is, $\rho_{AB} = \frac{4}{3}((F - \frac{1}{4})|\Phi^+\rangle\langle\Phi^+| + \frac{1-F}{4}\mathbb{I})$ where $0 \leq F \leq 1$. This allows to connect entanglement visiblility and fidelity, i.e. $F = (3V + 1)/4$.

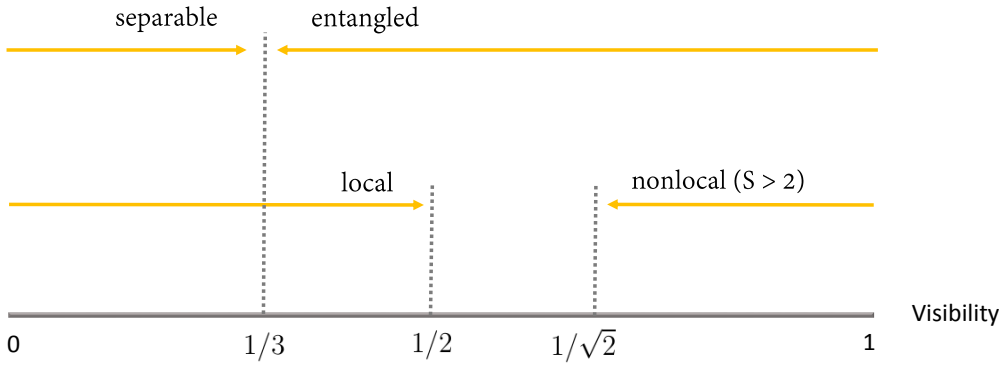

Figure 2.10: **Property of the Werner state in Equation 2.10 in terms of entanglement visibility [33].** Separability : a two-photon Werner state is entangled if V is greater than 1/3. Nonlocality : the state is nonlocal if V > 1/ $\sqrt{2}$.

2.2 Quantum Memory

2.2.1 Storage Materials and Protocols

Over the last decade, many quantum storage protocols have been implemented using various storage materials, including vapour cells, laser-cooled atoms, and impurities doped into crystals operated at cryogenic temperatures [34]. Here we will focus on the photon-echo based atomic frequency comb (AFC) quantum memory protocol [35], which is used in conjunction with our storage materials, a thulium (Tm)-doped $LiNbO_3$ waveguide and an erbium (Er)-doped optical fibre shown in Figure 2.11.

The principle of storage is based on the interaction of light with an atomic ensemble that features an inhomogeneously broadened optical transition. The broadening is due to the presence of defects in the solid-state host. The inhomogeneously broadend line is spectrally tailored into a series of equally-spaced narrow absorption peaks of width γ and spacing Δ, called an atomic frequency comb (AFC), as shown in Figure 2.12. We assume that the width of the inhomogeneously broadened absorption line is much larger than the homogenous linewidth of the individual peaks. If a single photon is absorbed by the spectrally-tailored atomic ensemble, then the absorption introduces a single collective excitation in all the atoms resonant with the light field. This is described by a collective Dicke state [36].

$$|\Psi\rangle = \frac{1}{\sqrt{N}} \sum_{j=1}^{N} c_j e^{i2\pi\delta_j t} e^{-ikz_j} |g_1, \cdots e_j, \cdots g_N\rangle \,. \tag{2.11}$$

Here, $|g_j\rangle$ ($|e_j\rangle$) denotes the ground (excited) state of atom j, δ_j is the detuning of the atom's transition frequency from the photon carrier frequency, z_j its position measured along the propagation direction of the light, and the factor c_j depends on the atom's resonance fre-

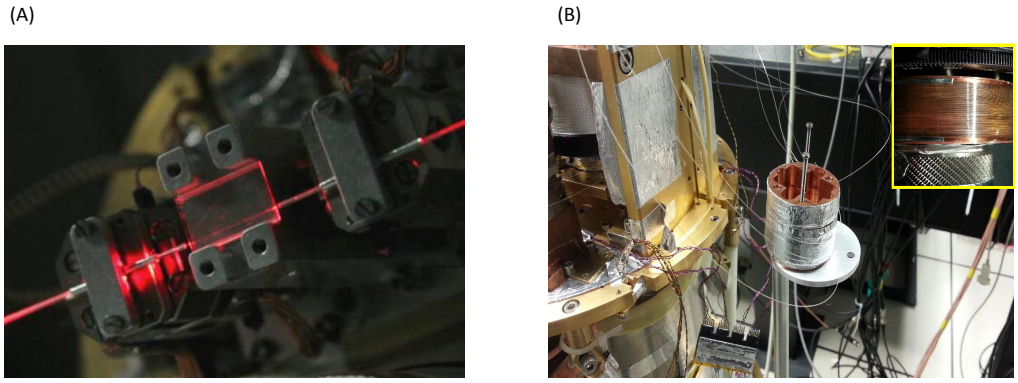

Figure 2.11: **Our quantum memories** (A) Thulium-doped $LiNbO_3$ waveguide. Laser light (red) is propagating through the waveguide. (B) A 20 m-long erbium-doped optical fibre spooled around a copper tube. The inset shows a zoom-in on the fibre spool.

quency and position. Note that the bandwidth of the input photon, γ_{ph}, should be bigger than the absorption peak separation and smaller than the AFC bandwidth (Γ), i.e., $\Delta < \gamma_{ph} < \Gamma$.

The coherence of the collective state will rapidly dephase as each individual atom posesses a different atomic transition frequency. However, if the detuning, δ_j, of the individual comb teeth is given by $\delta_j = m_j\Delta$, then the periodic structure of the absorption line causes rephasing of the state after multiples of the storage time $t_{storage} = 1/\Delta$, that is, the photon is re-emitted in the forward direction. This can easily be seen from Equation 2.11: if $t = t_{storage}$, all frequency dependent phase factors are zero (mod 2π) resulting in all individual excitations in the Dicke state to be in phase. Assuming Gaussian shaped comb teeth, the retrieval efficiency is given by [35]

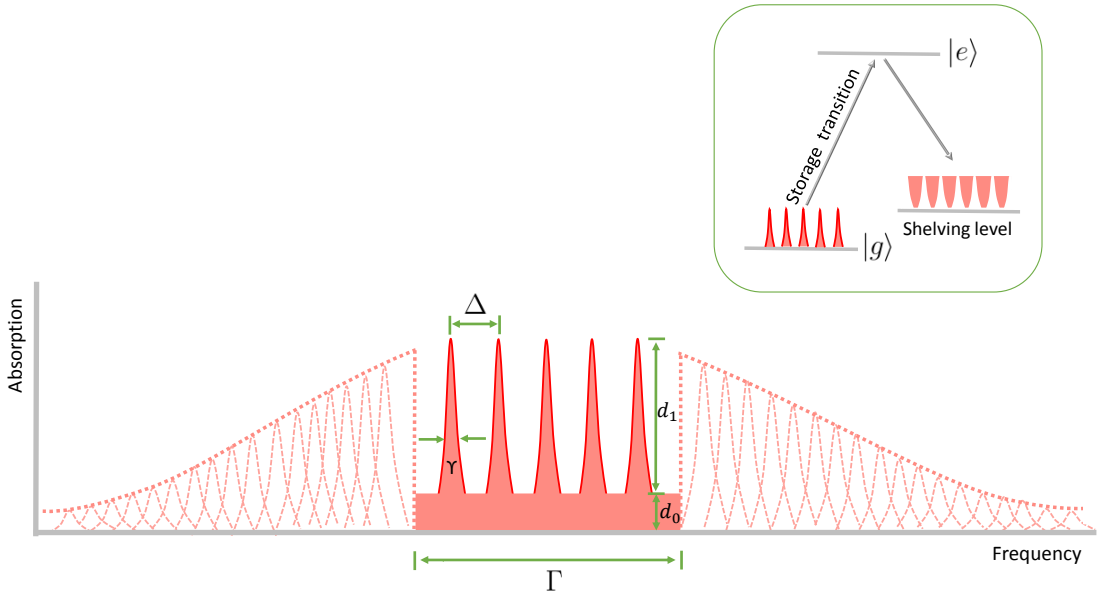

Figure 2.12: **Atomic frequency comb (AFC).** The main figure shows an atomic frequency comb tailored in an inhomogeneously broadened absorption line, and the inset shows the atomic level structure. $|g\rangle$ and $|e\rangle$ denote ground and excited state, respectively. To create the AFC, atoms are frequency-selectively pumped from $|g\rangle$ into a shelving level, whose lifetime must significantly exceed the lifetime of the excited state.

$$\eta_f = (d_1/F)^2 e^{-7/F^2} e^{-d_1/F} e^{-d_0}, \tag{2.12}$$

where d_1 and d_0 are the optical depths of the AFC and the atomic background, respectively (see Figure 2.12) and F denotes the finesse of the comb defined as $F = \Delta/\gamma$. Theoretically the achievable efficiency is limited to 54 % in the case of re-emission in the forward direction, due to re-absorption of the re-emitted photon in the storage medium. Up to 100 % recall efficiency is possible with retrieval in the backward direction [35].

To implement the AFC protocol, for instance in Chapter 5, a Tm : $LiNbO_3$ waveguide is

cooled down below 3 Kelvin. The cryogenic temperature is required in order to increase the coherence time of the optical transition between storage levels as well as the life-time of the shelving level which affects on storage time and efficiency. At higher temperatures interaction with the crystal lattice induces energy perturbation of electronic and magnetic levels. The coherence time of the optical transition and the life-time of shelving level (nuclear Zeeman state) were measured to be about 80 microsecond and 1 minute, respectively in our implementation. To initialize our memory, a coherent pulse of light pumps atoms from the ground state ($|g\rangle$) to the excited state ($|e\rangle$) such that some atoms form an AFC structure on $|g\rangle$ where the rest of the atoms are moved to a shelving level as shown in Figure 2.12. This can be implemented by frequency-selective optical pumping.

2.2.2 Figures of Merit

In order to access the performance of a quantum memory, several figures of merit have been established : bandwidth, recall efficiency, multiplexing capacity, storage time, and storage fidelity [34]. These indicate the fundamental performance of the memory, and also evaluate its suitability for quantum communication realizations in particular for use in a quantum repeater.

Bandwidth

When interfacing a single photon of width γ_{ph} with a memory, the spectral storage window, Γ, of the memory should be wider than the bandwidth of the photon, i.e. $\Gamma \gg \gamma_{ph}$. This ensures a faithful interaction of the photon over its entire spectrum. Hence, for high-rate quantum communication for which photonic waveforms must be short, the memory bandwidth is an important factor. Rare-earth ion-doped solid-state materials are generally good candidates for huge-bandwidth memories [37]. For instance, Tm:$LiNbO_3$ in principle allows

(if used in conjunction with the AFC protocol) the absorption of photons over a 300 GHz bandwidth, and for erbium-doped fibres the bandwidth is around 1300 GHz, clearly outperforming memories based on atomic vapor or laser cooled atoms and electromagnetically induced transparency (EIT)-based storage, for which the bandwidth is typically restricted to a few MHz [34].

Recall Efficiency

A photon stored in a quantum memory is retrieved with a certain probability, P. This probability defines the recall efficiency, η, of the memory. The efficiency is usually defined as P_{out}/P_{in}. Basically, the efficiency needs to be higher than the transmission of a quantum channel inducing the same delay, e.g. 1 - $10^{-\alpha(\frac{ct}{n})/10}$ for an optical telecommunication fibre with time $t = \frac{nL}{c}$ and attenuation coefficient $\alpha = 0.2dB/km$. For instance, the minimum required efficiency is found to be 0.01 to outperform L=100 kilometers of optical fibre transmission. Obviously, the higher η, the better the quantum repeater. In the case of AFC-based quantum memory, 59% of recall efficiency has been experimentally demonstrated [38]. With the AFC protocol, approaching unity efficiency is possible when a stored photon is retrieved in the backward direction [35]. High-efficient forward-direction recall is also feasible with a memory residing inside an impedance-matched cavity [39]. To date, the state-of-the-art for the retrieval efficiency of a solid-state quantum memory is 69% [40]. At the moment, our thulium- and erbium-doped quantum memories yield recall efficiencies of a few percent. This is mainly due to inefficient AFC preparation as non-zero absorption background (d_0) significantly diminishes the efficiency via the term e^{-d_0} in Equation 2.12. Together with improving the preparation of the AFC, our group is currently working on cavity-enhanced memory for higher recall efficiency.

Multiplexing Capacity

The multi-mode capacity describes a memory's capability to simultaneously store many qubits, all encoded in a different spatial, spectral, temporal or polarization mode. This capacity affects the time it takes to distribute entanglement across an elementary link in a repeater-based quantum channel, and thereby significantly impacts the communication rate. If we take multiplexing in the spectral domain, then a memory with 1 THz of total storage bandwidth would in principle enable storing 1,000 photons with 1 GHz bandwidths at the same time. Rare-earth doped solid-state atomic ensembles offer a high frequency multiplexing capacity as they can make use of inherently broadened inhomogeneous linewidth which is usually on the order of 100 GHz. In the case of AFC-based quantum memory, the ideal multiplexing capacity is given by the ratio between the inhomogeneously broadened total storage bandwidth (Γ_{inh}) and individual AFC bandwidth, i.e. Γ_{inh}/Γ, assuming neligible spacing between AFCs. Multiplexed quantum memories with 10 spatial modes [41], 26 spectral modes [42], 400 temporal modes [43] have been reported.

Storage Time

Unlike a classical storage device, the storage time of the AFC quantum memory is not infinite due to the limited coherence of the atomic system. In the AFC protocol, the spacing (Δ) between two neighboring absorption peaks defines the storage time and thus the homogeneous linewidth (γ), which is related to the coherence time as $T_2 = \frac{1}{\pi\gamma}$, becomes a fundamental factor for determining the maximum achievable storage duration. 29 microseconds storage of single-photon-level coherent light has been implemented using an AFC based solid-state spin-wave memory [44]. The storage time required varies depending on the tasks. For instance, a storage time of 500 micro-seconds is required in order to build a quantum repeater with 100 kilometers elementary link length [42]. To date, 16 seconds [45] and 1 minute [46] of storage time have been demonstrated using an ultracold atomic gas (Rb) confined in an

optical lattice and a solid-state material ($Pr : Y_2SiO_5$) based on EIT, respectively. It is worth to note that the storage time for the AFC protocol is predetermined by the tailored frequency-comb structure. Hence the AFC in this form is not capable of on-demand recall in the temporal domain. However, our group successfully implemented feed-forward controlled recall in the frequency domain, which for the purpose of a quantum repeater, is equivalent to on-demand recall in time domain [42].

Fidelity

Fidelity, F, indicates how similar one state is with respect to another by quantifying the amount of overlap between the two states. In the Bloch sphere picture shown in Figure 2.1, it measures the distance between two quantum states. For instance, in the case of pure states, it is $F = Tr(\rho_A \rho_B)$. When considering storage, this can be used to verify how faithful a memory preserves the quantum state during storage. The maximal achievable average fidelity using the best classical storage strategy for qubits encoded into a single photon is 2/3 [47]. It is worth noting that this value does not provide the correct bound if qubits are encoded into weak laser pulses. In this case, it turns out that the bound varies depending on the photon-number distribution and increases with increasing mean photon number as additional information can be extracted from measurements on multi-photon events. For Poissonian statistics, as an example, the classical fidelity is bounded by $F_{classical} = \sum_{N\geq 1} \frac{N+1}{N+2} \times \frac{P(\mu,N)}{1-P(\mu,0)}$ [48], assuming that the storage device has unity recall efficiency, and where $P(\mu, N) = e^{-\mu}\mu^N/N!$. N stands for the number of photons and μ is the mean photon number. This can even be further extended to the case of finite storage efficiency, as shown in [49]. In conclusion, to make sure that a memory is non classical, thus verifying quantum storage, the storage fidelity should exceed the relevant classical upper bound, which depends on the memory efficiency and the number statistics of the incident light.

An additional benchmark to beat is that of quantum cloning. Quantum cloning is a process that makes an exact copy of an arbitrary quantum state without any modification of the state. A perfect duplication is forbidden by the law of physics, i.e. the *no-cloning theorem* [50, 51]. The best known optimal cloning guarantees a fidelity as high as 5/6 [52].

In the included papers, the fidelity of our storage device is assessed via three different experiments. I. Information Storage (Chapter 5) : In this experiment, a single qubit encoded into a photon, $|\psi_{in}\rangle = a|0\rangle + b|1\rangle$, is sent into our memory, retrieved, and measured after storage. Since the qubit is expressed as a vector on a 3-dimensional Bloch sphere as shown in Figure 2.1, i.e. a pure state, the mean storage fidelity can be calculated as $\bar{F} \equiv \int d\psi_{in} \langle\psi_{in}|\rho_{out}|\psi_{in}\rangle$ $= \frac{1}{3}F_{pole} + \frac{2}{3}F_{equator}$ [53]. F_{pole} is easily computed as $P_{|\psi\rangle}/(P_{|\psi\rangle} + P_{|\psi^{\perp}\rangle})$ where $|\psi\rangle$ is the input state and $P_{|\psi\rangle}(P_{|\psi^{\perp}\rangle})$ denotes the probability for the input state to be projected onto $|\psi\rangle(|\psi^{\perp}\rangle)$. Here $|\psi^{\perp}\rangle$ denotes the orthogonal state with respect to $|\psi\rangle$. By scanning the measurement basis on the equator of the Bloch sphere $F_{equator}$ can be obtained as $F_{equator} = (1+V)/2$, where V is the visibility of count measurement along the equator. The relation is found by the definition of storage fidelity, i.e. $\langle\psi_{in}|\rho_{out}|\psi_{in}\rangle$, with the density matrix of recalled output state expressed in terms of visibility as $\rho_{out} = \frac{1}{2}(\mathbb{I} + V\vec{n}\cdot\vec{\sigma})$ where $\vec{n}$ and $\vec{\sigma}$ denote a vector on the Bloch sphere and the Pauli vector defined in Chapter 2. Alternatively one may simply equalize the two definitions for the output state density matrix : $\rho_{out} = V|\psi\rangle\langle\psi| + (\frac{1-V}{2})\mathbb{I}$ and $\rho_{out} = F|\psi\rangle\langle\psi| + (1-F)|\psi^{\perp}\rangle\langle\psi^{\perp}|$.

II. Entanglement Storage (Chapter 6, 7) : Secondly, we consider the storage of entanglement. In the experiments described in Chapter 6 and 7, we reconstruct density matrices of the states before (ρ) and after (ρ') storage, which as considered in Chapter 2 allows one to directly calculate the storage fidelity for two mixed quantum states : $F \equiv [\mathrm{Tr}(\sqrt{\sqrt{\rho}\rho'\sqrt{\rho}})]^2$,

originally defined as Uhlmann's transition probability [54, 55].

III. Wavefunction storage (Chapter 8) Finally, in order to determine if the storage device preserves the wavefunction of the photons we consider a two-photon measurement performed after photons are mapped into and out of a memory. As in case I, we mathematically formulate the operation of the memory as $|\psi\rangle\langle\psi| \rightarrow F|\psi\rangle\langle\psi| + (1-F)|\psi^{\perp}\rangle\langle\psi^{\perp}|$ and by expressing the degree of two-photon interference, which is experimentally measureable, in terms of the fidelity, one can derive the memory fidelity. This is further discussed in Chapter 8 and a detailed calculation is available in Appendix C.

2.3 Two-Photon Measurement

2.3.1 Two-Photon Interference

As a start, let us consider the interference between two perfect single photons. When two indistinguishable single photons impinge on a lossless symmetric beam-splitter from different input ports, they bunch and leave together by the same output port due to destructive interference, i.e. π-phase difference, between the probability amplitudes associated with both input photons being transmitted or both reflected. This is expressed mathematically as :

$$A^\dagger B^\dagger |00\rangle_{AB} = (\frac{C^\dagger + iD^\dagger}{\sqrt{2}})(\frac{iC^\dagger + D^\dagger}{\sqrt{2}})|00\rangle_{CD} = \frac{i}{\sqrt{2}}(|20\rangle_{CD} + |02\rangle_{CD}). \tag{2.13}$$

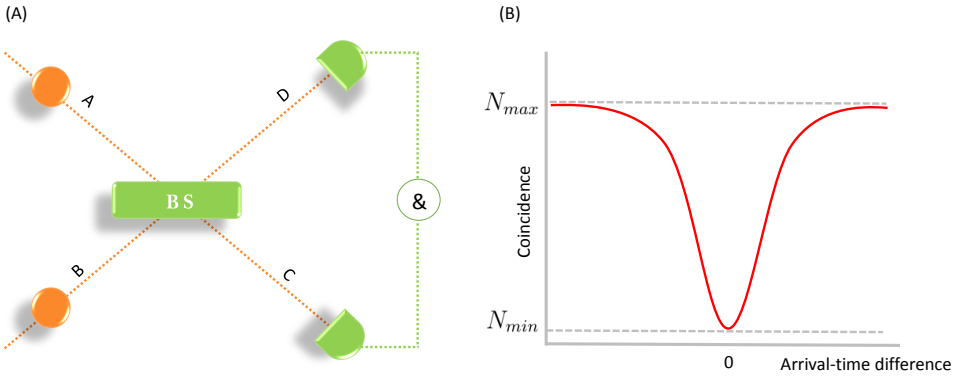

Figure 2.13: **Two-photon interference.** (A) A schematic diagram of two-photon interference. BS and & denote a lossless symmetric beam splitter and a joint detection between two detectors placed at the outputs of the BS, respectively. (B) The rate of the joint detections as a function of the arrival-time difference between two input photons at the BS. $N_{max(min)}$ denotes the maximum (minimum) coincidence rate.

This phenomenon is known as the Hong-Ou-Mandel (HOM) effect [56]. A schematic diagram of the effect is shown in Figure 2.13 (A). Since no such interference occurs for distinguishable input photons, the interference visibility V provides a convenient way to verify that two photons are indistinguishable in all degrees of freedom. The visibility is defined as $V = (N_{\max} - N_{\min})/N_{\max}$, where $N_{\min}$ and $N_{\max}$ denote the number of detections, as shown in Figure 2.13 (B), with which photons are found in the two output ports in coincidence if the incoming photons are indistinguishable and distinguishable, respectively. When the incident photons are completely distinguishable (indistinguishable), the visibility ideally reaches the value of 0 (1). In reality, however, the quality of the interference can be degraded even with perfectly indistinguishable photons due to experimental imperfections. One experimental limiting factor, for instance, depends on the ratio between temporal uncertainty (ΔT) of photons' generation and the coherence time ($\Delta\tau$) of the photons, with the maximally achievable visibility given by $V = 1/\sqrt{1 + (\frac{\Delta T}{\Delta \tau})^2}$ [57, 58] . This approaches unity when $\Delta T \ll \Delta\tau$ and slowly decreases as ΔT increases. It is also worthwhile to note that, owing to multi-photon contributions, the interference visibility only reaches 1/2 [59] and 1/3 [60] when using light with the Poissonian- and thermal-statistics, respectively.

The HOM effect is found to be useful in various applications. The state in Equation 2.13, known as the two-photon *NOON* state [61], is used to precisely measure phase down to the so-called *Heisenberg* limit (quadratic improvement over standard quantum limit) when used in optical interferometer [62]. This makes the effect important in the concept of quantum lithography [63] and metrology [64]. In addition, as the HOM effect reveals photonic similiarity between two photons, it is used to verify the purity of two independently generated photons. This has been employed with single photons generated from varioius materials including trapped ions [65], quantum dots [66, 67, 68], and nitrogen-vacancy centers in diamond [69, 70].

In Chapter 8, two-photon interference is charaterized with photons that are recalled from two independent quantum memories in order to investigate the capability of our memory for preserving the photonic wavefunction during storage, thus guaranteeing successful BSM with the recalled photons. The measurement is performed with respect to the spectral, temporal, and polarization degrees of freedom. Since we observe that the visibility of the interference with and without the memories are the same to within experimental uncertainties with respect to all the aforementioned degrees, we conclude that our memory does not modify the wavefunction of photons during storage.

2.3.2 Bell-State Measurement

The BSM erases "which-photon" information by projecting two independent photons that have never interacted onto one of the *Bell* states : $|\Phi^{\pm}\rangle = \frac{1}{\sqrt{2}}(|ee\rangle \pm |ll\ \rangle)$ and $|\Psi^{\pm}\rangle = \frac{1}{\sqrt{2}}(|el\ \rangle \pm |le\rangle)$. To date, no method is known to unambiguously distinguish all four Bell states without losing any measurement events, i.e. with 100% efficiency. As BSMs are required in order to interconnect elementary repeater links, its operational efficiency significantly influences the performance of a quantum repeater in terms of the entanglement distribution rate. Thus, the BSM efficiency as well as ability to distinguish Bell states becomes important in building a high-efficient quantum repeater.

For better understanding how a BSM is implemented, let us consider two time-bin qubits with a temporal separation of Δt impinging onto a single beam splitter from different input modes. One possible projection is onto $|\Psi^{-}\rangle$. This happens when two photons are found in different output modes at different times, i.e. $|el\ \rangle$ or $|le\rangle$ as shown in Figure 2.14 (A). This is because the measurement is only possible when the two photons are either both transmitted or reflected at the beam splitter, causing a relative phase difference of π between the events.

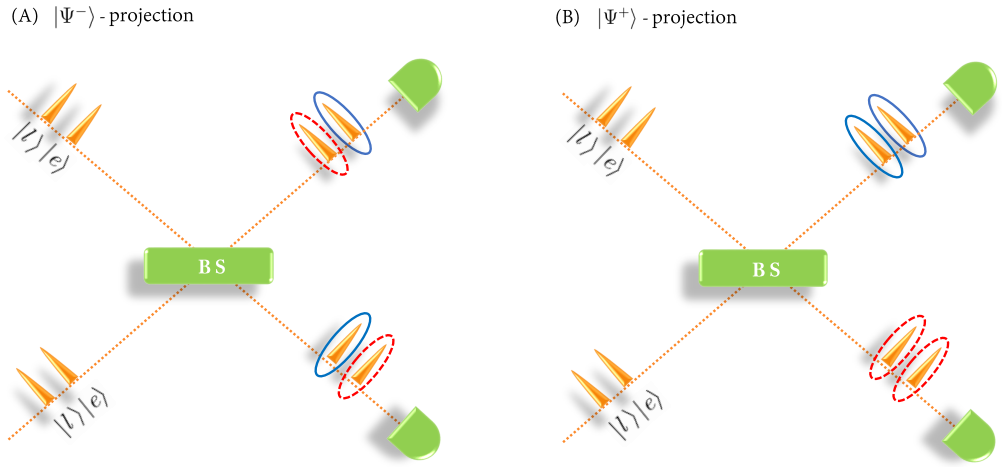

Figure 2.14: **A photonic Bell-state measurement.** BS denotes a lossless symmetric beam splitter. (A) A projection onto $|\Psi^-\rangle$. This happens if each photon in different temporal mode is found at different output ports, i.e. either dotted red or solid blue circles. (B) A projection onto $|\Psi^+\rangle$. This happens if each photon in different temporal mode is found at the same output port, either dotted red or solid blue circles.

Note that if a photon impinges on a beam splitter there is $\pi/2$-phase difference between transmission and reflection amplitude due to the unitarity of the beam-splitting operation [71]. Another possible projection with a single beam splitter is onto $|\Psi^+\rangle$. This happens if two photons are found in the same output mode but at different times as shown in Figure 2.14 (B). This implies that, to detect both photons at a single detector, the recovery time of the detector should be shorter than the separation of two temporal modes. However, for the experiment described in Chapter 8, the re-activation time of the employed superconducting nanowire single-photon detector is not short enough to perform a $|\Psi^+\rangle$-projection with our time-bin qubits. In order to project onto the remaining two Bell states, $|\Phi^+\rangle$ and $|\Phi^-\rangle$, it is necessary to find detection events where two photons are present in the same temporal and output mode. However, it is not possible to unambiguously discriminate, which detection belongs to which state with only a single beam splitter. Thus, a successful BSM occurs only for two out of the four possible projections or in other words 50% of the time. Note that

it is known that the 50% BSM efficiency (η_{BSM}) is the highest possible with linear optics [72].

Discriminating all four Bell states has been demonstrated with the aid of frequency sum generation [73]. However, due to the nonlinear conversion process, the effciency of the BSM was very low. Recently, it has been proposed that 75% of BSM efficiency can be achieved if two ancillary photons and photon number resolving detectors are involved [74]. In the proposal, the efficiency approaches unity as the number of anicillary photons and the detectors increase to infinity : $\eta_{BSM} = 1 - \frac{1}{2}^N$ with 2^N of photons and detectors. Due to technical difficulties, no experimental BSM with greater than 50% effciency has been reported to date.

Bibliography

[1] C. H. Bennett, G. Brassard, C. Crepeau, R. Jozsa, A. Peres, and W. K. Wootters, Phys. Rev. Lett. 70, 1895 (1993)

[2] S. Pironio, A. Acin, S. Massar, A. Boyer de la Giroday, D. N. Matsukevich, P. Maunz, S. Olmschenk, D. Hayes, L. Luo, T. A. Manning, C. Monroe, Nature 464, 1021 (2010)

[3] J. Brendel, N. Gisin, W. Tittel, and H. Zbinden, Phys. Rev. Lett. 82, 2594 (1999)

[4] W. Tittel and G. Weihs, Quantum Information and Computation 1, 3 (2001)

[5] E. Schrodinger, Naturwissenschaften 23, 807 (1935)

[6] R. F. Werner, Phys. Rev. A 40, 4277 (1989)

[7] C. H. Bennett, D. P. DiVincenzo, J. Smolin, and W. K. Wootters, Phys. Rev. A 54, 3824 (1996)

[8] K. Modi, A. Brodutch, H. Cable, T. Paterek, and V. Vedral, Rev. Mod. Phys. 84, 1655 (2012)

[9] E. Megidish, A. Halevy, T. Shacham, T. Dvir, L. Dovrat, and H. S. Eisenberg, Phys. Rev. Lett. 110, 210403 (2013)

[10] A. I. Lvovsky, arXiv : 1401.4118 (2014)

[11] P.G Kwiat, E. Waks, A.G. White, I. Appelbaum, and P.H. Eberhard, Phys. Rev. A 60, 773 (1999)

[12] D. H. Jundt, Optics Lett. 22, 1553 (1997)

[13] I. Marcikic, H. de Riedmatten, W. Tittel, V. Scarani, H. Zbinden, N. Gisin, Phys. Rev. A 66,062308 (2002)

[14] D. Bohm, Quantum Theory. PrenticeHall (1951)

[15] A. Einstein, B. Podolsky, and N. Rosen, Phys. Rev. 47, 777 (1935)

[16] J. S. Bell, Physics 1 195 (1964)

[17] J. F. Clauser, M.A. Horne, A. Shimony, R.A. Holt, Phys. Rev. Lett. 23, 880 (1969)

[18] J. S. Bell, Introduction to the hidden variable question, Proceedings of the International School of Physics 'Enrico Fermi', Course IL, Foundations of Quantum Mechanics 171 (1971)

[19] J. F. Clauser, M.A. Horne, Phys. Rev. D 10, 526 (1974)

[20] V. Scarani, Ultracold Gases and Quantum Information, 105, Oxford (2011)

[21] N. Brunner, D. Cavalcanti, S. Pironio, V. Scarani, S. Wehner, Rev. Mod. Phys. 86, 419 (2014)

[22] P. H. Eberhard, Phys. Rev. A, 47, 747 (1993)

[23] G. Weihs, T. Jennewein, C. Simon, H. Weinfurter, and A. Zeilinger, Phys. Rev. Lett. 81, 5039 (1998)

[24] T. Scheidl, R. Ursin, J. Koer, S. Ramelow, X.-S. Ma, T. Herbst, L. Ratschbacher, A. Fedrizzi, N. K. Langford, T. Jennewein, A. Zeilinger, and W. D. Phillips, Proc. Natl. Acad. Sci. USA 107, 19708 (2010)

[25] M.A. Rowe, D. Kielpinski, V. Meyer, C.A. Sackett, W.M. Itano, C. Monroe, D.J. Wineland, Nature 409, 791 (2001)

[26] M. Giustina, A. Mech, S. Ramelow, B. Wittmann, J. Kofler, J. Beyer, A. Lita, B. Calkins, T. Gerrits, S. W. Nam, R. Ursin, and A. Zeilinger, Nature 497, 227 (2013)

[27] B. G. Christensen, K. T. McCusker, J. Altepeter, B. Calkins, T. Gerrits, A. Lita, A. Miller, L. K. Shalm, Y. Zhang, S. W. Nam, N. Brunner, C. C. W. Lim, N. Gisin, and P. G. Kwiat, Phys. Rev. Lett. 111, 130406 (2013)

[28] A. I. Lvovsky, M. G. Raymer, Rev. Mod. Phys. 81, 299 (2009)

[29] J. B. Altepeter, E. R. Jeffrey, P. G. Kwiat, Advances In Atomic, Molecular, and Optical Physics 52, 105 (2005)

[30] W. K. Wotters, Phys. Rev. Lett. 80, 2245 (1998)

[31] S. Hill, W. K. Wootters, Phys.Rev.Lett.78, 5022 (1997)

[32] R. F. Werner, Phys. Rev. A 40, 4277 (1989)

[33] D. Cavalcanti, A. Acin, N. Brunner, T. Vertesi, Phys. Rev. A 87, 042104 (2013)

[34] C. Simon, M. Afzelius, J. Appel, A. Boyer de la Giroday, S.J. Dewhurst, N. Gisin, C.Y. Hu, F. Jelezko, S. Kroll, J.H. Muller, J. Nunn, E. Polzik, J. Rarity, H. de Riedmatten, W. Rosenfeld, A.J. Shields, N. Skold, R.M. Stevenson, R. Thew, I. Walmsley, M. Weber, H. Weinfurter, J. Wrachtrup, and R.J. Young l. Eur. Phys. J. D, 58, 2010.

[35] M. Afzelius, C. Simon, H. de Riedmatten, and N. Gisin, Phys. REv. A 79, 052329

[36] R. H. Dicke, Phys. Rev. 93, 99 (1954)

[37] E. Saglamyurek et al., Nature 469, 512 (2011)

[38] M. Sabooni, Q. Li, S. Kroll, and L. Rippe, Phys. Rev. Lett. 110, 133604 (2013).

[39] M. Afzelius, C. Simon, Phys. Rev. A 82, 022310 (2010)

[40] M. P. Hedges, J. J. Longdell, Y. Li, and M. J. Sellars. Efficient quantum memory for light, Nature 465, 1052 (2010)

[41] S.-Y. Lan, A. G. Radnaev, O. A. Collins, D. N. Matsukevich, T. A. B. Kennedy, and A. Kuzmich, Opt. Express 17, 13639 (2009)

[42] N. Sinclair, E. Saglamyurek, H. Mallahzadeh, J. A. Slater, M. George, R. Ricken, M. P. Hedges, D. Oblak, C. Simon, W. Sohler, W. Tittel , arXiv : 1309.3202

[43] M. Bonarota, J. L. Le Gouet, and T. Chaneliere, New J. Phys. 13, 013013 (2011)

[44] N. Timoney, I. Usmani, P. Jobez, M. Afzelius, and N. Gisin, arXiv:1301.6924

[45] Y. O. Dudin, L. Li, and A. Kuzmich, Phys. Rev. A 87, 031801 (2013)

[46] G. Heinze, C. Hubrich, and T. Halfmann, Phys. Rev. Lett. 111, 033601 (2013)

[47] S. Massar and S. Popescu, Phys. Rev. Lett. 74, 1259 (1995)

[48] H. P. Specht, C. Nlleke, A. Reiserer, M. Uphoff, E. Figueroa, S. Ritter, and G. Rempe, Nature 473, 190 (2011)

[49] M. Gndoan, P. M. Ledingham, A. Almasi, M. Cristiani, H. de Riedmatten, Phys. Rev. Lett. 108, 190504 (2012)

[50] W. Wootters and W. Zurek, Nature 299, 802 (1982)

[51] D. Dieks, Phys. Lett. A 92, 271 (1982)

[52] V. Buek and M. Hillery, Phys. Rev. A 54, 1844 (1996)

[53] I. Marcikic, H. de Riedmatten, W. Tittel, H. Zbinden, N. Gisin, Nature 421, 509 (2003)

[54] A. Uhlmann, Rep. Math. Phys. 9, 273 (1976)

[55] R. Jozsa, J. Mod. Opt. 42, 2315 (1994)

[56] C. K. Hong, Z. -Y. Ou, and L. Mandel, Phys. Rev. Lett. 59, 2044 (1987)

[57] M. Zukowski, A. Zeilinger, and H. Weinfurter, Annals of the New York academy of Sciences 755, 91 (1995).

[58] J. G. Rarity, Annals of the New York academy of Sciences 755, 624 (1995).

[59] J. G. Rarity, P. R. Tapster and R. Loudon, J. Opt. B 7, 171 (2005)

[60] H. de Riedmatten, I. Marcikic, W. Tittel, H. Zbinden, N. Gisin, Phys. Rev. A 67, 022301 (2003)

[61] B. C. Sanders, Phys. Rev. A 40, 2417 (1989)

[62] V. Giovannetti, S. Lloyd, L. MacCone, Nature Photonics 5, 222 (2011)

[63] A. N. Boto, P. Kok, D. S. Abrams, S. L. Braunstein, C. P. Williams, and J. P. Dowling, Phys. Rev. Lett. 85, 2733 (2000)

[64] H. Lee, P. Kok, and J. P. Dowling, J. Mod. Opt.49, 2325 (2002)

[65] P. Maunz, D. L. Moehring, S. Olmschenk, K. C. Younge, D. N. Matsukevich, and C. Monroe, Nature Photonics 3, 538 (2007)

[66] K. Sanaka, A. Pawlis, T. D. Ladd, K. Lischka, and Y. Yamamoto, Phys. Rev. Lett. 103, 053601(2009)

[67] R. B. Patel, A. J. Bennett, I. Farrer, C. A. Nicoll, D. A. Ritchie, and A. J. Shields, Nature Photonics 4, 632 (2010)

[68] E. B. Flagg, A. Muller, S. V. Polyakov, A. Ling, A. Migdall, G. S. Solomon, Phys. Rev. Lett. 104, 137401 (2010)

[69] H. Bernien, L. Childress, L. Robledo, M. Markham, D. Twitchen, and R. Hanson, Phys. Rev. Lett. 108, 043604 (2012)

[70] A. Sipahigil, M. L. Goldman, E. Togan, Y. Chu, M. Markham, D. J. Twitchen, A. S. Zibrov, A. Kubanek, and M. D. Lukin, Phys. Rev. Lett. 108, 143601 (2012)

[71] C. H. Holbrow, E. Galvez, and M. E. Parks, Am. J. Phys. 70, 260 (2002)

[72] N. Ltkenhaus, J. Calsamiglia, K-A. Suominen, Phys. Rev. A 59, 3295 (1999)

[73] Y. -H. Kim, S. P. Kulik, and Y. Shih, Phys. Rev. Lett. 86, 1370 (2001)

[74] W. P. Grice, Phys. Rev. A 84, 042331 (2011)

Chapter 3

Real-World Entanglement

Quantum entanglement plays a key role in various applications of quantum communication including advanced secret-key distribution protocols such as measurement-device-independent quantum key distribution (MDI-QKD) [1, 2] and device-independent QKD [3] making the security of the shared key independent of involved measurements and all devices, respectively. Moreover, entanglement is widely used for various fundamental tasks including quantum teleportation [4], random number certification [5] and system dimension witness [6, 7, 8].

If entangled photons, possibly distributed using a quantum repeater, are used to establish secret keys, each user measures his/her own photon in order to generate classical bits . With the aid of well-known classical techniques, i.e. error correction and privacy amplification, the users are able to distill and share a secret key for secure communication and the security of this entanglement-based QKD is guaranteed by the violation of the Bell inequality as explained in Chapter 1. This Chapter describes a distribution of photonic entangled qubits in a real-world setting over a 12.4 kilometers underground optical fibre link, established between the University of Calgary and the Southern Alberta Institute of Technology (SAIT) Polytechnic, and demonstrates the nonlocal nature of the entanglement by violating the Clauser-Horne-Shimony-Holt (CHSH)-Bell inequality. This means that if entanglement is established between distant real-world users via a quantum repeater then it can be used for secure communication. Furthermore, in our implementation, each qubit is encoded into different degrees of freedom, i.e. polarization and time, thus revealing the robustness of entanglement. In the context of heterogeneous quantum networks [9], the hybrid photonic entanglement can interface with different types of quantum bits.

In this Chapter, the experiment was conducted in collaboration with Félix Bussières and Joshua A. Slater and supervised by Nicolas Godbout and Wolfgang Tittel. I contributed to this study in the following stages : characterizing the spectral features of the entangled photons as well as performing the measurements.

Physical Review A 81, 052106 (2010)

Testing nonlocality over 12.4 km of underground fiber with universal time-bin qubit analyzers

Félix Bussières[1,2], Joshua A. Slater[1], Jeongwan Jin[1], Nicolas Godbout[2], and Wolfgang Tittel[1]

[1] *Institute for Quantum Information Science, and Department of Physics and Astronomy, University of Calgary, 2500 University Drive NW, Calgary, Alberta T2N 1N4, Canada*

[2] *Laboratoire des fibres optiques, Département de génie physique, École Polytechnique de Montréal, C.P. 6079, Succursale Centre-Ville, Montréal, Québec, H3C 3A7 Canada*

Abstract

We experimentally demonstrate that the nonlocal nature of time-bin entangled photonic qubits persists when one or two qubits of the pair are converted to polarization qubits. This is possible by implementing a novel Universal Time-Bin Qubit Analyzer (UTBA), which, for the first time, allows analyzing time-bin qubits in any basis. We reveal the nonlocal nature of the emitted light by violating the Clauser-Horne-Shimony-Holt inequality with measurement bases exploring all the dimensions of the Bloch sphere. Moreover, we conducted experiments where one qubit is transmitted over a 12.4 km underground fiber link and demonstrate the

suitability of our scheme for use in a *real-world* setting. The resulting entanglement can also be interpreted as hybrid entanglement between different types of degrees of freedom of two physical systems, which could prove useful in large scale, heterogeneous quantum networks. This work opens new possibilities for testing nonlocality and for implementing new quantum communication protocols with time-bin entanglement.

3.1 Introduction

Quantum physics allows physical systems to be correlated in a way that is impossible to describe using a local variable model [10]. In the case of two physical systems, nonlocal correlations can be produced when they are entangled. From a practical point of view, entanglement is also a powerful resource for the field of quantum communication [11, 12]. Specifically, photonic entanglement is appealing as it can easily be distributed and, when combined with quantum memories [13], it can be swapped [14] to create a quantum repeater [15] needed to extend the distribution of quantum states over arbitrarily long distances [16]. Furthermore, in the context of a large scale, heterogeneous quantum network [9], photonic entanglement could be used to interface different types of quantum links, encodings, wavelengths and quantum memories. Fortunately, as photonic entanglement exists independently of the choice of encoding, it should persist even if these encoding are converted into each other [17]. Photonic entanglement between a polarization qubit and a linear momentum qubit has been shown recently [18, 19, 20]. While this is interesting for the purpose of quantum computing [21, 22], the linear momentum encoding is badly suited for long distance transmission as it requires phase stability between two spatial modes. To this end, the polarization and time-bin encodings are much better suited [23, 24].

In this article, we experimentally demonstrate that entanglement persists when one or both qubits of a time-bin entangled pair are converted to polarization qubits (for a recently re-

ported, similar investigation see [25]). Furthermore, this enables the measurement of time-bin entangled qubits in arbitrary bases, as shown in Fig. 3.1-a. This qubit conversion is possible by implementing a Universal Time-Bin Qubit Analyzer (UTBA), proposed in [26]. If one part of one of the two UTBAs is placed next to the source, as described in Fig. 3.1-b, this modified source generates hybrid entanglement between a time-bin qubit and polarization qubit.

We reveal the presence of entanglement through the violation of the Clauser-Horne-Shimony-Holt (CHSH) inequality [27] with a variety of measurement settings exploring all the dimensions of the Bloch sphere.

Finally, we demonstrate the persistence of entanglement when one of the qubits travels through an underground 12.4 km fiber link installed between two locations physically separated by 3.3 km.

Importance of a UTBA is twofold. First, it constitutes a versatile tool to implement quantum communication protocols with time-bin qubits. This is exemplified by our recent implementation of a new loss-tolerant quantum coin-flipping protocol [28, 29]. Second, it should prove

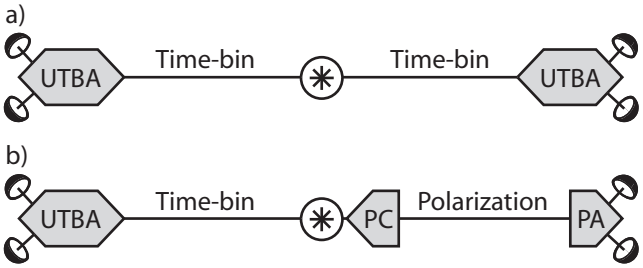

Figure 3.1: a) Source of time-bin entangled qubits, represented by the circled asterisk, with UTBAs, b) A source of hybrid entanglement is obtained by splitting apart one UTBA into a time-bin-to-polarization converter (PC) and a polarization analyzer (PA).

useful to experimentally violate a Leggett-type inequality [30, 31, 32] with time-bin entangled qubits. Indeed, these inequalities require the ability to project qubits onto bases that span all the dimensions of the Bloch sphere in order to rule out nonlocal models than can violate Bell-type inequalities but cannot reproduce all the predictions of quantum mechanics. From a more general point of view, this source can also be seen as an interface between heterogeneous quantum communication links, namely free-space and fiber links with possibly different types of encodings and wavelengths, and it should prove useful for quantum networking in general.

3.2 Experiment

We begin by describing the principle of the UTBA, both in its free-space and fiber optics versions. We recall that a time-bin qubit [33] denotes a single photon in superposition of being emitted in two well defined time windows of width Δt, separated by time $\tau > \Delta t$, that we shall label *early* $|e\rangle$ and *late* $|\ell\rangle$:

$$|\psi\rangle = \cos\theta\,|e\rangle + \mathrm{e}^{i\phi}\sin\theta\,|\ell\rangle\,. \tag{3.1}$$

Note that both basis states have identical polarization. Usually, experiments with time-bin qubits resort to "standard" time-bin qubit analyzers that restrict the possible measurement bases. These operate by converting the time-bin qubit into a superposition of a photon travelling along the short and long arms of an unbalanced Mach-Zehnder interferometer, and then detecting it behind a 50/50 beamsplitter. In this way, the time-bin qubit can be measured either in bases formed by states $\frac{1}{\sqrt{2}}(|e\rangle \pm \mathrm{e}^{i\phi}\,|\ell\rangle)$, where ϕ can be selected by modulating the interferometer's path length difference, or it can be projected onto $|e\rangle$ or $|\ell\rangle$. While this is sufficient to show violation of the CHSH inequality [24] or to implement entanglement based quantum key distribution with the BB84 protocol [34], it does not allow one to perform other tasks that require projecting on states corresponding to uneven super-

positions of $|e\rangle$ and $|\ell\rangle$.

In order to project a time-bin qubit onto any basis, one approach is to convert it first to a polarization qubit and then select the basis using wave plates and a polarizing beamsplitter (PBS), as proposed in [26].

Fig. 3.2-a shows the free-space UTBA designed for a wavelength around 810 nm that we built for this experiment. The polarization of the incoming time-bin qubit is first rotated using the half-wave plate HWP1 to 45° with respect to the linear polarization transmitted by the input polarizing beamsplitter PBS1. Each time-bin qubit component is then separated equally and travels along the short and long arms of a folded Mach-Zehnder interferometer using retroreflectors, featuring a travel time-difference $\tau = 1.4$ ns. After being transmitted through the quarter-wave plates QWP1 and QWP2, the light exits through PBS1. At this point, the photon emerges in three chronologically ordered time slots separated by τ that we label *early*, *middle* and *late*. In the middle slot, the initial time-bin qubit is mapped onto a polarization qubit, i.e. $|\psi\rangle \rightarrow \cos\theta\,|V\rangle + \mathrm{e}^{i(\phi+\phi_A)}\sin\theta\,|H\rangle$, where ϕ_A is an additional phase picked-up in the interferometer. This polarization qubit is then analyzed in any basis using the quarter-wave plate QWP3 followed by the half-wave plate HWP2, the polarizing beamsplitter PBS2 and the Si-based single photon detectors S_1 and S_2. For increased thermal stability, the optical components of the interferometer are glued on a Zerodur glass plate with a nearly zero linear thermal expansion coefficient. The glass plate is enclosed in a temperature controlled box. To realize the source of hybrid entanglement described in Fig. 3.1-b, one would physically separate QWP3, HWP2, PBS2 and the detectors from the rest and implement a proper transmission link in between.

The fiber optics version of the UTBA, designed for a wavelength around 1530 nm, is shown

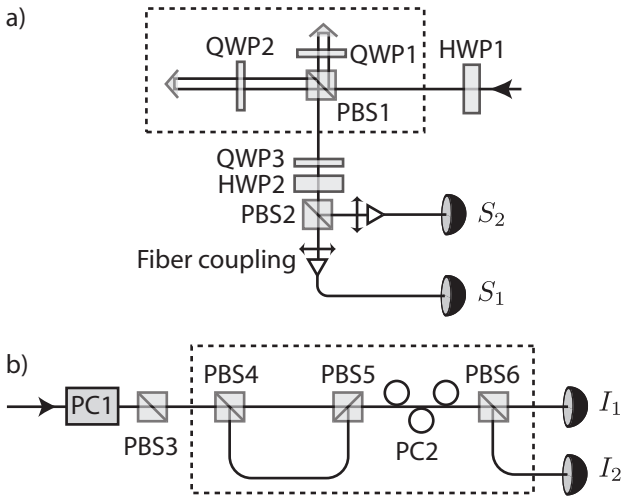

Figure 3.2: a) Free-space UTBA, b) Fiber optics UTBA. The dashed boxes show the sections that were enclosed in a temperature controlled box.

in Fig. 3.2-b. First, the polarization controller PC1 is used to maximize the transmission through PBS3. The output of PBS3 is a polarization maintaining fiber that is connected to the input port of PBS4 with its slow axis is aligned at 45° with respect to the transmitted polarization. The outputs of PBS4 couple light into the slow axis of the short and long polarization maintaining fibers of the Mach-Zehnder interferometer that also features the travel time-difference τ. A section of the long arm is wrapped and glued around a circular piezo actuator that is used to control the relative optical phase accumulated during transmission through the two arms of the interferometer. Both paths recombine at PBS5 and are coupled into a single mode fiber. Then, a *Lefèvre* polarization controller PC2 [35] and PBS6 are used to select the measurement basis in the middle time slot, and detection occurs in one of the InGaAs-based single photon detectors I_1 or I_2. The interferometer was placed in a temperature controlled box for increased stability.

The alignment of the paddles of PC2 was performed in the following way. First, a strong pulse of light prepared in the early time-bin was sent into the interferometer. Let us consider

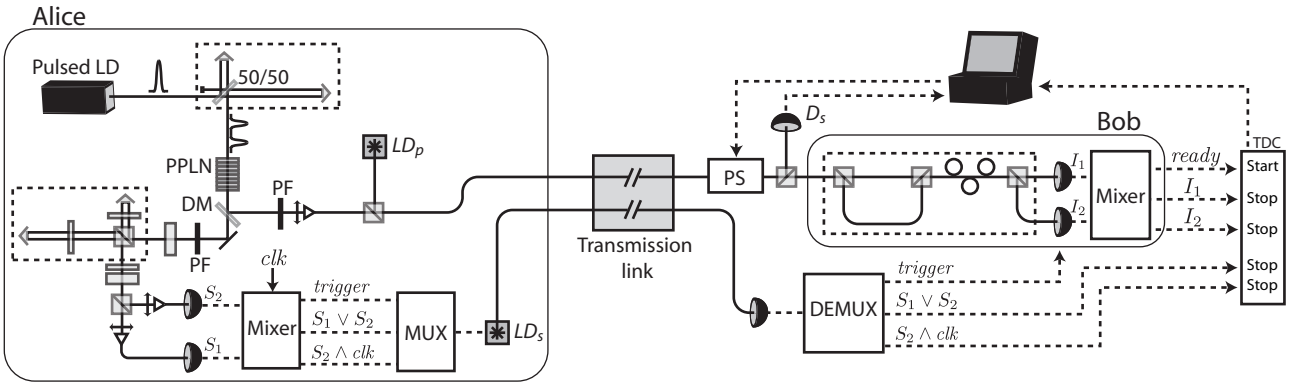

Figure 3.3: A laser diode generates 50 ps pulses at 530.6 nm wavelength and 20 MHz repetition rate that are sent through a folded Mach-Zehnder interferometer with a travel time-difference of 1.4 ns. The pulses emerge in a balanced superposition of two well defined time-bins labelled *early* and *late* and then propagate into a nonlinear, periodically poled lithium niobate crystal (PPLN), thereby creating time-bin entangled qubits at 811.9 and 1531.4 nm wavelengths through spontaneous parametric downconversion. The two qubits are separated at the dichroic mirror (DM) and the pump is filtered out using high-pass filters (PF). The 811.9 nm qubit is measured directly at Alice's using her free-space UTBA. The 1531.4 nm qubit is coupled into the transmission link and sent to Bob, who measures it with his fiber UTBA. The travel time-difference of all three interferometers is the same within a fraction of the coherence time of the photons. Detection events are acquired by a time to digital converter (TDC) that measures delays between a start signal and several stop signals. The detection signals from Alice's free-running Si-based single photon detectors are pre-processed with an electronic mixer. When performing the experiment over the underground fiber link, the signals exiting the mixer are time-multiplexed (MUX) and used to trigger a laser diode LD_s. The laser pulses are sent over a second fiber link parallel to the one used for the single photon signals. The signals are time-demultiplexed at Bob's (DEMUX) and then used for synchronization and data processing. The *trigger* signal is generated when a detection at either S_1 or S_2 occurs and emerges synchronously with the laser clock (*clk*). This signal is used to gate Bob's InGaAs-based single photon detectors during a 7 ns activation window. The *ready* signal, which is emitted only when both detectors are ready to detect, is used to start the TDC. This ensures that the statistics are not biased by the dead-time of Bob's detectors. The stop signals $S_2 \wedge clk$ and $S_1 \vee S_2$, where $\wedge$ denotes the logical AND and $\vee$ the logical OR, are used to determine which detector clicked and at what time, respectively. The detections at I_1 and I_2 also serve as stop signals. This allows us to register all possible coincidence detection events in the middle time slot. The duration of the latter was narrowed down to a time that varied between 0.4 to 0.8 ns.

the component that travels through the short arm. After PBS4, its polarization is horizontal ($|H\rangle$). Let $\cos\theta\,|H\rangle + \mathrm{e}^{i\phi}\sin\theta\,|V\rangle$ be the polarization right before PBS5. The energy of the pulse transmitted through PBS5 can be monitored by replacing I_1 with a fast classical detector connected to an oscilloscope. By rotating the paddles, the area of the light pulse can be maximized: this indicates that $\theta = 0$. Then, the paddles can be rotated to reduce the area by a factor $\cos^2\theta$, which allows inferring the value of θ. Note that the value of ϕ cannot be measured in this way: this would require performing a complete polarization state analysis. However, as we explain later, our measurements did not require measuring the exact value of ϕ.

We note that this UTBA requires the polarization of the time-bin qubit to be set properly at the input. This may seem to defeat the purpose of using the time-bin encoding, which is immune to birefringence in the transmission link [33]. This is, however, not entirely true as the polarization at the input of the UTBA only requires to be set to horizontal up to an arbitrary phase, whereas polarization encoding requires the horizontal and vertical polarizations' relative phase to be set to zero, which is more challenging to achieve.

Our source of time-bin entangled qubits is detailed in Fig. 3.3. Time-bin entangled photonic qubits in the state

$$|\psi\rangle = \frac{1}{\sqrt{2}}\left(|e\rangle_A\,|e\rangle_B + |\ell\rangle_A\,|\ell\rangle_B\right) \tag{3.2}$$

were created, where $|e\rangle_{A(B)}$ and $|\ell\rangle_{A(B)}$ represent the *early* and *late* time-bin qubit states of Alice (Bob). The wavelength and FWHM bandwidth of Alice's qubit was measured using a monochromator and found to be 811.9 ± 1.6 nm. From energy conservation, and assuming a monochromatic pump, Bob's qubit is calculated to be encoded at 1531.4 ± 5.6 nm wavelength.

We performed two set of experiments. In the first one, Alice and Bob were placed side by side in our laboratory at the University of Calgary, and the transmission link was a 10 m polarization maintaining fiber that did not require any polarization alignment and stabilization. In the second set of experiments, Bob was placed in a laboratory at the Southern Alberta Institute of Technology (SAIT), 3.3 km from the U. of Calgary. The link was a 12.4 km underground single mode fiber featuring total loss of 7.3 dB. Polarization stabilization was performed using quantum frames and a fully automatized polarization stabilizer (PS) [36]. Specifically, each 10 s period was divided into a 0.4 s period used to send a 0.25 s reference light pulse with the 1536.47 nm laser diode LD_p (see Fig. 3.3), and a 9.6 s period during which entangled photons were sent. The reference pulse and time-bin qubits were orthogonally polarized and are combined into the link using a polarizing beamsplitter. At Bob's, the reference pulse passes through the polarization stabilizer PS (PSY-101 from General Photonics) and is then reflected through a PBS towards the synchronization detector D_s. The signal from D_s is used to trigger the computer that then enables PS during 50 ms. The pulse is used as a reference to adjust the polarization transformation of PS to maximize the transmission of the single photons through the PBS and through Bob's UTBA. This stabilization system ran uninterrupted throughout an entire day and did not require resetting.

3.3 Measurements and Results

To reveal the presence of entanglement, we first measured the entanglement visibility using projections that are depicted on great circles around the Bloch sphere. First, we positioned Alice's (Bob's) UTBA to measure in the basis $|\pm\rangle_{\phi_A} = \frac{1}{\sqrt{2}}(|e\rangle \pm e^{i\phi_A}|\ell\rangle)$ ($|\pm\rangle_{\phi_B} = \frac{1}{\sqrt{2}}(|e\rangle \pm e^{i\phi_B}|\ell\rangle)$). Then, the phase of Bob's UTBA was scanned by varying the voltage applied to the piezo actuator of Bob's UTBA, as illustrated in Fig. 3.4-a. The average visibilities obtained are $91.0 \pm 2.9\%$ with Bob beside Alice and $85.4 \pm 3.3\%$ with Bob at SAIT (Fig. 3.4-b). The decrease in the latter visibility is entirely due to a decreased signal to

noise ratio (i.e. photon loss during transmission). This measurement was used to calibrate the phase variation as a function of the voltage applied to the piezo actuator. We also used this measurement to assess the phase stability of the setup. We observed that, typically, the phase did not drift more than $\pi/10$ over 10 minutes, which we set to be the time limit for stability. Then, we positioned Bob's UTBA to project onto $|e\rangle$ and $|\ell\rangle$, and scanned Alice's UTBA to project onto bases aligned along the xz great circle of the Bloch sphere (Fig. 3.4-c). The average visibilities obtained are $95.6 \pm 1.9\%$ for Bob beside Alice and $88.4 \pm 3.2\%$ for Bob at SAIT (Fig. 3.4-d). We point out that this type of measurement is not accessible using a single "standard" time-bin qubit analyzer consisting of an unbalanced interferometer and nonpolarizing beamsplitters with fixed splitting ratios.

Next, we used our source to violate the CHSH inequality [27] using four configurations that demonstrate the universality of the UTBAs. For each configuration, Alice and Bob projected their qubits randomly onto one of two, configuration specific bases. Each measurement result was registered as either $+1$ or -1, and only coincidence detections, one detection at Alice's and one detection at Bob's, were considered. Alice and Bob repeated each experiment with many photons to collect sufficient statistics. We shall use the indices i and j, respectively, with $i, j \in \{1, 2\}$, to identify Alice's and Bob's measurement basis. Strictly speaking, the basis selection and the measurements should be space-like separated events. Moreover, the overall detection efficiency of Alice and Bob's transmission channels should be above a certain threshold [37, 38]. These conditions were not met in our experiment, and, as is the case in all Bell-inequality tests to date, the violations we obtained are not loophole-free.

The CHSH inequality reads

$$S_{CHSH} = |E_{11} + E_{12} + E_{21} - E_{22}| \leq 2, \tag{3.3}$$

where the correlation coefficient E_{ij} is given by

Table 3.1: Results of the CHSH inequality violations with the four different configurations shown in Fig. 3.5. Columns S_A and S_S show the values obtained with Bob beside Alice, and Bob at SAIT, respectively. Columns $\times\sigma_A$ and $\times\sigma_S$ show by how many standard deviations the inequality was violated. Each measurement of S_A (S_S) lasted 160 s (480 s).

Conf.	$S_A \pm \sigma_A$	$(\times\sigma_A)$	$S_S \pm \sigma_S$	$(\times\sigma_S)$
1	2.65 ± 0.09	7.7	2.44 ± 0.15	2.9
2	2.60 ± 0.08	7.5	2.40 ± 0.15	2.7
3	2.65 ± 0.09	7.5	2.39 ± 0.15	2.6
4	2.60 ± 0.10	6	2.39 ± 0.15	2.7

$$E_{ij} = \frac{N^{ij}_{++} + N^{ij}_{--} - N^{ij}_{+-} - N^{ij}_{-+}}{N^{ij}_{++} + N^{ij}_{--} + N^{ij}_{+-} + N^{ij}_{-+}}. \tag{3.4}$$

N^{ij}_{++} denotes the number of times a coincidence detection with outcome ++ in the bases i and j, respectively, occurred during a fixed time period, etc. Assuming a local variable model, S has an upper bound of two. Quantum mechanics, however, predicts that entangled qubits with entanglement visibility $V > 71\%$ can violate this bound: $S_{QM} = 2\sqrt{2}V$. This value is obtained when Alice's and Bob's basis are symmetrically positioned on a great circle around the Bloch sphere as shown in Fig. 3.5. A violation of the CHSH-Bell inequality is obtained for $S > 2$.

The four configurations used are depicted in Fig. 3.5. Alice's (Bob's) measurement bases are shown as black solid circles (white circles) on the Bloch sphere. Previous experiments with time-bin entangled qubits always reported a violation of the CHSH inequality using configuration 1, as in [34]. Configurations 2, 3 and 4 constitute a demonstration of nonlocality with time-bin entangled qubits measured in bases that do not lie exclusively on the equator. Configuration 4 corresponds to configuration 2 after a rotation of $-\pi/8$ around the y-axis, followed by a rotation of $-\pi/4$ around the x-axis.

In order to perform the measurements, one could set the phase of each UTBA individually

using a frequency stabilized reference laser. However, this is not required as one can set the phase of Bob's UTBA using the results from coincidence measurements. To see this, let us consider the quantum state in the middle time slot shared by Alice and Bob right after PBS2 and PBS5 of Alice's and Bob's UTBA (see Fig. 3.2-b). This state can be written as $|\psi'\rangle = \frac{1}{\sqrt{2}}(|HH\rangle + \mathrm{e}^{i(\phi_A+\phi_B)}|VV\rangle)$, where ϕ_A and ϕ_B are the relative phases picked up in the two interferometers. We see immediately that setting ϕ_B to $-\phi_A$ yields the desired state $|\psi\rangle$ of Eq. (3.2). Accordingly, we varied ϕ_B using the piezo actuator until we obtained a value of E_{11} that was consistent with the S-parameter expected from the measurements of the entanglement visibilities reported above. Then, we proceeded with the measurements of the remaining correlation coefficients.

Taking into account the measured entanglement visibilities, we expected values of S between 2.57 and 2.70 with Bob beside Alice, and between 2.40 and 2.49 with Bob at SAIT. As shown in Table 3.1, the measured values are in very good agreement with the predictions. Note that the violations (in terms of the number of standard deviations) are limited by the measurement time, which was set to 10 minutes or less to ensure stability of the system.

3.4 Conclusion and Discussion

The results presented here show that entanglement is a concept that is independent of the encoding used, and that it persists when different encodings are converted into each other. This work also opens new possibilities for using time-bin entanglement to perform more stringent test of nonlocality, and to implement new quantum communication protocols that require measurement bases exploring all dimensions of the Bloch sphere.

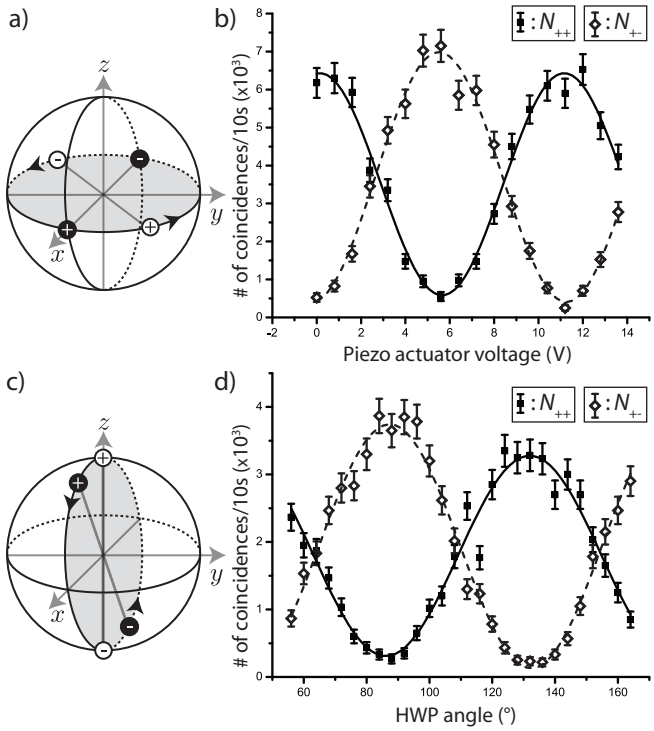

Figure 3.4: Entanglement visibility measurements. a) Bloch sphere depicting Alice's projection measurements (black solid circles with + and − symbols defining Alice's measurement basis) and Bob's measurements (white circles with + and − symbols defining Bob's measurement basis). Bob's measurements are scanned around the equator. b) Subset of the entanglement visibility curves with the settings of a) and with Bob at SAIT. The y-axis shows the number of coincidence detections, N_{++} and N_{+-}, per 10 seconds, where N_{++} corresponds to coincidences projecting on the state identified by the + black solid circle at Alice and on the + white circle at Bob's, etc. N_{-+} and N_{--} are similar (not shown). c) Bloch sphere showing Alice's measurement settings (black solid circles) and Bob's measurements (white circles). Alice's measurements are scanned around a great circle orthogonal to the equator. d) Subset of the entanglement visibility curves with the settings of c) and with Bob at SAIT.

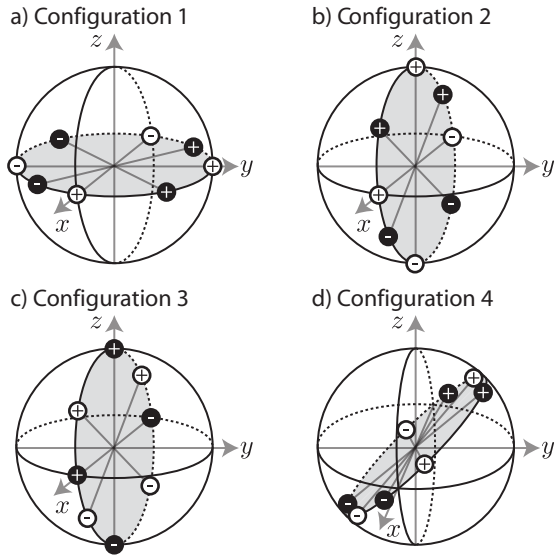

Figure 3.5: The four configurations used to violate the CHSH inequality. Alice's (Bob's) bases are represented by black solid circles (white circles).

Bibliography

[1] H.-K. Lo, M. Curty, B. Qi, Phys. Rev. Lett. 108, 130503 (2012)

[2] F. Xu, B. Qi, Z. Liao, H.-K. Lo, Appl. Phys. Lett. 103, 061101 (2013)

[3] A. Acin, N. Brunner, N. Gisin, S. Massar, S. Pironio, V. Scarani, Phys. Rev. Lett. 98, 230501 (2007)

[4] C. H. Bennett, G. Brassard, C. Crepeau, R. Jozsa, A. Peres, and W. K. Wootters, Phys. Rev. Lett. 70, 1895 (1993)

[5] S. Pironio, A. Acin, S. Massar, A. Boyer de la Giroday, D. N. Matsukevich, P. Maunz, S. Olmschenk, D. Hayes, L. Luo, T. A. Manning, C. Monroe, Nature 464, 1021 (2010)

[6] R.Gallego, N. Brunner, C. Hadley, and A. Acin, Phys. Rev. Lett. 105, 230501 (2010)

[7] M. Hendrych, R. Gallego, M. Miuda, N. Brunner, A. Acin, J. P. Torres, Nature Physics 8, 588 (2012)

[8] J. Ahrens, P. Badziag, A. Cabello, M. Bourennane, Nature Physics 8, 592 (2012)

[9] H. J. Kimble, Nature **453**, 1023 (2008).

[10] J. S. Bell, Physics **1**, 195 (1964).

[11] W. Tittel, and G. Weihs, Quantum Inf. and Computation **1**, 3 (2001).

[12] R. Thew, and N. Gisin, Nature Photonics **1**, 165 (2007).

[13] A. I. Lvovsky, B. C. Sanders, and W. Tittel, Nature Photonics **3**, 706 (2009).

[14] M. Żukowski, A. Zeilinger, M. A. Horne, and A. K. Ekert, Phys. Rev. Lett. **71**, 4287 (1993).

[15] H.-J. Briegel, W. Dür, J. I. Cirac, and P. Zoller, Phys. Rev. Lett. **81**, 5932 (1998).

[16] N. Sangouard, C. Simon, H. de Riedmatten, and N. Gisin, arXiv:0906.2699 (2009).

[17] M. Żukowski, and A. Zeilinger, Phys. Lett. A **155**, 69 (1991).

[18] X.-s. Ma, A. Qarry, J. Kofler, T. Jennewein, and A. Zeilinger, Phys. Rev. A **79** 042101 (2009).

[19] L. Neves, G. Lima, J. Aguirre, F. A. Torres-Ruiz, C. Saavedra, and A. Delgado, New J. of Phys. 11 073035 (2009).

[20] L. Neves, G. Lima, A. Delgado, and C. Saavedra, Phys. Rev. A 80 042322 (2009)

[21] G. Vallone, E. Pomarico, P. Mataloni, F. De Martini, and V. Berardi, Phys. Rev. Lett. **98**, 180502 (2007).

[22] K. Chen, C.-M. Li, Q. Zhang, Y.-A. Chen, A. Goebel, S. Chen, A. Mair, and J.-W. Pan, Phys. Rev. Lett. **99**, 120503 (2007).

[23] R. Ursin *et al.*, Nature Physics **3**, 481 (2007).

[24] I. Marcikic, H. de Riedmatten, W. Tittel, H. Zbinden, M. Legré, and N. Gisin, Phys. Rev. Lett. **93**, 180502 (2004).

[25] M. Fujiwara, M. Toyoshima, M. Sasaki, K. Yoshino, Y. Nambu, and A. Tomita, quant-ph/1002.4226.

[26] F. Bussières, Y. Soudagar, G. Berlín, S. Lacroix, and N. Godbout, arXiv:quant-ph/0608183 (2006).

[27] J. F. Clauser, M. A. Horne, A. Shimony, and R. A. Holt, Phys. Rev. Lett. **23**, 880 (1969).

[28] G. Berlín, G. Brassard, F. Bussières, and N. Godbout, Phys. Rev. A **80**, 062321 (2009).

[29] G. Berlín, G. Brassard, F. Bussières, N. Godbout, J. A. Slater, and W. Tittel, arXiv:0904.3946 (2009).

[30] A. J. Leggett, Found. Phys. **33**, 1469 (2003).

[31] S. Gröblacher, T. Paterek, R. Kaltenbaek, Č. Brukner, M. Żukowski, M. Aspelmeyer, and A. Zeilinger, Nature **446**, 871 (2007); T. Paterek, A. Fedrizzi, S. Gröblacher, T. Jennewein, M. Żukowski, M. Aspelmeyer, and A. Zeilinger, Phys. Rev. Lett. **99**, 210406 (2007).

[32] C. Branciard, A. Ling, N. Gisin, C. Kurtsiefer, A. Lamas-Linares, and V. Scarani, Phys. Rev. Lett. **99**, 210407 (2007); C. Branciard, N. Brunner, N. Gisin, C. Kurtsiefer, A. Lamas-Linares, A. Ling, V. Scarani, Nature Phys. **4**, 681 (2008).

[33] J. Brendel, N. Gisin, W. Tittel, and H. Zbinden, Phys. Rev. Lett. 82, 2594 (1999).

[34] W. Tittel, J. Brendel, H. Zbinden, and N. Gisin, Phys. Rev. Lett. **84**, 4737 (2000).

[35] H. C. Lefèvre, Electron. Lett. **16** (1980).

[36] I. Lucio Martinez, P. Chan, X. F. Mo, S. Hosier, and W. Tittel, New Journal of Physics **11**, 095001 (2009).

[37] P. Pearle, Phys. Rev. D **2**, 1418 (1970).

[38] P. H. Eberhard, Phys. Rev. A **47**, R747 (1993).

Chapter 4

Entanglement Swapping with Quantum-Memory Compatible Photons

Entanglement swapping entangles two photons that have no common past [1]. Projecting two independent photons, each from an individual entangled photon pair, onto a maximally entangled state generates entanglement between the other two photons. For instance, the tensor product of two individual entangled states, e.g. $|\Phi^+\rangle_{AB} \otimes |\Phi^-\rangle_{CD}$, can be represented in Bell basis for states B and C as :

$$\frac{1}{2}(|\Phi^+\rangle_{BC} \otimes |\Phi^-\rangle_{AD} - |\Phi^-\rangle_{BC} \otimes |\Phi^+\rangle_{AD} - |\Psi^+\rangle_{BC} \otimes |\Psi^-\rangle_{AD} + |\Psi^-\rangle_{BC} \otimes |\Psi^+\rangle_{AD}) \quad (4.1)$$

This shows that if the two photons (B, C) are projected on the Bell basis, then the other two photons (A, D) are maximally entangled as shown in Equation 4.1, that is, entanglement is swapped between the photons. In other words, as shown in Figure 4.1, a Bell-state measurement heralds entanglement and thus entanglement swapping is one way to make entanglement in a heralded fashion. Moreover, in the context of a quantum repeater, the swapped entanglement has to entangle separate quantum memories in order to establishing the elementary link of the repeater. This means that photons must be compatible with quantum memories in the sense that all photonic degrees of freedom of the photons need to be properly engineered to match the memory's specifications.The first experimental demonstration of entanglement swapping with free-space optics was reported in 1998 [2] and in 2002 the nonlocal property of swapped entanglement was revealed [3]. An optical fibre-based experiment of entanglement swapping with telecommunication-wavelength photons was im-

plemented in 2005 [4].

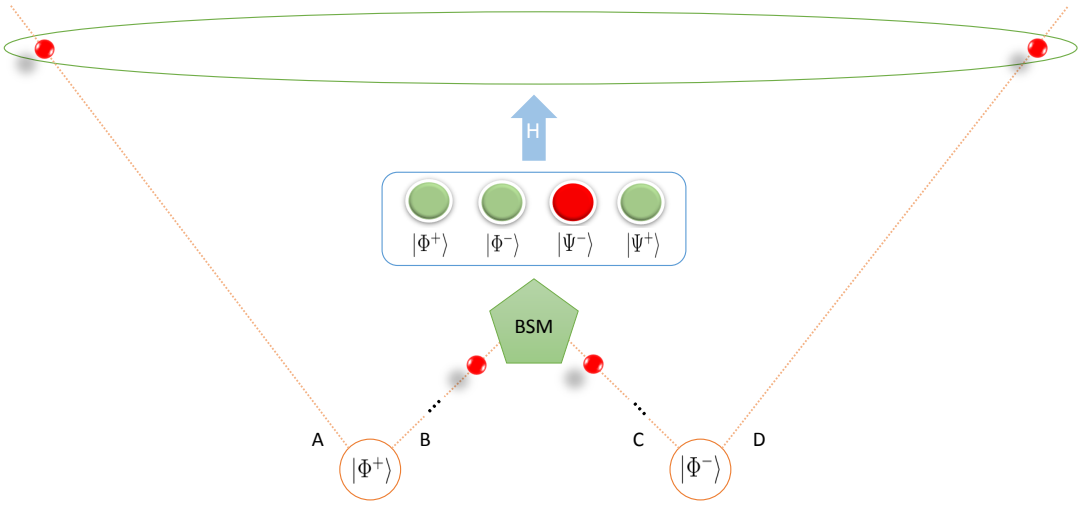

Figure 4.1: **A schematic diagram of entanglement swapping.** A Bell-state measurement (BSM) on photons (B,C) heralds entanglement between photons A and D. H stands for a heralding signal.

This Chapter demonstrates the experimental generation of heralded entanglement with quantum-memory compatible photons via entanglement swapping, as required for an elementary repeater link. Photons are spectrally filtered down to the order of Ghz, which matches the bandwidth of our quantum memories, and are coupled into sinlge-mode optical fibres to guarantee spatial-mode matching. A picture of experimental setup is shown in Figure 4.2.

In this Chapter, the experiment was conducted in collarboration with Marcel.li G. Puigibert, Lambert Giner, Joshua A. Slater, Michael R. E. Lamont, and Daniel Oblak. The superconducting nanowire single-photon detectors used in the experiment were developed by Varun B. Verma, Matthew D. Shaw, Francesco Marsili, and Sae Woo Nam. Wolfgang Tittel conceived

and directed the experiment. I contributed to this study in the following stages : building the sources of entanglement and measurement setups, performing the measurements, ,analyzing the results, and writing the manuscript.

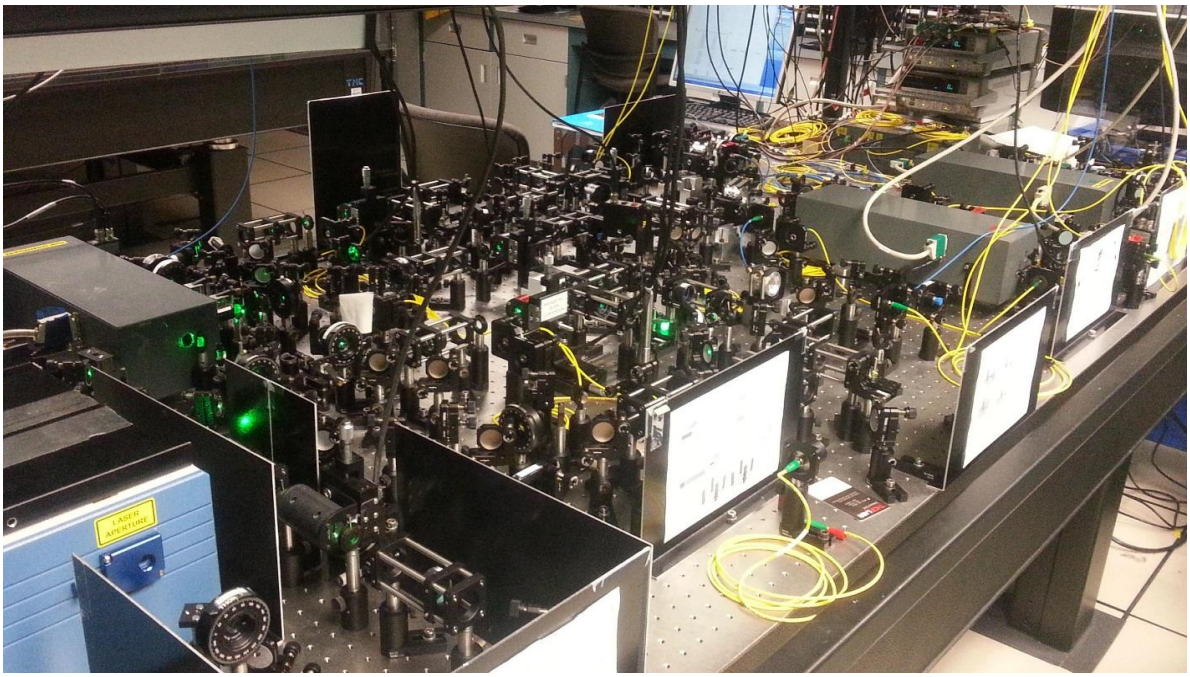

Figure 4.2: **Picture of the experimental setup for entanglement swapping.**

J. Jin[1], M. Grimau Puigibert[1], L. Giner[1],J. A. Slater[1], M. R. E. Lamont[1],V. B. Verma[2], M. B. Shaw[3], F. Marsili[3], S. W. Nam[2], D. Oblak[1], and W. Tittel[1]

[1]*Institute for Quantum Information Science, and Department of Physics and Astronomy, University of Calgary, 2500 University Drive NW, Calgary, Alberta T2N 1N4, Canada*

[2]*National Institute of Standards and Technology, Boulder, Colorado 80305 USA*

[3] *Jet Propulsion Laboratory, California Institute of Technology, 4800 Oak Grove Drive, Pasadena, California 91109, USA*

Abstract

We report entanglement swapping with time-bin entangled photon pairs, each constituted of one 795 nm photon and a 1532 nm photon, and created via spontaneous parametric down conversion in a non-linear crystal. After projecting the two 1532 nm photons onto a Bell state, entanglement between the two 795 nm photons is verified by means of quantum state tomography. As an important feature, the bandwidth of these photons is compatible with Tm:$LiNbO_3$- based quantum memories, making our experiment an important step towards the realization of a quantum repeater.

4.1 Introduction

Entanglement swapping entangles two photons that have no common past [1]. This fascinating phenomenon not only stimulated curiosity to understand quantum correlations [5, 6, 7, 8, 9, 10], but also plays an important role in various applications of quantum information science, including quantum computing [11, 12] and quantum repeaters [13]. A quantum repeater-based communication channel, for instance, use entanglement swapping to entangle interim nodes in a heralded fashion, and connect elementary entangled links (connecting interim nodes) to distribute entanglement over arbitrarily long distance [14, 15]. In turn, the resulting entanglement can be used to generate a secret key between distant users [16].

A necessary ingredient for quantum repeaters, in addition to entanglement swapping, are optical quantum memories [17]. Such memories allow the reversible mapping of (entangled) states between light and atoms, and thereby remove the necessity for all elementary links to

establish entanglement in a synchronized fashion. While entanglement swapping has been reported before [2, 3, 4, 18, 19, 20], the spectra of the resulting entangled photons were either orders of magnitude too large, or their wavelength were not suitable to allow subsequent interfacing with optical quantum memory. Here we remove this impediment.

4.2 Experiment

A schematics of our experimental setup is depicted in Fig. 4.3. A 1047 nm wavelength laser emits 6 ps long pulses at 80 MHz repetition rate. After second harmonic generation (SHG) in a periodically poled lithium niobate crystal (PPLN), the then 18 ps long pulses, centered at 523.5 nm wavelength, travel through an unbalanced Mach-Zehnder interferometer whose path length difference corresponds to 1.4 ns travel time difference, thereby splitting every pulse into two. Pairs of pulses emitted from the two outputs of the interferometer then pump two 10 mm-long PPLN crystals, in which spontaneous parametric down-conversion (SPDC) leads to time-bin entangled qubits [21] with photons centred at wavelengths around 795 nm and 1532 nm. Assuming, for the sake of explanation, for the moment that only individual pairs are emitted, this leads to states of the form $|\phi^+\rangle_{AB} = \frac{1}{\sqrt{2}}(|e\rangle_A |e\rangle_B + |\ell\rangle_A |\ell\rangle_B)$ emitted from one crystal, and $|\phi^-\rangle_{CD} = \frac{1}{\sqrt{2}}(|e\rangle_C |e\rangle_D - |\ell\rangle_C |\ell\rangle_D)$ emitted from the other crystal, where $|e\rangle$ and $|\ell\rangle$ represent *early* and *late* time-bin qubit states.

Using a grating monochromator connected to a single photon detector, we measure the spectral width of the 795 nm photon at full width half maximum (FWHM) to be 1.5 nm. By energy conservation, and taking into account the bandwidth of the pump photons, we calculate the spectral width of the 1532 nm photons to be 5.6 nm (FWHM). These values by far exceed the maximum bandwidth of 10 GHz (corresponding to 21 pm at 795 nm wavelength), over which quantum memories have so far been reported to operate [22]. Hence, to allow

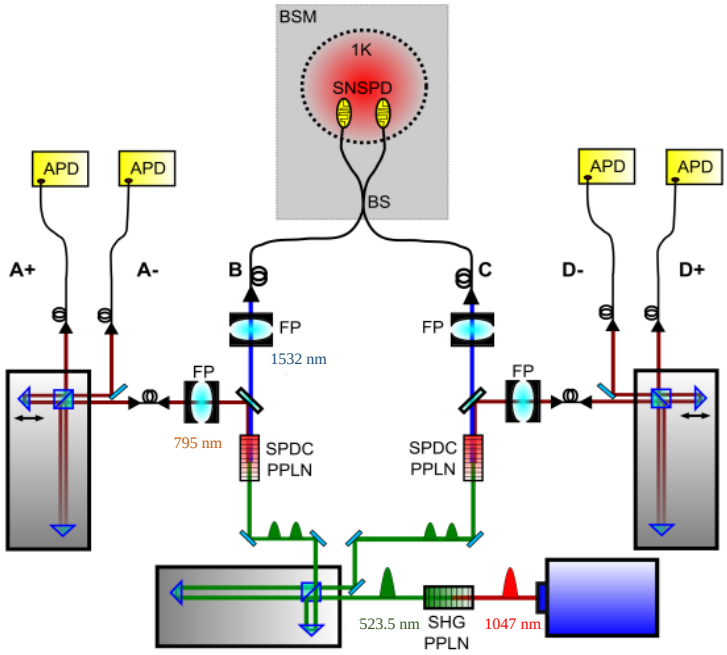

Figure 4.3: **Schematics of our setup. See text for details.**

future interfacing with memories, we filter the 795 nm photons using Farbry-Perot cavities (FP; one per source) to 6 GHz, and also reduce the bandwidth of the 1532 nm photons to 12 GHz (again using Fabry-Perot cavities), which corresponds to 94 pm. This additionally ensures that the photons' coherence time, around 37 ps, exceeds that of the pump pulses, as required for entanglement swapping. Using the approach described in [23], we find the probability of having a photon pair per source and laser pulse after filtering to be about 7%.

To swap entanglement to the two 795 nm qubits (A,D), the two 1532 nm qubits (B,C), after having travelled through short standard telecommunication fibre, are subjected to a so-called Bell-state measurement (BSM). This measurement is performed by sending the two photons into the different input ports of a 50/50 beam splitter. Provided they exit through two different output ports and in different temporal modes – one photon early, the other one late –, their joint state is projected onto the $|\psi^-\rangle = \frac{1}{\sqrt{2}}\left(|e\rangle_B |\ell\rangle_C - |\ell\rangle_B |e\rangle_C\right)$ Bell state,

leaving the two 795 nm photons in an entangled $|\psi^+\rangle = \frac{1}{\sqrt{2}}\left(|e\rangle_A|\ell\rangle_D + |\ell\rangle_A|e\rangle_D\right)$ Bell state. We note that, in principle, it is also possible to make projection measurements onto the $|\psi^+\rangle$ Bell state, thereby increasing the measurement's efficiency from maximally 25% to 50% [24].

For the Bell-state measurement to work, the two photons must be indistinguishable at the beam splitter, i.e, their spatial, temporal, spectral, and polarization modes must be identical. This is verified using so-called Hong-Ou-Mandel interference [25]: if two indistinguishable photons (not qubits) impinge on a symmetric beam splitter from different input ports, then they bunch and leave together by the same output port due to destructive interference between the probability amplitudes associated with both input photons being transmitted or both reflected. Conversely, if the two photons are distinguishable, no such interference occurs, and they leave the beamsplitter with 50% probability through different outputs, resulting in coincident detections. The HOM visibility, defined as $V_{HOM} = (N_{max} - N_{min})/N_{max}$ [26], where N_{max} and N_{min} denote coincidence count rates measured with completely distinguishable and (maximally) indistinguishable photons, respectively, is a common way to characterize the degree of indistinguishability. We find $V_{HOM} = 27.5 \pm 2.5\%$ as shown in Fig. 2. This value is consistent with the fact that our 1532 nm inputs are not single photons, but are mixtures of photon Fock states with thermal distribution, for which the HOM visibility is upper bounded by 1/3 [26]. Repeating the measurement conditioned on the detection of two 795 nm photons, which projects the 1532 nm inputs onto approximate single photons, the HOM visibility increases to $87.5 \pm 5.5\%$. The gap to the theoretical value of 100% is due to insufficient spectral filtering of the photons. Indeed, using $V_{HOM}^{Max} = 1/\sqrt{1 + (\frac{\Delta T}{\tau})^2}$ [27, 28], where ΔT denotes the duration of the pump pulses, and τ the coherence time of the 1532 nm photons after filtering, we find that the maximum visibility achievable with our setup is 89%, which corresponds to our result with experimental error.

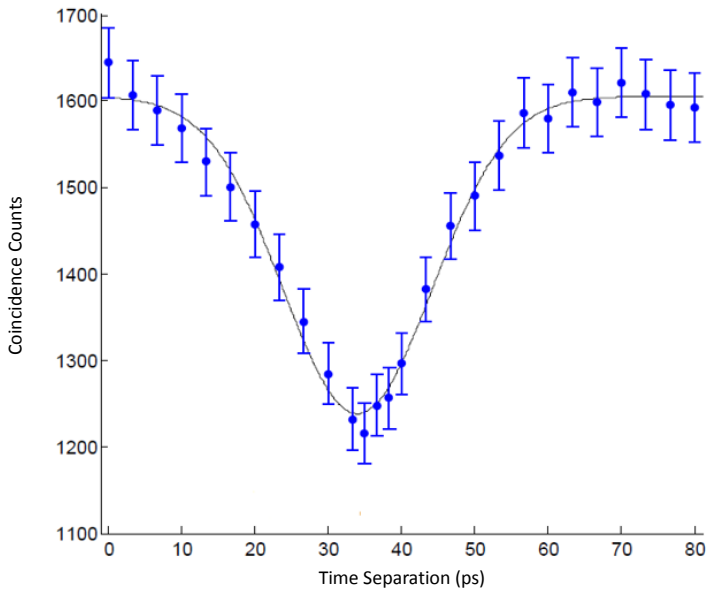

Figure 4.4: **Coincidence count rate of the 1532 photons (B,C) as a function of the delay of one photon.**

To detect the 1532 nm photons, we use free-running, tungsten silicide (WSi)-based superconducting nanowire single-photon detector (SNSPD) cooled to around 0.9 Kelvin, whose detection efficiency has been reported to exceed 90% [29]. Due to fibre transmission loss inside our cryostat, we find a system efficiency of around 50%. Furthermore, we measure a detection-time jitter of 250 ps (FWHM), which is sufficiently small to allow resolving the temporal qubit modes (spaced by 1.4 ns), and the dark-count rate of 10 Hz ensures little pollution of detection signals through noise.

The two 795 nm photons are sent through Mach-Zehnder interferometers that introduce the same travel-time difference of 1.4 ns as the interferometer that acts on the pump beam and allow projecting photon states onto various qubits states [21]. To ensure phase stability during the measurements, i.e. constant projectors, the interferometers are passively temperature stabilized. Additionally, their phases are actively locked using a frequency-stabilized laser at 1550 nm wavelength that is also sent through the interferometers, and a home-

made feedback loop. Finally, the 795 nm photons are detected using four standard silicon avalanche photodiode-based single photon detectors with efficiencies around 50% and dark counts around a few hundred Hz. All detection signals are recorded using a time-to-digital convertor that is started by a successful BSM.

4.3 Measurements and Results

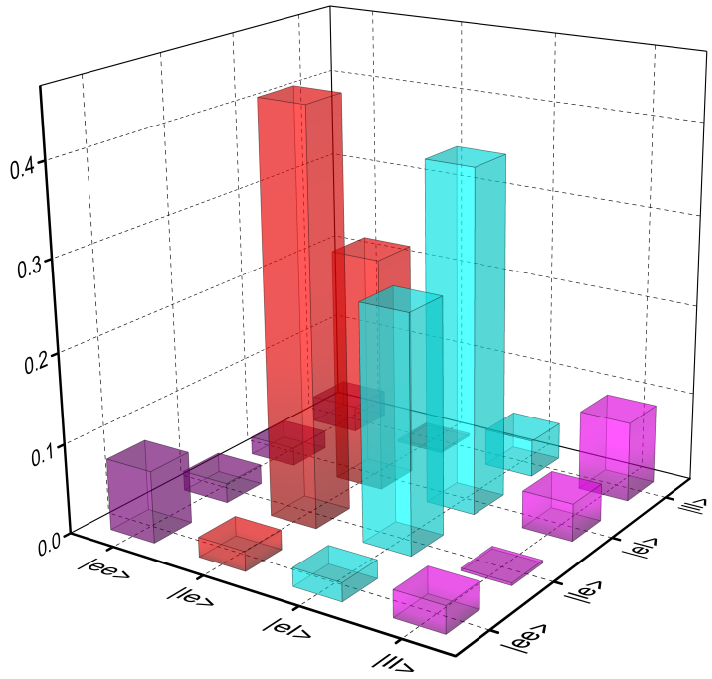

Figure 4.5: **Density matrix characterizing the joint state of the two 795 nm photons after entanglement swapping.**

To verify the presence of entanglement between the two 795 nm photons after the BSM with the 1532 nm photons, we perform various projection measurements that allow reconstructing the 795 nm photons joint quantum state by means of quantum state tomography [30]. Fig. 4.5 shows the resulting density matrix, which was obtained after 36 hours of

measurement. It allows predicting measurement outcomes and, most importantly, enables calculating measures for entanglement. For instance, we find the concurrence (a commonly used entanglement witness [31]) to be 0.36 ± 0.06. It is slightly above zero, indicating entanglement, but the uncertainty, derived from Monte-Carlo simulation, is currently too large to make this value significantly larger than zero. To improve both the mean value as well as the uncertainty, we have to decrease the probability of generating a photon pair per pulse below our current value of 9%, thereby reducing the number of (undesired) multiple pairs that is also emitted by each source. However, this will further increase the measurement time, making this measurement with the current setup very challenging. It is thus necessary to decrease the loss of photons between the photon pair sources and the detectors, e.g. by reducing aberrations encountered during (off-axis) transmission through lenses, using mirrors with higher reflectivity, or changing focussing parameters [32]. This work is in progress, and we expect repeating the measurement with reduced mean photon-pair numbers and improved results in near future.

4.4 Conclusion and Discussion

We have experimentally investigated the possibility to entangle two 795 nm photons, whose properties are suitable for further storage in broadband quantum memories such as our $LiNbO_3$ waveguides, by means of a Bell state measurement with two 1532 nm photons, each of which was initially entangled with one of the two 795 nm photons. While the resulting entanglement is not yet significant, our demonstration constitutes an important step towards the generation of a quantum repeater: the herald entanglement of two quantum memory-compatible photons. Further improvements have been suggested, and additional work is in progress.

Bibliography

[1] M. Zukowski, A. Zeilinger, M. A. Horne, and A. K. Ekert, Phys. Rev. Lett. 71, 4287 (1993).

[2] J. W. Pan, D. Bouwmeester, H. Weinfurter and A. Zeilinger, Phys. Rev. Lett. 80, 3891 (1998)

[3] T. Jennewein, G. Weihs, J. -W. Pan, A. Zeilinger, Phys. Rev. Lett. 88, 017903 (2002)

[4] H. de Riedmatten, I. Marcikic, J.A.W. van Houwelingen, W. Tittel, H. Zbinden, N. Gisin, Phys. Rev. A 71, 050302 (2005)

[5] E. Megidish, A. Halevy, T. Shacham, T. Dvir, L. Dovrat, and H. S. Eisenberg, Phys. Rev. Lett. 110, 210403 (2013).

[6] X. -S. Ma, S. Zotter, J. Kofler, R. Ursin, T. Jennewein, . Brukner, A. Zeilinger, Nature Physics 8, 480 (2012).

[7] A. J. Short, S. Popescu, and N. Gisin, Phys. Rev. A 73, 012101 (2006).

[8] C. Branciard, D. Rosset, N. Gisin, S. Pironio, Phys. Rev. A 85, 032119 (2012).

[9] W. Kobus, W. Laskowski, M. Markiewicz, A. Grudka, Phys. Rev. A 86, 020302 (2012).

[10] S. Bose, V. Vedral. and P. L. Knight, Phys. Rev. A 57, 822 (1998).

[11] Ladd, T. D. et al. Quantum computers. Nature 464, 45-53 (2010).

[12] E. Knill, R.Laflamme and G. Milburn, Nature 409, 46-52 (2001).

[13] H. -J. Briegel, W. Dür, J. I. Cirac, and P. Zoller, Phys. Rev. Lett. 81, 5932 (1998).

[14] N. Sangouard, C. Simon, H. de Riedmatten, and N. Gisin, Rev. Mod. Phys. 83, 33 (2011).

[15] N. Sinclair, E. Saglamyurek, H. Mallahzadeh, J. A. Slater, M. George, R. Ricken, M. P. Hedges, D. Oblak, C. Simon, W. Sohler, and W. Tittel, accepted for publication in Phys. Rev. Lett. (Preprint arXiv:1309.3202 [quant-ph]).

[16] A. K. Ekert, Phys. Rev. Lett. 67, 661 (1991).

[17] A. I. Lvovsky, B. C. Sanders, and W. Tittel, Nature Photon. 3, 706-714 (2009).

[18] M. Halder, A. Beveratos, N. Gisin, V. Scarani, C. Simon, and H. Zbinden, Nature Physics 3, 692-695 (2007).

[19] Z.-S. Yuan, Y. -A. Chen, B. Zhao, S. Chen, J. Schmiedmayer, J. -W. Pan, Nature 454, 1098-1101 (2008).

[20] R. Kaltenbaek, R. Prevedel, M. Aspelmeyer, A. Zeilinger, Phys. Rev. A 79, 040302 (2009).

[21] W. Tittel, G. Weihs, Quantum Information and Computation 1, Rinton Press (2001).

[22] E. Saglamyurek, N. Sinclair, J. Jin, J. A. Slater, D. Oblak, F. Bussiières, M. George, R. Ricken, W. Sohler, and W. Tittel, Nature 469, 512 (2011).

[23] I. Marcikic, H. de Riedmatten, W. Tittel, V. Scarani, H. Zbinden, and N. Gisin, Phys. Rev. A 66 062308 (2002).

[24] R. Valivarthi, I. Lucio-Martinez, A. Rubenok, P. Chan, F. Marsili, V. B. Verma, M. D. Shaw, J. A. Stern, J. A. Slater, D. Oblak, S. W. Nam, W. Tittel (submitted).

[25] C. K. Hong, Z. Y. Ou, and L. Mandel, Phys. Rev. Lett. 59, 2044 (1987).

[26] H. de Riedmatten, I. Marcikic, W. Tittel, H. Zbinden, N. Gisin, Phys. Rev. A 67, 022301 (2003).

[27] M. Zukowski, A. Zeilinger, and H. Weinfurter, Annals of the New York Academy of Sciences 755, 91 (1995).

[28] J. G. Rarity, Annals of the New York Academy of Sciences 755, 624 (1995).

[29] F. Marsili, V. B. Verma, J. A. Stern, S. Harrington, A. E. Lita, T. Gerrits, I. Vayshenker, B. Baek, M. D. Shaw, R. P. Mirin, S. W. Nam, Nature Photon. 7, 210-214 (2013).

[30] J. B. Altepeter, E. R. Jeffrey, and P. G. Kwiat, Adv. At. Mol. Opt. Phys. 52, 105 (2005).

[31] W. K. Wootters, Phys. Rev. Lett. 80, 2245 (1998).

[32] T. Guerreiro, A. Martin, B. Sanguinetti, N. Bruno, H. Zbinden, R. T. Thew, arXiv:1309.2457 [quant-ph].

Chapter 5

Storage of Quantum Bits

As a classical memory stores classical bits, a quantum memory is capable of preserving quantum properties, i.e. quantum information in terms of qubit states or entanglement, as well as wavefuntion. These fundamental functionalities not only differenciate a quantum memory from any classical storage device but also allow embedding it into a quantum repeater. The first quantum memory was realized in 2004 using a gas-state atomic ensemble [1]. A solid-state memory at a single-photon level has been reported 4 years later [2].

This Chapter demostrates a mapping of quantum bits into and out of a solid-state based quantum memory. Externally provided photonic time-bin qubits are stored in our storage material, a thulium-doped $LiNbO_3$ waveguide, cooled to 3 Kelvin and retrieved after 6 nanoseconds. An average fidelity between input and output states is investigated by performing projection measurements in order to verify the faithful storage in the quantum memory. The obtained value of 0.885 ± 0.020 exceeds not only the maximal achievable fidelity (2/3) using the best classical storage strategy for discrete values [3] but also the 5/6-limit that can be obtained by the best known optimal quantum cloning device [4]. This confirms that our memory is capable of preserving quantum bits during storage, thus entitling it to be called *quantum memory* and making it suitable for quantum science technologies including quantum repeaters.

In this Chapter, the experiment was conducted in collaboration with Erhan Saglamyurek, Neil Sinclair, Joshua A. Slater, Daniel Oblak, Félix Bussières. The thulium-doped $LiNbO_3$ waveguide was fabricated and charaterized by Mathew George, Raimund Ricken, and Wolf-

gang Sohler at room temperature. Wolfgang Tittel conceived and directed the expeirment. I contributed to this study in the following stages : building photonic time-bin qubits and measurement setups, as well as performing the measurements.

Physical Review Letters, 108, 083602 (2012)

Conditional Detection of Pure Quantum States of Light after Storage in a Tm-Doped Waveguide

Erhan Saglamyurek[1], Neil Sinclair[1], Jeongwan Jin[1], Joshua A. Slater[1], Daniel Oblak[1], Félix Bussières[1], Mathew George[2], Raimund Ricken[2], Wolfgang Sohler[2], and Wolfgang Tittel[1]

[1]*Institute for Quantum Information Science, and Department of Physics and Astronomy, University of Calgary, 2500 University Drive NW, Calgary, Alberta T2N 1N4, Canada*

[2]*Department of Physics - Applied Physics, University of Paderborn, Warburger Str. 100, 33095 Paderborn, Ge rmany*

Abstract

We demonstrate the conditional detection of time-bin qubits after storage in and retrieval from a photon-echo based waveguide quantum memory. Each qubit is encoded into one member of a photon-pair produced via spontaneous parametric down conversion, and the conditioning is achieved by the detection of the other member of the pair. By performing projection measurements with the stored and retrieved photons onto different bases, we obtain an average storage fidelity of 0.885 ± 0.020, which exceeds the relevant classical bounds and shows the suitability of our integrated light-matter interface for future applications of quantum information processing.

5.1 Introduction

Quantum memories are key elements for future applications of quantum information science such as long-distance quantum communication via quantum repeaters [5, 6] and, more generally, distributed quantum information processing in quantum networks [7]. They enable reversible mapping of arbitrary quantum states between travelling and stationary carriers (i.e. light and matter). This reduces the impact of loss on the time required to establish entanglement between distant locations [5], and allows the implementation of local quantum computers based on linear optics [8]. However, towards these ends, the successful transfer of a quantum state into the memory must be announced by a heralding signal. When using an individual absorber, such a signal can be derived through the detection of a change of atomic level population [9]. In atomic ensembles, this approach is infeasible. Instead, storage is derived from the detection of a second photon that indicates either the absorption [10], or the presence of the first at the input of the memory [11] (the first approach relies on spontaneous Raman scattering, the second on using pairs of photons). Furthermore, quantum memories must have large acceptance bandwidths and multi-mode capacities, and allow on-demand read-out after second-long storage with high efficiency [11, 12]. In addition, for viable quantum technology, quantum memories should be robust and simple to operate (e.g. be based on integrated optics).

A lot of progress towards these figures of merit has been reported over the past few years, including work that explores electromagnetically induced transparency (EIT), as well as photon-echo and cavity QED-based approaches (see [6, 9, 11, 12, 13, 14, 15, 16, 17, 18, 19, 20] for reviews and latest achievements). For instance, quantum memories employing Rb vapour have demonstrated efficiencies up to 87% [13] and storage times in excess of 0.1 s [14], while GHz bandwidths [15] and storage of 64 modes [18] have been shown in rare-earth materials. However, having a quantum memory that simultaneously satisfies all figures of merit cur-

rently remains an outstanding challenge.

Yet, strictly, most of these experiments did not report true heralding – either heralding was not actually implemented, the "heralding" signal was generated only after the stored photon left the memory, or the signal could, due to technical issues, only be derived once the stored photon was detected. Nevertheless, experiments that employ photon pairs [15, 16, 17, 21] do gain from conditioning the detection of the stored photon on that of the auxiliary photon (i.e. *a posteriori* "heralding"): By reducing the effects of loss and detector noise, conditioning generally increases the fidelity between the quantum state of the original and the retrieved photon.

Supplementing the experiments on storage of entangled photons [15, 16, 17, 21], we now report another step towards the goal of building universal, viable, and heralded quantum memory devices – the storage of photons in pure quantum states in a solid state waveguide, their retrieval, and their conditional detection by means of temporal correlations with auxiliary photons. We point out that the step to true heralding is minor and of purely technical nature; it simply requires using different, existing, single-photon detectors (see [22, 23]).

5.2 Experiment

Our experimental setup consists of two main blocks, see Fig. 5.1: a spontaneous parametric down-conversion (SPDC) photon-pair source, and a Ti:Tm:$LiNbO_3$ single mode waveguide fabricated by indiffusion processes [24]. When cooled to 3 K, and by using a photon-echo quantum memory protocol [8, 12, 25], the Tm-doped waveguide allows storage and retrieval of quantum states encoded into one member of each photon pair, while the detection of the other member provides the conditioning signal.

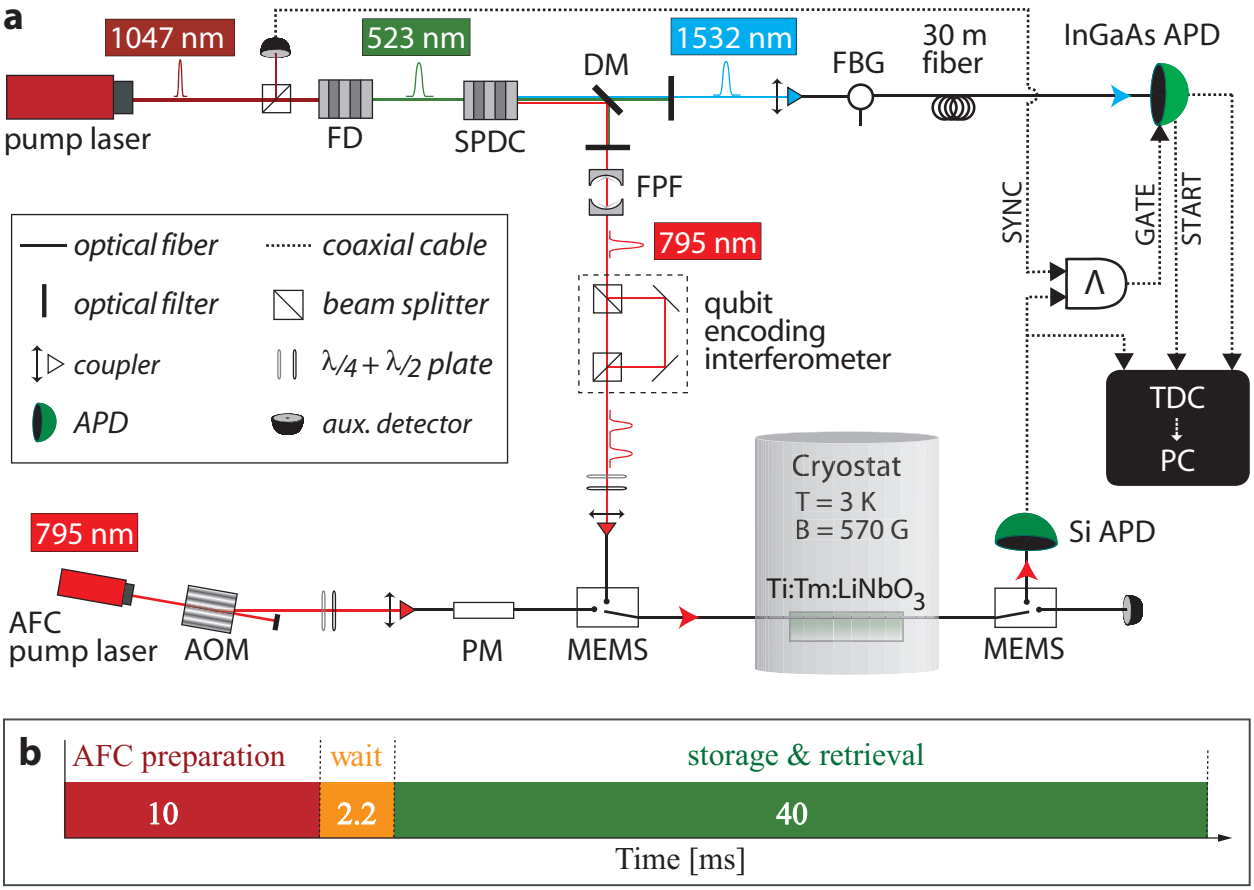

Figure 5.1: (color online) **a. Photon pair source and quantum memory setup (see text for details):** Wave-plates align light polarization along the $LiNbO_3$'s C_3-axis. The waveguide is held at 3 K, and a 570 G magnetic field is applied along the crystal's C_3-axis (see Fig. 5.1 2a). **b.** Timing sequence containing three repeated phases: 10 ms *AFC preparation* for optical pumping, 2.2 ms *wait* to allow excited population to decay, and 40 ms *storage and retrieval*, during which 795 nm photons are successively stored for $t_{st} = 6$ ns and then recalled.

In the photon-pair source a mode-locked pump laser generates 6 ps long pulses at a rate of 80 MHz and 1047.328 nm central wavelength. They are subsequently frequency-doubled (FD) in a periodically poled $LiNbO_3$ (PPLN) crystal, yielding pulses with 523.664 nm central wavelength, 16 ps duration, and 90 mW average power. The FD pulses are sent to a second PPLN crystal that, via SPDC, produces pairs of photons centred at 795.506 nm and

1532.426 nm. Frequency filtering the 795 nm photons with a 6 GHz-bandwidth Fabry-Perot filter (FPF) and the 1532 nm photons with a 9 GHz-bandwidth fiber-Bragg grating (FBG) we obtain frequency uncorrelated pairs. Each 795 nm photon travels through an imbalanced, temperature-stabilized Mach-Zehnder interferometer with 42 cm path-length difference, corresponding to 1.4 ns relative delay. Thus, each photon emerges in a superposition of two temporal modes (early and late), i.e., in a time-bin qubit state [26]. They are then directed into the quantum memory, stored, retrieved, and finally detected by a Si avalanche-photodiode (APD)-based single-photon detector.

All 1532 nm photons are sent through 30 m standard telecommunication fiber to an InGaAs APD-based single-photon detector. As is typically done, the detector is gated to reduce noise. The gate signal could in principle be the SYNC signal derived from each pulse emitted by the pump laser. However, as its repetition rate of 80 MHz by far exceeds the maximum gate frequency of our detector, around 1 MHz, we first AND the SYNC pulses with pulses generated by each Si-APD detection, and then use this low-rate signal to gate the InGaAs-APD. Provided the latter is ready for photon detection (i.e. not deadtime-blocked due to a previous detection), this signal also starts a time-to-digital converter (TDC), which then records the time-difference between the detection events produced by the Si-APD and the InGaAs-APD. These data are used to obtain statistics for single detections of the retrieved 795 nm photons, as well as for detections conditioned on the existence of 1532 nm photons. We emphasize that if an InGaAs APD supporting 80 MHz gate rate had been available [22, 23], then 1532 nm photons could have been detected without the need for *a priori* detection of a 795 nm photon. This simple modification of our setup would have turned the conditional detection of 795 nm photons into detections that are heralded by clicks of the InGaAs APD.

The other main block of our setup is a Ti:Tm:$LiNbO_3$ waveguide that allows storage and

retrieval of the 795 nm photons via the atomic frequency comb (AFC) quantum memory protocol [25]. This approach to quantum state storage requires the spectral absorption of an atomic ensemble to be constituted of a series of equally spaced lines with frequency spacing Δ_ν. The interaction between such an AFC and a photon with wavevector k leads to the absorption of the photon and generates a collective excitation in the atomic medium that is described by

$$|\Psi\rangle = \frac{1}{\sqrt{N}} \sum_{j=1}^{N} c_j e^{i2\pi m_j \Delta_\nu t} e^{-ikz_j} \, |g_1, \cdots e_j, \cdots g_N\rangle \, . \tag{5.1}$$

Here, $|g_j\rangle$ ($|e_j\rangle$) denotes the ground (excited) state of atom j, $m_j\Delta_\nu$ is the detuning of the atom's transition frequency from the photon carrier frequency, z_j its position measured along the propagation direction of the light, and the factor c_j depends on the atom's resonance frequency and position. Because of the presence of different atomic transition frequencies, the excited collective coherence dephases rapidly. However, the particular shape of the absorption line results in the recovery of the collective coherence after storage time $t_{st} = 1/\Delta_\nu$. This can easily be seen from Eq. (5.1): for $t = 1/\Delta_\nu$ all frequency dependent phase factors are zero (mod 2π). This leads to re-emission of the photon into the original mode and quantum state with maximally 54% efficiency for an optimally implemented AFC. Modifications to the procedure enable recall on demand and up to 100% efficiency [25].

Suitable media in which to implement the AFC protocol are cryogenically cooled rare-earth ion doped crystals [8, 27]. They feature inhomogeneously broadened absorption profiles, often posses long-lived atomic sub-levels that can serve as shelving levels for tailoring the AFC through persistent spectral hole burning, and generally have long coherence times on optical and spin transitions. We use the $^3H_6$-$^3H_4$ transition of Tm ions in a single-mode channel waveguide fabricated by Ti indiffusion into the Tm doped surface of a Z-cut $LiNbO_3$ crystal, see Fig. 5.2a [26]. To tailor the desired AFC into the inhomogeneously broadened absorption

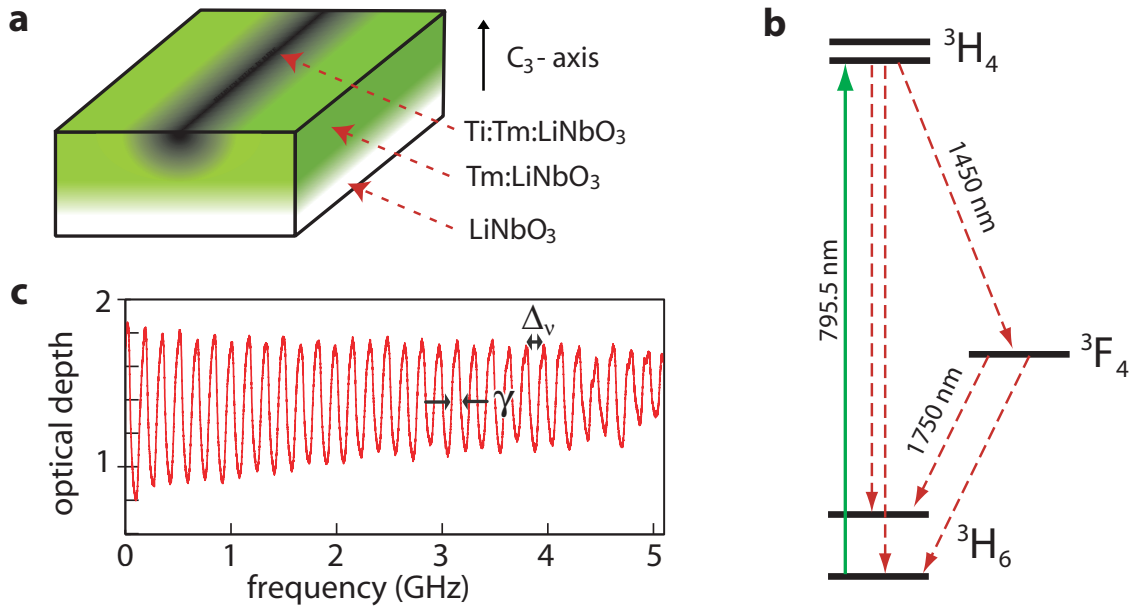

Figure 5.2: (color online) **a. Waveguide geometry:** The sample surface is first doped by indiffusing a ≈ 20 nm thick Tm layer yielding a concentration profile of ≈ 6 μm depth with $\approx 10^{20}$ ions per cm^3 surface concentration. Subsequently a 3 μm wide channel waveguide is fabricated by indiffusion of a 40 nm thick vacuum-deposited Ti stripe. AFC preparation light and single photons are coupled in and out of the waveguide with 10% total efficiency by butt-coupling single mode fibers. **b. Simplified energy level diagram of Tm ions:** The optical coherence time of the ^{3}H$_6$-^{3}H$_4$ transition at 3 K is 1.6 μs, and the radiative lifetimes of the ^{3}H$_4$ and ^{3}F$_4$ levels are 82 μs and 2.4 ms, respectively. A 570 G magnetic field splits the ground and excited levels into Zeeman sub-levels. The ground Zeeman level splitting is $\sim$ 83 MHz, and the lifetime of the upper ground level exceeds one second. **c. 5 GHz-bandwidth AFC:** The tooth separation is $\Delta_\nu = 167$ MHz, corresponding to 6 ns storage time. The line-width of the teeth is $\gamma = 83$ MHz.

profile, Tm ions with transition frequencies within the comb's troughs are optically pumped via the excited level into long-lived nuclear Zeeman levels, see Fig. 5.2b [26, 28]. To achieve frequency selective optical pumping we employed a linear side-band chirp technique [15, 29] that allowed us to create a 5 GHz broad grating (matching the spectral width of the 795 nm photons) with tooth spacing of 167 MHz, see Fig. 5.2c. This corresponds to a storage time of 6 ns. After each 10 ms-long AFC preparation a 2.2 ms-long wait time allows atoms excited by the optical pumping to decay before photon storage (see Fig. 5.1b for the timing

per experimental cycle). A set of micro electro-mechanical switches (MEMS) then open the channel for qubits to enter the memory, and, after recall, direct them towards the Si-APD. We assessed our memory's retrieval efficiency to be $(2 \pm 0.5)\%$. Taking the 10 dB fibre-to-fibre coupling loss in and out of the waveguide into account, this yields an overall system efficiency of approximately 0.2% [15].

An interesting and useful aspect of photon-echo quantum memory protocols is that they provide a robust tool to manipulate time-bin qubits [30, 4, 31, 32]. For example, by using the AFC approach, any projection measurement on time-bin qubit states can be performed by superimposing two combs (double AFC) with appropriately chosen relative center frequencies and amplitudes [4]. This leads to two re-emission times that can be set to differ by the temporal mode separation of the qubit to be analyzed (1.4 ns for our experiments). Hence, as a previously absorbed photon is re-emitted by the superimposed combs, early and late temporal modes interfere, allowing the qubit state to be analyzed in the same way as is typically done with an imbalanced Mach-Zehnder interferometer [4]. Double AFC recall will, however, lead to a reduction of the recall efficiency (compared to single recall).

5.3 Measurements and Results

To demonstrate faithful storage and retrieval of quantum states from the memory, we performed projection measurements with various time-bin qubits onto different bases using single (standard) and double AFC schemes as explained before. In all our measurements the average photon number per qubit was 0.1 at the output of the qubit-encoding interferometer. First we generated qubit states that occupy only early $|e\rangle$ or late $|l\rangle$ temporal modes by blocking either the long or short arm of the qubit-encoding interferometer, respectively, and then stored these states in the memory for 6 ns. Fig. 5.3 (left) shows single detections (no

conditioning) of the retrieved photons as a function of the time difference with respect to the START signal. The dark counts from the Si-APD reduce the signal to noise ratio (SNR) to ~ 5. For an input state $|e\rangle$, we compute the fidelity as $\mathcal{F}_e = C_{e|e}/(C_{e|e} + C_{l|e})$, where, e.g., $C_{l|e}$ denotes the number of detected counts in the late time-bin given $|e\rangle$ was encoded in the qubit at the input. Similarly, we can find $\mathcal{F}_l$, enabling us to calculate the mean fidelity: $\mathcal{F}_{el} = (\mathcal{F}_e + \mathcal{F}_l)/2 = 0.8514 \pm 0.0004$.

On the other hand, conditioning the detections of the retrieved photons on the detection of 1532 nm photons leads to a substantial increase of the SNR to ~ 22, as shown in Fig. 5.3 (right). This yields a mean fidelity of $\mathcal{F}^*_{el} = 0.9539 \pm 0.0024$.

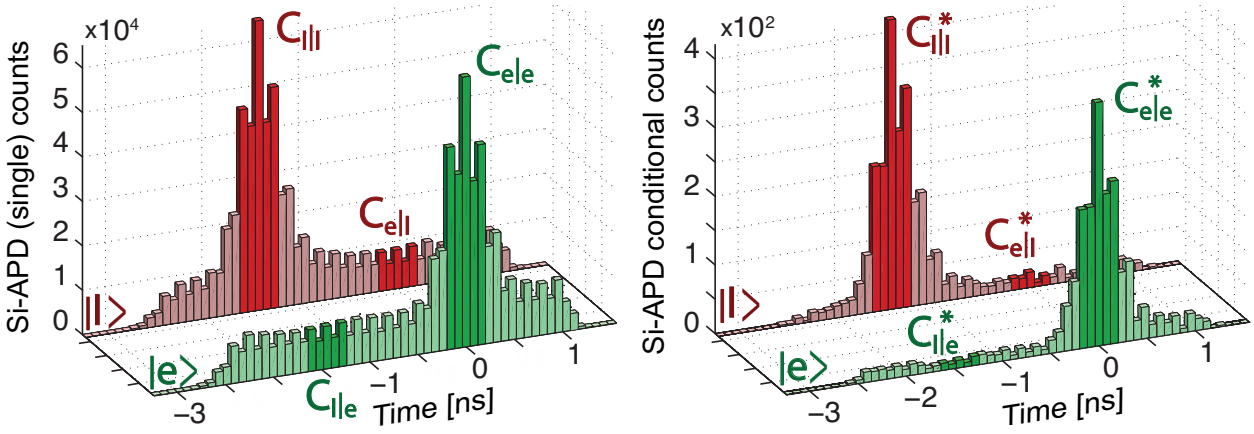

Figure 5.3: (color online) **Storage of early and late time-bin qubit states in the AFC memory:** The left-hand figure depicts the histograms from 180 min of single detections of the retrieved 795 nm photons prepared in early (red) and late (green) qubit states with the highlighted regions marking the relevant detection windows. The right-hand figure shows the detections conditioned on 1532 nm photons for the same states. Without conditioning the fidelities are $\mathcal{F}_e = 0.8652 \pm 0.0006$ and $\mathcal{F}_l = 0.8376 \pm 0.0004$ for the storage of early and late time-bin states, respectively. Correspondingly, with conditioning, the fidelities are $\mathcal{F}^*_e = 0.9505 \pm 0.0058$ and $\mathcal{F}^*_l = 0.9573 \pm 0.0033$.

Next, qubit states in an equal superposition of early and late temporal modes $\frac{1}{\sqrt{2}}(|e\rangle + e^{i\phi}|l\rangle)$ were produced with ϕ set to zero. Storage and projection measurements were performed using

the double AFC scheme with the relative phase of the two combs (measured w.r.t. the phase introduced by the qubit-encoding interferometer) varied by $\pi/2$ increments. The results for single and conditional detections are given in Fig. 5.4. The histograms show the detection statistics for zero and π double AFC phase settings, from which we extract a SNR slightly above 1 for the single, and above 6 for the conditional detection. In the lower part of Fig. 5.4 we show the normalized counts for each projection setting for the single and conditional detections. Fitting sinusoidal curves to these we derive visibilities $\mathcal{V}$, which, in turn, yield a fidelity $\mathcal{F} = (1+\mathcal{V})/2$ for single detections of $\mathcal{F}_\phi = 0.682 \pm 0.020$. For conditional detections we find a significantly larger value of $\mathcal{F}_\phi^* = 0.851 \pm 0.030$. These figures allow establishing an average, single detection fidelity: $\overline{\mathcal{F}} \equiv (\mathcal{F}_{el} + 2\mathcal{F}_\phi)/3 = 0.738 \pm 0.029$. This violates the quantum classical bound [33] of ~ 0.667, thus verifying that our memory outperforms any classical storage protocol. However, it is below the bound of ~ 0.833 for an optimal universal quantum cloner [34]. Harnessing the conditional detection we find $\overline{\mathcal{F}^*} = 0.885 \pm 0.020$. This beats the quantum-classical bound by 10 standard deviations and also violates the optimal universal quantum cloner bound by 2.5 standard deviations.

5.4 Conclusion and Discussion

To conclude, we have demonstrated storage, retrieval, and conditional detection of different time-bin qubit states using a solid-state Ti:Tm:LiNbO3 waveguide quantum memory with average fidelity $\overline{\mathcal{F}^*} = 0.885 \pm 0.020$, which exceeds the relevant classical bounds. Operating the memory in a heralded fashion is readily achievable with high-rate APDs that have recently become commercially available. Despite our memory device's current limitations, namely efficiency, storage time, and preset recall time, the high fidelity and the wide spectral acceptance makes our approach promising for future quantum communication schemes and quantum networks. The $LiNbO_3$ host crystal and the waveguide structure have potential advantages in quantum memory applications such as fast electric field control of collective

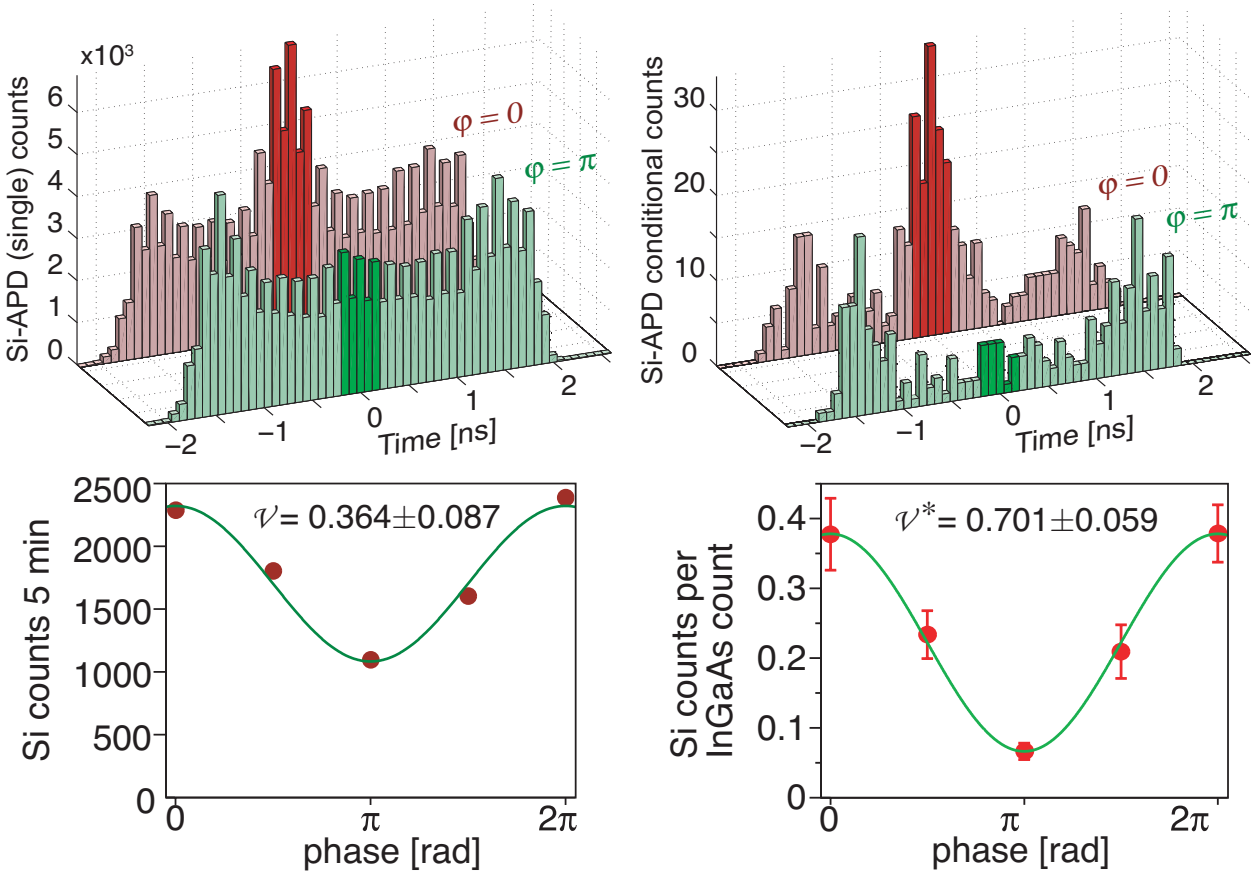

Figure 5.4: (color online) **Retrieval of qubits created in a superposition of early and late temporal modes:** The top left figure presents histograms of single detections of the retrieved 795 nm photons with AFC phase settings of zero (red) and π (green), collected during 80 min. The top right figure shows the same histograms for conditional detections. The highlighted regions mark detection windows used to derive projection probabilities required to calculate fidelities. The lower curves show single and coincidence counts obtained for all phase settings for single detections (left) and conditional detections (right), yielding visibilities of 0.364 ± 0.087 and 0.701 ± 0.059, respectively.

atomic phase evolution and, due to the resemblance with building blocks of classical integrated optical devices [35], it holds promise for simple integration with existing information technology. Furthermore, the ability to perform projection measurements using a photon-echo memory provides a simple and robust tool that might find use in other applications of quantum information processing.

Bibliography

[1] B. Julsgaard, J. Sherson, J. I. Cirac, J. F. caronek, and E. S. Polzik, Nature 432, 482 (2004)

[2] H. de Riedmatten, M. Afzelius, M. U. Staudt, C. Simon, and N. Gisin, Nature 456, 773 (2008)

[3] S. Massar and S. Popescu, Phys. Rev. Lett. 74, 1259 (1995)

[4] V. Buek and M. Hillery, Phys. Rev. A 54, 1844 (1996)

[5] H.-J. Briegel et al., Phys. Rev. Lett. 81, 5932 (1998)

[6] N. Sangouard et al., Rev. Mod. Phys. 83, 33 (2011)

[7] J. Kimble, Nature 453, 1023 (2008)

[8] P. Kok et al., Rev. Mod. Phys. 79, 135 (2007)

[9] H. P. Specht et al., Nature 473, 190 (2011)

[10] H. Tanji et al., Phys. Rev. Lett. 103, 043601 (2009)

[11] W. Tittel et al., Laser Photon. Rev. 4, 244 (2010)

[12] A. I. Lvovsky, B. C. Sanders and W. Tittel, Nature Photon. 3, 706 (2009)

[13] M. Hosseini et al., Nature Phys. 7, 794 (2011)

[14] A. G. Radnaev et al., Nature Phys. 6, 894 (2010)

[15] E. Saglamyurek et al., Nature 469, 512 (2011)

[16] C. Clausen et al., Nature 469, 508 (2011)

[17] H. Zhang et al., Nature Photon. 5, 628 (2011)

[18] I. Usmani et al., Nature Commun. 1, 12 (2010)

[19] K. F. Reim et al., Phys. Rev. Lett. 107, 053603 (2011)

[20] M. Hedges et al., Nature 465, 1052 (2010)

[21] K. Akiba et al., New J. Phys. 11, 013049 (2009)

[22] M. D. Eisaman et al., Rev. Sci. Instrum. 82, 071101 (2011)

[23] ID Quantique SA, Phys. Today 64, 59 (2011)

[24] N. Sinclair et al., J. Lumin. 130, 1586 (2010)

[25] M. A1fzelius et al., Phys. Rev. A 79, 052329 (2009)

[26] W. Tittel and G. Weihs, Quantum Inf. Comput. 1, No. 2, 3 (2001)

[27] C. Thiel, T. Bottger, and R. Cone, J. Lumin. 131, 353 (2011)

[28] C. W. Thiel et al., J. Lumin. 130, 1598 (2010)

[29] R. R. Reibel et al., J. Lumin. 107, 103 (2004)

[30] S. A. Moiseev and B. S. Ham, Phys. Rev. A 70, 063809 (2004)

[31] M. Hosseini et al., Nature 461, 241 (2009)

[32] S. A. Moiseev and W. Tittel, Phys. Rev. A 82, 012309 (2010)

[33] S. Massar and S. Popescu, Phys. Rev. Lett. 74, 1259 (1995)

[34] V. Buzek and M. Hillery, Phys. Rev. A 54, 1844 (1996)

[35] W. Sohler et al., Opt. Photonics News 19, 24 (2008)

Chapter 6

Storage of Entangled Photons at 795 nm

The need for quantum memory in a quantum repeater architectures has been introduced in Chapter 1. An important property of such a quantum memory in the context of quantum repeaters is that it should preserve entanglement during storage.

This Chapter describes a reversible mapping of one member of an entangled photon pair into and out of our solid-state quantum memory as shown in Figure 6.1 (A). The time-bin entangled qubit pair, centered at wavelengths around 795 nm and 1532 nm, are generated via a spontaneous parametric down conversion technique. A 795 nm-photon is transmitted to a quantum memory and its state is mapped onto a collective excitation of thulium ions while the 1532 nm-photon is traveling through an optical fibre, thereby generating light-matter entanglement. Some time later, the atomic state is mapped back onto a photon. In order to verify entanglement between a recalled and non-stored photon, projective measurements, as shown in Figure 6.1 (B), are performed for a Bell inequality test and quantum state tomography.

In this Chapter, the experiment was conducted in collaboration with Erhan Saglamyurek, Neil Sinclair, Joshua A. Slater, Daniel Oblak, Félix Bussières. The thulium-doped $LiNbO_3$ waveguide was fabricated and charaterized by Mathew George, Raimund Ricken, and Wolfgang Sohler. Wolfgang Tittel conceived and directed the expeirment. I contributed to this study in the following stages : building the source of photonic entanglement and measurement setups, as well as performing the measurements.

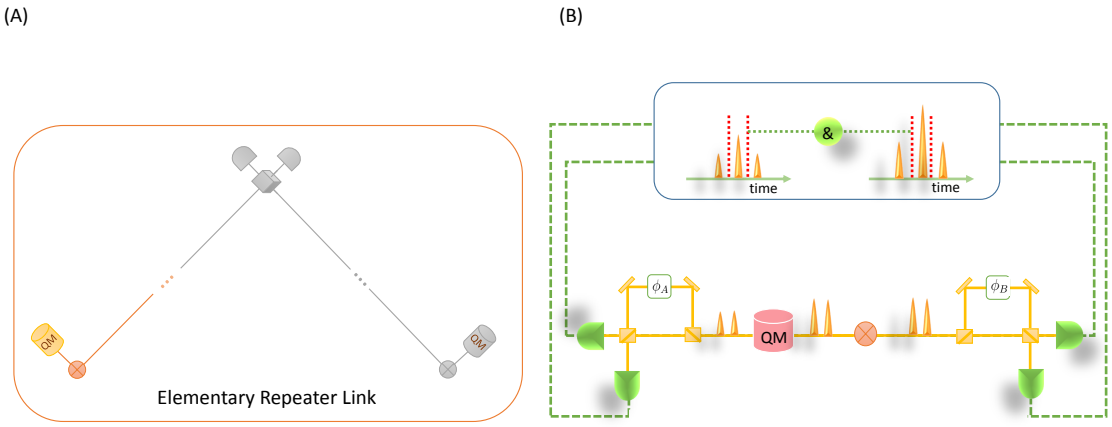

Figure 6.1: **Storage and retrieval of photonic entanglement.** (A) A schematic diagram of entanglement storage in the architecture of elementary quantum-repeater link. (B) Measurement setup for verifying the memory capability of preserving entanglement during storage. $\otimes$ and QM denotes time-bin entangled photons and a quantum memory, respectively.

Nature 469, 512 (2011)

Broadband Waveguide Quantum Memory for Entangled Photons

Erhan Saglamyurek[1], Neil Sinclair[1], Jeongwan Jin[1], Joshua A. Slater[1], Daniel Oblak[1], Félix Bussières[1], Mathew George[2], Raimund Ricken[2], Wolfgang Sohler[2], and Wolfgang Tittel[1]

[1]*Institute for Quantum Information Science, and Department of Physics and Astronomy, University of Calgary, 2500 University Drive NW, Calgary, Alberta T2N 1N4, Canada*

[2]*Department of Physics - Applied Physics, University of Paderborn, Warburger Str. 100, 33095 Paderborn, Germany*

Abstract

The reversible transfer of quantum states of light into and out of matter constitutes an important building block for future applications of quantum communication: it will allow the synchronization of quantum information [1], and the construction of quantum repeaters [2] and quantum networks [3]. Much effort has been devoted to the development of such quantum memories [1], the key property of which is the preservation of entanglement during storage. Here we report the reversible transfer of photon–photon entanglement into entanglement between a photon and a collective atomic excitation in a solid–state device. Towards this end, we employ a thulium-doped lithium niobate waveguide in conjunction with a photon-echo quantum memory protocol [4], and increase the spectral acceptance from the current maximum [5] of 100 Megahertz to 5 Gigahertz. We assess the entanglement-preserving nature of our storage device through Bell inequality violations [6] and by comparing the amount of entanglement contained in the detected photon pairs before and after the reversible transfer. These measurements show, within statistical error, a perfect mapping process. Our broadband quantum memory complements the family of robust, integrated lithium niobate devices [7]. It simplifies frequency-matching of light with matter interfaces in advanced applications of quantum communication, bringing fully quantum-enabled networks a step closer.

6.1 Introduction

Quantum communication is founded on the encoding of information, generally referred to as quantum information, into quantum states of light [6]. The resulting applications of quantum physics at its fundamental level offer cryptographic security through quantum key distribution without relying on unproved mathematical assumptions [8] and allow for the disembodied transfer of quantum states between distant places by means of quantum teleportation [6]. Reversible mapping of quantum states between light and matter is central to advanced applications of quantum communication such as quantum repeaters [2] and

quantum networks [3], in which matter constitutes nodes that hold quantum information until needed, and thereby synchronize the information flow through the communication channel or network. Furthermore, such a quantum interface allows the generation of light–matter entanglement through the mapping of one of two entangled photons into matter. To determine whether and how different physical systems can be entangled, and to localize the fundamental or technological boundaries where this fascinating quantum link breaks down, are central goals in quantum physics and have received much attention over the past decades [6].

The reversible light–matter interface can be realized through the direct transfer of quantum states from light onto matter and back, or through the generation of light–matter entanglement followed by teleportation of quantum information from an externally provided photon into matter, and eventually back. Experimental capabilities have advanced rapidly over the past years and quantum state transfer between light and atomic vapour [9, 10, 11, 12, 13], solid–state ensembles [4, 14], or single absorbers [15], as well as the generation of light–matter entanglement through the absorption of photons [16, 17, 18], or the emission of photons from atomic ensembles [19, 20, 21] or single emitters [22, 23] have all been reported.

For quantum memory to become practical, it is important to reduce the complexity of experimental implementations, and the recent addition of rare-earth-ion-doped crystals [4, 14] to the set of storage materials has been a valuable step towards this goal. The promise of such crystals is further enhanced through potentially long storage times–up to several seconds in $Pr:Y_2SiO_5$ [24]. In addition, given the large inhomogeneous broadening of optical zero-phonon lines, up to 100 Gigahertz (GHz), rare-earth-ion-doped crystals in principle offer storage of photons with less than 100-picosecond duration when being used in conjunction with a suitable quantum memory protocol [4]. Yet, the reversible state transfer between light and solid–state devices has so far not been shown to preserve entanglement. This is

largely due to the limited spectral bandwidth of current implementations, 100 Megahertz (MHz) at most [5], which is orders of magnitude smaller than that of entangled photon pairs generated in the widely used process of spontaneous parametric down-conversion [6]. In this work, we approach the problem from both ends: we increase the acceptance bandwidth of our storage device to 5 GHz and narrow the bandwidths of our entangled photons to similar values. Furthermore, by using a wave-guiding storage medium, we move fundamental quantum memory research further towards application.

6.2 Experiment

The layout of our experiment is depicted in Fig. 6.2. Short pulses of 523-nm wavelength light travel through an unbalanced interferometer. For sufficiently small pulse energies, subsequent spontaneous parametric down-conversion yields, to a good approximation, individual pairs of photons, centred at wavelengths around 795 nm and 1,532 nm, in the time-bin entangled qubit state [25]:

$$\left|\phi^{+}\right\rangle = \frac{1}{\sqrt{2}}\left(|e,e\rangle + |l,l\rangle\right) \tag{6.1}$$

Here, $|e\rangle$ and $|l\rangle$ denote early and late temporal modes and replace the usual spin-down and spin-up notation for spin-half particles. More specifically, $|i,j\rangle$ denotes a quantum state in which the 795-nm photon has been created in the temporal mode i, and the 1,532-nm photon has been created in the temporal mode j. We point out that, owing to the spectral filtering, our source generates frequency-uncorrelated entangled photons at wavelengths that match the low-loss windows of free-space and standard telecommunication fibre. It can thus be readily used in real-world applications of quantum communication that involve quantum teleportation and entanglement swapping.

The 1,532-nm photon is directed to a qubit analyser. It consists of either a fibre delay line followed by a single-photon detector that monitors the photon's arrival time, or a fibre-optical

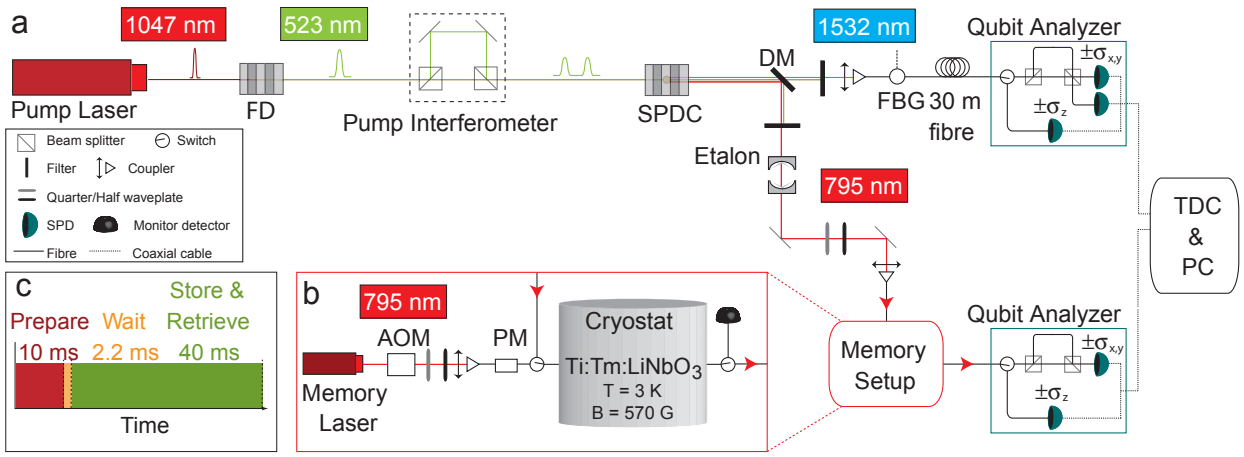

Figure 6.2: **Schematics of the experimental set-up: a**. Generating and measuring entanglement. Six-picosecond-long pump laser pulses (1,047.328 nm wavelength, 80 MHz repetition rate) are frequency doubled (FD) in a periodically poled lithium niobate (PPLN) crystal. Each resulting 16-ps-long pulse (523.664-nm wavelength, 90 mW average power) is coherently split into two by the unbalanced pump interferometer, featuring a 1.4-ns travel–time difference. Spontaneous parametric down-conversion (SPDC) in a second PPLN crystal followed by frequency filtering using an etalon and a fibre Bragg grating (FBG) (bandwidths of 6 GHz and 9 GHz, respectively), yields maximally entangled pairs of photons centred at 795.506-nm and 1,532.426-nm wavelength (DM, dichroic mirror). The 1,532-nm photon travels through a 30-m telecommunication fibre, and the 795-nm photon is either stored in the memory or sent through a fibre delay line (not pictured). To characterize the bi-photon state, we use qubit analysers consisting of delay lines or unbalanced interferometers connected to single-photon detectors. Detection events are collected with a time-to-digital converter (TDC) connected to a personal computer (PC). All interferometers are phase-locked to stable reference lasers (not shown). **b**. Memory set-up. The 795.506-nm continuous-wave memory laser beam is intensity- and phase/frequency-modulated using an acousto-optic modulator (AOM) and a phase modulator (PM). The waveguide is cooled to 3 K and exposed to a 570-G magnetic field aligned with the crystal's C_3-axis. Waveplates allow adjusting the polarization of the beam to the waveguide's transverse magnetic (TM) mode, and optical switches combine and separate the optical pump beam and the 795-nm photons. **c**. Timing sequence. We use three continuously repeated phases: the 10 ms "prepare" phase for optical pumping, the 2.2-ms "wait" phase, which ensures stored photons are not polluted by fluorescence from the excited state, and the 40-ms "store and retrieve" phase, during which many 795-nm photons are successively stored in the waveguide and recalled after 7 ns.

interferometer that is unbalanced in the same way as the pump interferometer, followed by single-photon detectors. The role of the delay line is to perform projection measurements of the photon's state onto early and late qubit states. Alternatively, the interferometer enables projections onto equal superpositions of early and late modes [25]. Using the language of spin-half systems, this corresponds to projections onto σ_z and, for appropriately chosen phases, σ_x and σ_y, respectively.

The 795-nm photon is transmitted to the quantum memory where its state –specifically that it is entangled with the 1,532-nm photon– is mapped onto a collective excitation of millions of thulium ions. Some time later, the state is mapped back onto a photon that exits the memory through a fibre in well-defined spatio-temporal modes and is probed by a second qubit analyser.

To reversibly map the 795-nm photon onto matter, we use a photon-echo quantum memory protocol based on atomic frequency combs (AFC) [4]. It is rooted in the interaction of light with an ensemble of atomic absorbers (so far rare-earth-ion-doped crystals cooled to cryogenic temperatures) with an inhomogeneously broadened absorption line that has been tailored into a series of equally spaced absorption peaks (see Fig. 6.3). The absorption of a single photon leads to a collective excitation shared by many atoms. Owing to the particular shape of the tailored absorption line, the excited collective coherence rapidly dephases and repeatedly recovers after multiples of the storage time T_s. This results in the re-emission of a photon in the state encoded into the original photon.

In our implementation the moment of photon re-emission is predetermined by the spacing of the teeth in the comb, $T_s = 1/\Delta$, and the storage process can be described as arising from the linear response of an optical filter made by spectral hole burning. Yet, readout

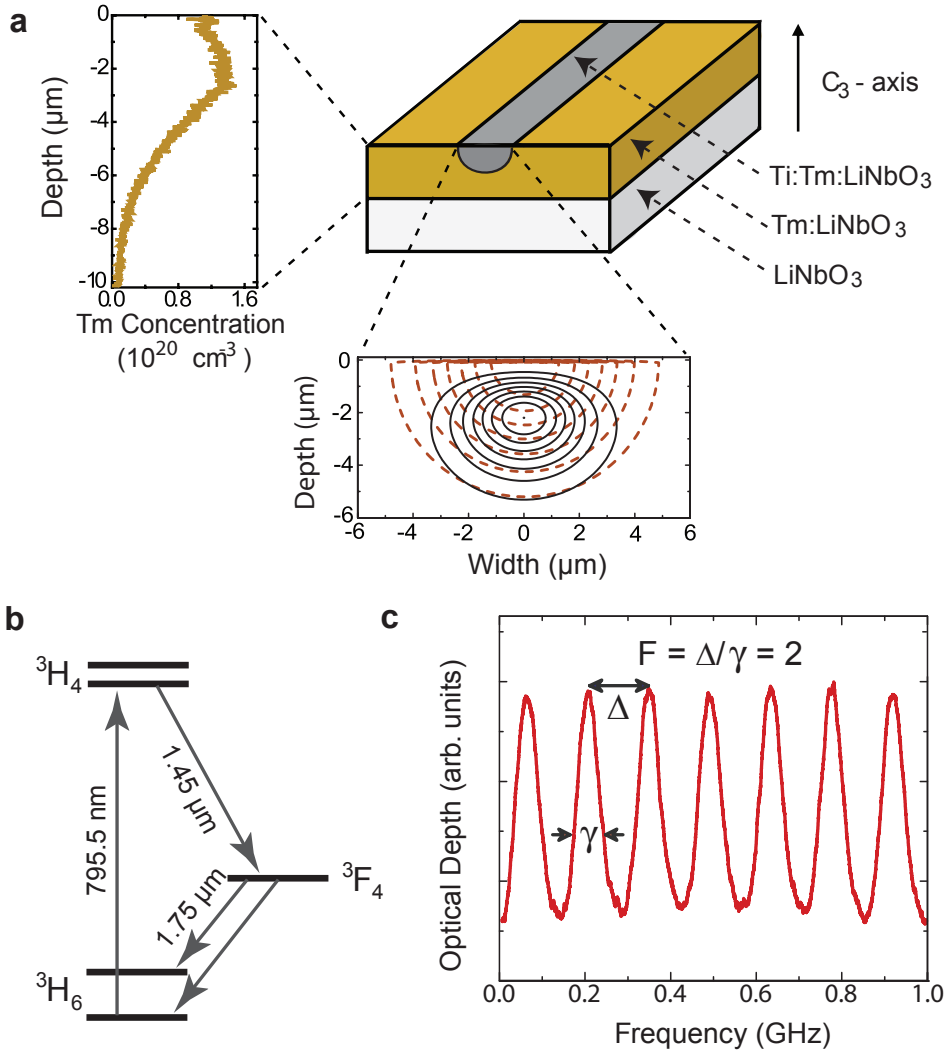

Figure 6.3: **The storage medium: a**. Waveguide geometry. The measured thulium (Tm) concentration profile is given on the left and the calculated intensity distribution of the fundamental TM-mode at the 795-nm wavelength is shown below. Iso-intensity lines are plotted corresponding to 90%, 87.5%, 75% and so on of the maximum intensity. **b**. Simplified energy level diagram of thulium ions. The optical coherence time of the $^3H_6 \leftrightarrow ^3H_4$ transition at 3 K is 1.6 μs, the radiative lifetimes of the $^3H_4$ and $^3F_4$ levels are 82 μs and 2.4 ms, respectively, and the branching ratio from the $^3H_4$ to the $^3F_4$ level is 44%. Upon application of a magnetic field of 570 G, the ground and excited levels split into magnetic sublevels with lifetimes exceeding one second [27].**c**. Atomic frequency comb. The bandwidth of our AFC is 5 GHz (shown here is a 1-GHz broad section). The separation between the teeth is $\Delta \approx 143$ MHz, resulting in 7 ns storage time. The line width of the peaks is $\gamma \approx 75$ MHz, yielding a finesse $F = 2$, as expected for the sinus-type comb.

on demand can be achieved by temporarily mapping the optically excited coherence onto ground-state coherence where the comb spacing is smaller or the comb structure is washed out [4], or by combining the AFC protocol with controlled reversible inhomogeneous broadening of each absorption line, similar to the storage mechanism used in another photon-echo quantum memory protocol [1].

Our storage device, a Ti:Tm:$LiNbO_3$ optical waveguide cooled to 3 K, is detailed in Fig. 6.3. It was previously characterized to establish its suitability as a photon-echo quantum memory material [26]. It combines interesting properties from the specific rare-earth element (795-nm storage wavelength), the host crystal (allowing for controlled dephasing and rephasing by means of electric fields), and from the wave-guiding structure (ease-of-use). Lithium niobate waveguides have also been doped with neodymium, praseodymium and erbium [7], and we conjecture that other rare-earth ions could also be used. This could extend the properties of $LiNbO_3$ and allow an integrated approach to other storage wavelengths, ions with different level structures, and so on.

To generate the AFC, we use a sideband-chirping technique (see Supplementary Information) to transfer atomic population between magnetic sublevels and create troughs and peaks in the inhomogeneously broadened absorption line. They form a 5-GHz-wide comb with tooth spacing of 143 MHz, setting the storage time to 7 ns. The system efficiency in our implementation is currently about 0.2%. This is in part due to the 90% fibre-to-waveguide input and output coupling loss, which we attribute to imperfect mode overlap. In addition, owing to the specific level structure of thulium under current experimental conditions, the finesse of the comb in the broadband approach is two, which limits the memory efficiency to about 10%. However, imperfections in the creation of the comb decrease this efficiency to around 2%. The system efficiency can be increased by improving the spectral tailoring of

the AFC, and triggering photon re-emission in the backward direction. By also optimizing the mode overlap, we anticipate that it could reach approximately 15%. Furthermore, if the two long-lived atomic levels between which population is transferred during the optical pumping procedure (in our case the two magnetic ground states; see Fig. 6.3) are spaced by more than the storage bandwidth, the memory efficiency can theoretically reach unity (see Supplementary Information).

6.3 Measurements and Results

To assess the quantum nature of our light–matter interface, we first make projection measurements with the 795 nm photons and the 1532 nm photons onto time-bin qubit states characterized by Bloch vectors aligned along $\boldsymbol{a}$, $\boldsymbol{b}$, respectively, where $\boldsymbol{a}, \boldsymbol{b} \in [\pm\sigma_x, \pm\sigma_y, \pm\sigma_z]$ (see Fig. 6.4). Experimentally, this is done by means of suitably adjusted qubit analyzers, and by counting the number $C(\boldsymbol{a}, \boldsymbol{b})$ of detected photon pairs. From two such spin-measurements, we calculate the normalized *joint-detection probability*

$$P(\boldsymbol{a}, \boldsymbol{b}) = \frac{C(\boldsymbol{a}, \boldsymbol{b})}{C(\boldsymbol{a}, \boldsymbol{b}) + C(\boldsymbol{a}, -\boldsymbol{b})} \tag{6.2}$$

The measurement and the results with the fibre delay line, as well as the memory, are detailed in Fig. 6.4 and the Supplementary Information. From this data, we reconstruct the bi-photon states before and after storage in terms of their density matrices ρ_{in} and ρ_{out}, depicted in Fig. 6.4, using a maximum likelihood estimation [27]. This, in turn, allows us to examine the entanglement of formation [28], a measure that indicates entanglement if it exceeds zero; it is upper-bounded by one. The results, listed in Table 6.1, clearly show the presence of entanglement in ρ_{in} and ρ_{out} and, within experimental uncertainty, establish that the storage process preserves entanglement without measurable degradation. Furthermore, we note that the fidelity $\mathcal{F}$ between ρ_{in} and ρ_{out} is close to one, and hence the unitary transformation introduced by the storage process is almost the identity transformation.

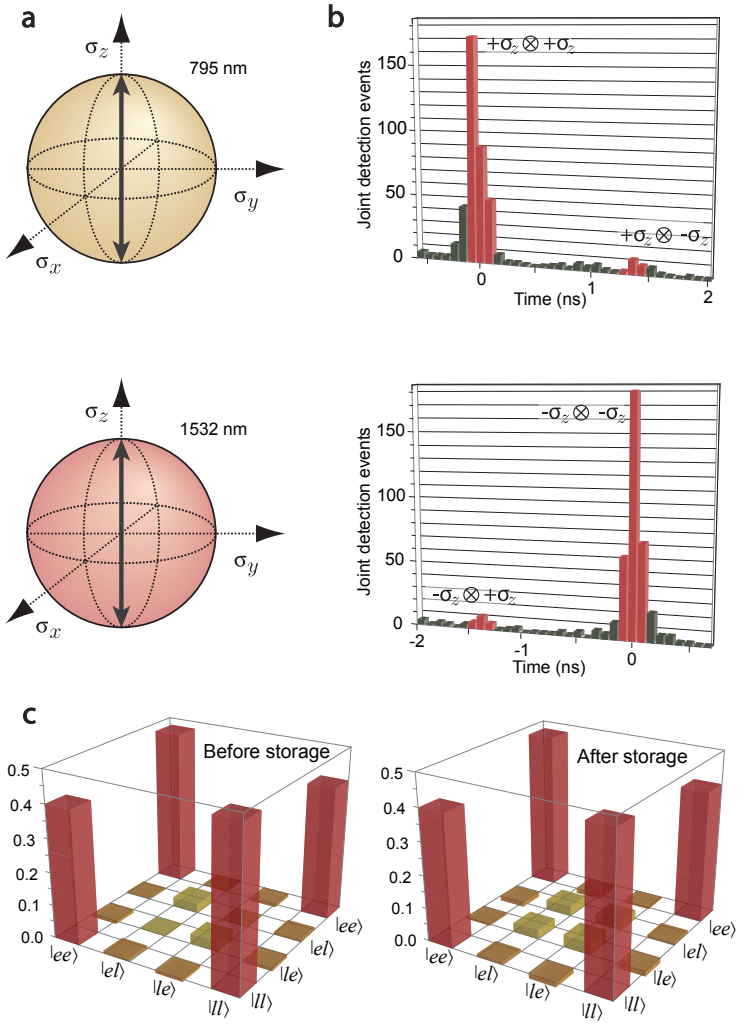

Figure 6.4: **Measurement of density matrices: a**. Visualization of projection measurements. The measurement settings for the 795-nm (or 1,532-nm) qubit analyser are depicted on the upper (or lower) Bloch sphere. The example shows joint settings that enable calculating normalized probabilities for projections onto $\sigma_z \otimes \sigma_z$ $\sigma_z \otimes -\sigma_z$. **b**. Results for joint projection measurement after storage. The top (bottom) histogram displays joint detection events for the projection onto $\sigma_z \otimes \sigma_z$ and $\sigma_z \otimes -\sigma_z$($-\sigma_z \otimes \sigma_z$ and $-\sigma_z \otimes -\sigma_z$) as a function of the time difference between detections of the 795-nm and the 1,532-nm photons. The desired events are those within the red-highlighted time windows. This allows us to calculate the joint-detection probabilities for projections onto $\sigma_z \otimes \sigma_z$ and $\sigma_z \otimes -\sigma_z$ (for results with other joint settings see the Supplementary Information). **c**. Density matrices. Density matrices were calculated using a maximum-likelihood estimation for the bi-photon states before and after storage. Only the real parts are shown-the absolute values of all imaginary components are below 0.04.

	Entanglement of formation (%)	Purity (%)	Fidelity with $\|\phi^+\rangle$	Input/output fidelity (%)	Expected S_{th}	Measured S
ρ_{in}	64.4 ±4.2	75.7 ± 2.4	86.2±1.5		2.235 ±0.085	2.379 ±0.034
ρ_{out}	65 ±11	76.3±5.9	86.6 ±3.9	95.4 ±2.9	2.2 ±0.22	2.25 ±0.060.22

Table 6.1: **Entanglement measures, purities and fidelities:** Entanglement of formation (normalized with respect to the entanglement of formation of $|\phi^+\rangle$, purity P=tr(ρ^2)), fidelity with $|\phi^+\rangle$, input–output fidelity $\mathcal{F} = \left(\mathrm{tr}\sqrt{\sqrt{\rho_{out}}\rho_{in}\sqrt{\rho_{out}}}\right)^2$ (referring to the fidelity of ρ_{out} with respect to ρ_{in}), and expected and experimentally obtained S values for tests of the CHSH Bell inequality (measured for $\boldsymbol{a} = \sigma_x$, $\boldsymbol{a'} = \sigma_y$, $\boldsymbol{b} = \sigma_x + \sigma_y$ and $\boldsymbol{b'} = \sigma_x - \sigma_y$). The correlation coefficients used to compute S and the calculation of S_{th} are detailed in the Supplementary Information. We note that the original state (and hence the recalled state) has limited purity and fidelity with $|\phi^+\rangle$. This is due to the probabilistic nature of our spontaneous parametric down-conversion source, which features a non-negligible probability of generating more than two photons simultaneously [26]. Uncertainties indicate one-sigma standard deviations and are estimated from Poissonian detection statistics and using a Monte Carlo simulation

In addition, as a second entanglement measure, we perform tests of the Clauser–Horne–Shimony–Holt (CHSH) Bell inequality [6]. This test indicates non-local correlations and thus the possibility of using the bi-photons for entanglement-based quantum key distribution [**?**] if the sum:

$$S = |E(\boldsymbol{a},\boldsymbol{b}) + E(\boldsymbol{a'},\boldsymbol{b}) + E(\boldsymbol{a},\boldsymbol{b'}) - E(\boldsymbol{a'},\boldsymbol{b'})| \tag{6.3}$$

of four correlation coefficients

$$E(\boldsymbol{a},\boldsymbol{b}) = \frac{C(\boldsymbol{a},\boldsymbol{b}) - C(\boldsymbol{a},-\boldsymbol{b}) - C(-\boldsymbol{a},\boldsymbol{b}) + C(-\boldsymbol{a},-\boldsymbol{b})}{C(\boldsymbol{a},\boldsymbol{b}) + C(\boldsymbol{a},-\boldsymbol{b}) + C(-\boldsymbol{a},\boldsymbol{b}) + C(-\boldsymbol{a},-\boldsymbol{b})} \tag{6.4}$$

with appropriately chosen settings $\boldsymbol{a}$, $\boldsymbol{a'}$ and $\boldsymbol{b}$, $\boldsymbol{b'}$ exceeds the classical bound of two; quantum mechanically it is upper-bounded by $2\sqrt{2}$. As detailed in Table 6.1, we find $S_{in} = 2.379 \pm 0.034 > 2$ before the memory and, crucially, $S_{out} = 2.25 \pm 0.06 > 2$, which is in agreement with the value $S_{th} = 2.2 \pm 0.22$ predicted from the reconstructed density matrix ρ_{out}. This validates the suitability of our set-up for quantum communication.

6.4 Conclusion and Discussion

Our investigation provides an example of entanglement being transferred between physical systems of different nature, thereby adding evidence that this fundamental quantum property is not as fragile as is often believed. Furthermore, our broadband integrated approach permits the linkage of a promising quantum storage device with extensively used, high-performance sources of photons in bi- and multi-partite entangled states [6]. Although the storage efficiency and the storage time need to be significantly increased, and the moment of recall was pre-set, this study opens the way to new investigations of fundamental and applied aspects of quantum physics. Having increased the storage bandwidth also significantly facilitates the building of future quantum networks, because mutual frequency matching of photons and distant quantum memories will be simple. In addition, a large storage bandwidth –that is, the possibility to encode quantum information into short optical pulses– allows us to increase the number of temporal modes that can be stored during a given time. This enhances the flow of quantum information through a network and decreases the time needed to establish entanglement over a large distance using a quantum repeater [1, 2].

We note that, parallel to this work, Clausen et al. have demonstrated the storage of an entangled photon using a neodymium-doped crystal [29].

Bibliography

[1] Lvovsky, A. I., Sanders, B. C., &. Tittel, W. Optical quantum memory. Nature Photon. 3, 706–714 (2009)

[2] Sangouard, N., Simon, C., de Riedmatten, H. & Gisin, N. Quantum repeaters based on atomic ensembles and linear optics. Preprint at http://arxiv.org/abs/ 0906.2699 (2009)

[3] Kimble, H. J. The quantum Internet. Nature 453, 1023–1030 (2008)

[4] de Riedmatten, H., Afzelius, M., Staudt, M. U., Simon, C. & Gisin, N. A solid–state light–matter interface at the single-photon level. Nature 456, 773–777 (2008)

[5] Usmani, I., Afzelius, M., de Riedmatten, H. & Gisin, N. Mapping multiple photonic qubits into and out of one solid–state atomic ensemble. Nature Commun. 1, 1–7 (2010)

[6] Pan, J.-W., Chen, Z.-B., Zukowski, M., Weinfurter, H. & Zeilinger, A. Multi-photon entanglement and interferometry. Preprint at http://arxiv.org/abs/0805.2853 (2008)

[7] Sohler, W. et al. Integrated optical devices in lithium niobate. Opt. Photon. News 24–31 (2008)

[8] Gisin, N., Ribordy, G., Tittel, W. & Zbinden, H. Quantum cryptography. Rev. Mod. Phys. 74, 145–195 (2002)

[9] Julsgaard, B., Sherson, J. & Cirac, J. I. J. Fiurasek, J. & Polzik, E. S. Experimental demonstration of quantum memory for light. Nature 432, 482–486 (2004)

[10] Chaneliere, T. et al. Storage and retrieval of single photons transmitted between remote quantum memories. Nature 438, 833–836 (2005)

[11] Eisaman, M. D. et al. Electromagnetically induced transparency with tunable single-photon pulses. Nature 438, 837–841 (2005)

[12] Honda, K. et al. Storage and retrieval of a squeezed vacuum. Phys. Rev. Lett. 100, 093601 (2008)

[13] Appel, J., Figueroa, E., Korystov, D., Lobino, M. & Lvovsky, A. Quantum memory for squeezed light. Phys. Rev. Lett. 100, 093602 (2008)

[14] Hedges, M. P., Longdell, J. J., Li, Y. & Sellars, M. J. Efficient quantum memory for light. Nature 465, 1052–1056 (2010)

[15] Boozer, A. D. et al. Reversible state transfer between light and a single trapped atom. Phys. Rev. Lett. 98, 193601 (2007).

[16] Choi, K. S. Deng, H. Laurat, J. & Kimble, H. J. Mapping photonic entanglement into and out of a quantum memory. Nature 452, 67–71 (2008)

[17] Akiba, K., Kashiwagi, K. Arikawa, M. & Kozuma, M. Storage and retrieval of nonclassical photon pairs and conditional single photons generated by the parametric down-conversion process. N. J. Phys. 11, 013049 (2009)

[18] Jin, X.-M. et al. Quantum interface between frequency-uncorrelated down converted entanglement and atomic-ensemble quantum memory. Preprint at http://arxiv.org/abs/1004.4691 (2011)

[19] Chou, C. W. et al. Measurement-induced entanglement for excitation stored in remote atomic ensembles. Nature 438, 828–832 (2005)

[20] Matsukevich, D. N. et al. Entanglement of a photon and a collective atomic excitation. Phys. Rev. Lett. 95, 040405 (2005)

[21] Yuan, Z.-S. et al. Experimental demonstration of a BDCZ quantum repeater node. Nature 454, 1098–1101 (2008)

[22] Blinov, B. B., Moehring, D. L., Duan, L.M. & Monroe, C. Observation of entanglement between a single trapped atom and a single photon. Nature 428, 153–157 (2004)

[23] Togan, E. et al. Quantum entanglement between an optical photon and a solid state spin qubit. Nature 466, 730–734 (2010)

[24] Longdell, J., Fraval, E., Sellars, M. & Manson, N. Stopped light with storage times greater than one second using electromagnetically induced transparency in a solid. Phys. Rev. Lett. 95, 063601 (2005)

[25] Marcikic, I. et al. Time-bin entangled qubits for quantum communication created by femtosecond pulses. Phys. Rev. A 66, 062308 (2002)

[26] Sinclair, N. et al. Spectroscopic investigations of a Ti:Tm:$LiNbO_3$ waveguide for photon-echo quantum memory. J. Lumin. 130, 1586–1593 (2010)

[27] Altepeter, J. B., Jeffrey, E. R., &. Kwiat, P. G. Photonic state tomography. Adv. At. Mol. Opt. Phys. 52, 105–159 (2005)

[28] Plenio, M. B. & Virmani, S. An introduction to entanglement measures. Quant. Inf. Comput. 7, 1–51 (2007)

[29] Clausen, C. et al. Quantum storage of photonic entanglement in a crystal. Nature doi:10.1038/nature09662 (this issue).

Chapter 7

Storage of Entangled Photons at Telecom Wavelength

This Chapter introduces a commercially available erbium-doped optical fibre as a material for quantum storage. The fibre, cooled to 1 Kelvin, is used to map one member of an entangled photon pair onto the atomic state of erbium ions and retrieve it back onto a photonic state using the AFC quantum memory protocol. The two-photon states before and after the storage are reconstructed via a quantum state tomography technique. With a fidelity of 97.1 $\pm$ 4.9 % between the states before and after storage, the erbium-doped optical fibre reveals its capability of preserving entanglement during storage, thereby showing its suitability for being used in a quantum repeater. Moreover, due to ease of use, it can be easily integreated into telecommunication optical-fibre based quantum communications : the storage of entanglement as well as quantum bits by means of light-atom interaction in optical fibres!

In this Chapter, the experiment was conducted in collaboration with Erhan Saglamyurek and Daniel Oblak. Varun B. Verma, Matthew D. Shaw, Francesco Marsili, and Sae Woo Nam developed superconducting nanowire single-photon detectors used in the experiment. Wolfgang Tittel conceived and directed the expeirment. I contributed to this study in the following stages : building the source of photonic entanglement and measurement setups, performing the measurements, and analyzing the results.

Quantum storage of entangled telecom-wavelength photons in an erbium-doped optical fibre

Erhan Saglamyurek[1], Jeongwan Jin[1], Varun B. Verma[2], Matthew D. Shaw[3], Francesco Marsili[3], Sae Woo Nam[2], Daniel Oblak[1], and Wolfgang Tittel[1]

[1]*Institute for Quantum Information Science, and Department of Physics and Astronomy, University of Calgary, 2500 University Drive NW, Calgary, Alberta T2N 1N4, Canada*

[2]*National Institute of Standards and Technology, Boulder, Colorado 80305 USA* [3]*Jet Propulsion Laboratory, California Institute of Technology, 4800 Oak Grove Drive, Pasadena, California 91109, USA*

Abstract

The realization of a future quantum Internet requires processing and storing quantum information at local nodes, as well as interconnecting distant nodes using free-space and fibre-optic links[1]. Quantum memories for light[2] are key elements of such quantum networks. However, to date, neither an atomic quantum memory for non-classical states of light that operates at a wavelength compatible with standard telecom fibre infrastructure, nor a fibre-based implementation of a quantum memory has been reported. Here we demonstrate the storage and faithful recall of the state of a 1532 nm wavelength photon, entangled with a 795 nm photon, in an ensemble of cryogenically cooled erbium ions doped into a 20 meter-long silicate fibre using a photon-echo quantum memory protocol. Despite its currently limited efficiency and storage time, our broadband light-matter interface brings fibre-based quantum networks one step closer to reality. Furthermore, it paves the path towards novel tests of light-matter interaction and collective atomic effects in unconventional materials.

7.1 Introduction

The end of the last century witnessed the invention of, and important steps towards, several paradigm-shifting applications of quantum information science, including computers with unprecedented computational power[3], unbreakable secret key distribution[4], and measurement devices having ultimate precision[5]. Combining these applications in the so-called quantum Internet[1] requires transmitting quantum states encoded into photons between, and storage of quantum states in, nodes of the network. While the quantum Internet can leverage existing telecom fibre networks, standard (classical) repeater technology cannot be used to build large-scale networks, due to a fundamental restriction of quantum mechanics known as the no-cloning theorem[4]. Hence, classical repeaters, generally comprised of erbium-doped fibre amplifiers, need to be replaced with quantum repeaters, which include pairs of entangled photons, entanglement swapping, and light-matter interfaces that allow storing and manipulating quantum states of light[6].

Despite enormous success in developing suitable light-matter interfaces during the past decade (for recent reviews see [[2, 6, 7]]), a memory for non-classical states of light encoded into telecom-wavelength (i.e. approximately 1550 nm) photons — the most natural choice for a quantum network — still remains to be demonstrated. Considering the most popular materials – alkaline atoms (in particular caesium and rubidium), and rare-earth-ion doped crystals –, this challenge is due to two different reasons: First, Cs and Rb lack easily accessible atomic transitions, i.e. transitions starting at an electronic ground state, at around 1550 nm wavelength. Second, erbium (a rare-earth element and the seemingly obvious choice due to its telecom-wavelength transition and extensive use in fibre amplifiers) has so-far eluded all attempts to store non-classical states of light with a fidelity above the classical limit, albeit important steps towards this goal have recently been reported[8, 9]. Furthermore, in addition to telecom-wavelength storage, there is another milestone that,

if accomplished, would significantly benefit fibre-based quantum communication networks: the storage of non-classical states by means of light-atom interaction in optical fibres. This promises a simplified and robust setup – comparable to the use of an erbium fibre amplifier in standard telecom networks. We note that the use of a hollow core photonic crystal fibre filled with caesium atoms is a promising step in this direction[10].

Here we demonstrate that the apparent limitations of erbium for optical quantum memory can be overcome, and, furthermore, that quantum states of light can indeed be stored in impurities doped into an optical fibre. More precisely, employing a commercially available erbium-doped fibre cooled to around 1 K and exposed to a suitably chosen magnetic field, we report the storage and faithful recall of 1532 nm photons that are entangled with 795 nm photons using the atomic frequency comb (AFC) quantum memory protocol[11, 12].

7.2 Experiment

Our experimental setup, sketched and further explained in Fig. 7.1 and in the Methods section, is composed of three parts: a source of time-bin entangled photon pairs, a quantum memory for photons, and analyzers that allow projection measurements with the members of each entangled photon pair. First, using spontaneous parametric down-conversion of short laser pulses, we generate photon pairs with members at 795 nm and 1532 nm wavelength in a time-bin entangled state given by

$$\left|\phi^{+}\right\rangle = \frac{1}{\sqrt{2}}\left(|e,e\rangle + |l,l\rangle\right). \tag{7.1}$$

Here $|i,j\rangle$ denotes a quantum state in which the 795-nm photon has been created in the

temporal mode i, and the 1532-nm photon has been created in the temporal mode j. Furthermore, $i, j \in [e, l]$, and $|e\rangle$ and $|l\rangle$ label early and late temporal modes, respectively. The spectra of the 795 nm photon and the telecom photon are filtered to 6 GHz and 10 GHz, respectively, to allow subsequent storage of the 1532 nm photon in the erbium-doped fibre.

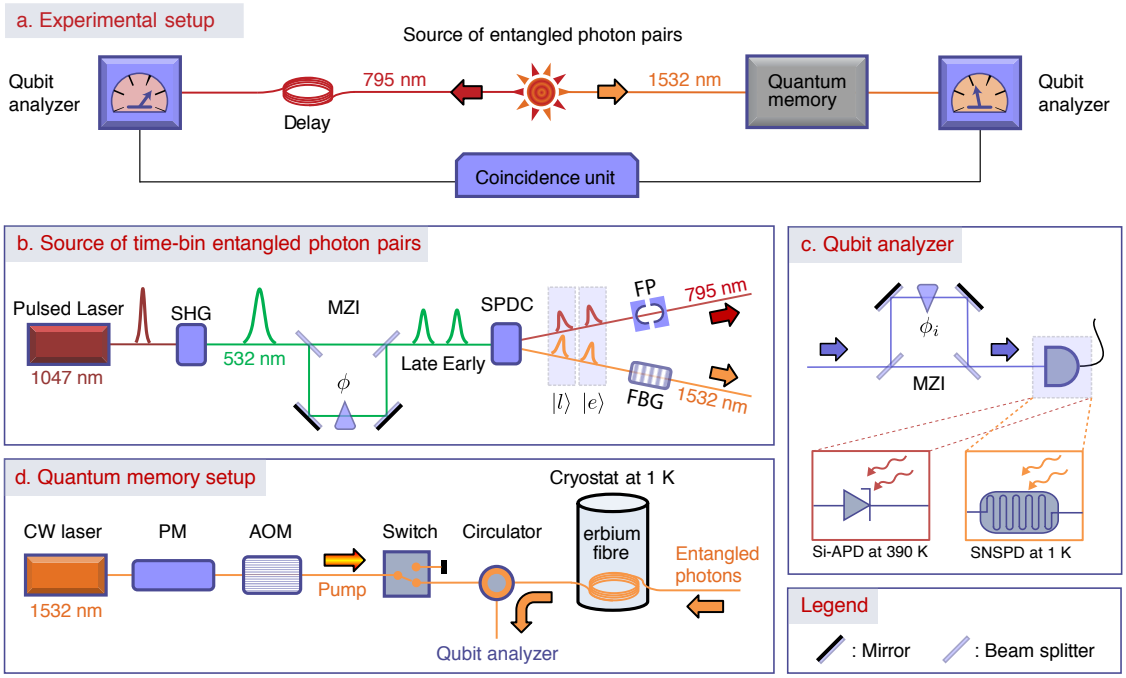

Figure 7.1: **Experimental setup. a) Schematic.** Our setup consists of three parts: the source of entangled photon pairs, the quantum memory, and analyzers (including a coincidence unit) that allow projecting the joint photon state onto qubit product states. Depending on the measurement, the entangled photons are either directly sent towards the analyzers, or the 1532 nm photon is first stored for 5 ns in an Erbium-doped fibre. **b) Photon pair source.** SHG – second harmonic generation; MZI – Mach-Zender interferometer; SPDC – spontaneous parametric down conversion; FP: Fabry-Perot cavity; FBG – fiber Bragg grating. **c) Analyzers.** SNSPD - superconducting nano-wire single photon detectors. **d) Quantum memory.** PM – phase modulator; AOM – acousto-optic modulator. For details on all components see the Methods section.

Second, to store the 1532 nm photons, we use a cryogenicly-cooled, commercially available erbium-doped fibre (see the Supplementary Information) in conjunction with the atomic frequency comb (AFC) quantum memory protocol[11, 12]. AFC-based storage relies on

tailoring an inhomogeneously broadened atomic transition (in our case the ${}^4I_{15/2} \leftrightarrow {}^4 I_{13/2}$ transition in Er^{3+}-ions) into a series of absorption lines that are equally spaced by frequency Δ – that is the atomic frequency comb (see Figure 7.2a, b). The absorption of a photon then creates a collective atomic excitation described by:

$$|\Psi\rangle_A = \frac{1}{\sqrt{N}} \sum_{j=1}^{N} c_j e^{i2\pi\delta_j t} e^{-ikz_j} |g_1, \cdots e_j, \cdots g_N\rangle \tag{7.2}$$

where N is the number of atoms in the ensemble and δ_j is the transition frequency of the j^{th} atom with respect to the input photon's carrier frequency, i.e. the detuning. z_j and c_j denote the position of the j^{th} atom within the medium and the excitation probability amplitude for each atom, respectively. Following the creation of the collective atomic excitation, the different components in Eq. 7.2 start accumulating different phases owing to different detunings δ_j of the excited ions. However, due to the discrete and periodic nature of the possible atomic transition frequencies, $\delta_j = m\,\Delta$ ($m \in \mathbb{Z}$), all phases automatically line up at time $\tau = 1/\Delta$, resulting in the re-emission of the photon in its original quantum state (see Fig. 7.2c). This memory for quantum light (with pre-programmed delay τ) can be turned into a quantum storage device with read-out on demand, i.e. allow mapping of a qubit in an arbitrary input mode onto a specific output mode, both in the temporal as well as spectral domain[13, 14]. Furthermore, under certain circumstances, the retrieval process can approach unit efficiency[3, 15]. The AFC protocol, implemented in rare-earth-ion doped crystals, has already shown great promise as a quantum memory for quantum information processing applications, including a retrieval fidelity exceeding 99.5%[16], an efficiency of 56%[17], more than 5 GHz bandwidth[18], the possibility to store a large number of temporal and spectral modes[19, 20, 14], recall on demand[16, 14], waveform preserving storage[21], and the possibilities to store members of entangled photon pairs[18, 22] plus teleport pho-

tonic quantum states into crystals[23].

Finally, to analyze the joint state of the photon pairs before and after storage of the 1532 nm photon, we perform individual projection measurements onto certain time-bin qubit states

$$|\psi\rangle = \alpha\,|e\rangle + \beta e^{i\theta}\,|l\rangle\,, \qquad \alpha^2 + \beta^2 = 1. \tag{7.3}$$

The measurements are henceforward also referred to as projections onto eigenstates of the Pauli operators σ_x (corresponding to projections onto $(|e\rangle \pm |l\rangle)/\sqrt{2}$), σ_y (corresponding to projections onto $(|e\rangle \pm i\,|l\rangle)/\sqrt{2}$), σ_z (corresponding to projections onto $|e\rangle$ and $|l\rangle$), and superpositions of σ_x, σ_y and σ_z.

a) Photon pair source (see also Fig. 7.1b). A mode-locked laser emits, with 80 MHz repetition rate, 6 ps-long pulses at 1047 nm wavelength. The pules are frequency doubled by means of second harmonic generation (SHG) in a periodically poled lithium niobate (PPLN) crystal, and are directed to an imbalanced Mach-Zender interferometer (MZI) that splits each pulse into two, separated by 1.4 ns. Spontaneous parametric down conversion in a PPLN crystal yields time-bin entangled photon pairs with members centered at 795 nm and 1532 nm wavelength. Remaining 523 nm light is removed through filters (not shown), the photons from each pair are separated using a dichroic mirror, and their bandwidths are reduced to approximately 6 GHz and 10 GHz by means of a Fabry-Perot cavity (for the 795 nm photon), and a fibre Bragg grating (for the 1532 nm photon), respectively, to allow storage of the 1532 nm photon in the erbium-doped fibre. In addition, the filtering creates entangled pairs that are suitable for quantum teleportation, and, furthermore, would allow storing the 795 nm photon in our Tm:$LiNbO_3$ quantum memory[18].

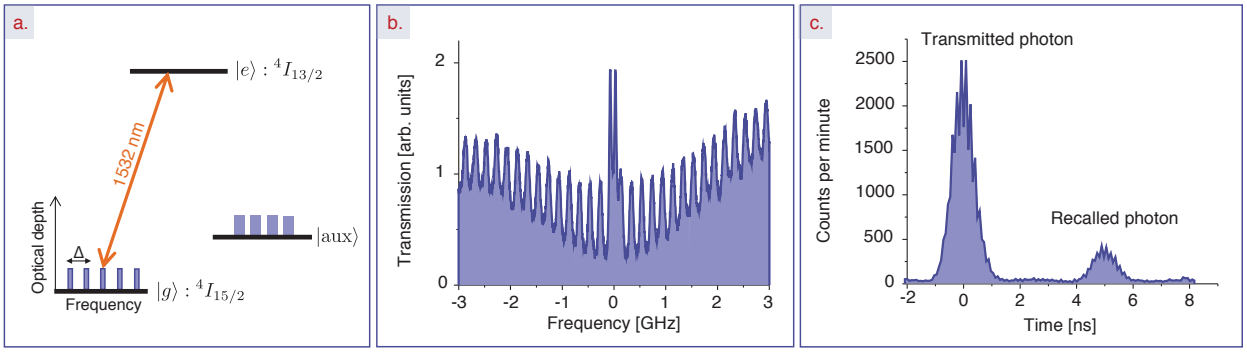

Figure 7.2: **Storage of telecom-wavelength photons in a broadband AFC memory. a) Simplified erbium level scheme.** To generate AFCs, we frequency-selectively transfer population from the ${}^4I_{15/2}$ electronic ground state ($|g\rangle$) through the ${}^4I_{13/2}$ excited state ($|e\rangle$) into an auxiliary state ($|aux\rangle$). **b) Typical atomic frequency comb.** The total AFC bandwidth is 8 GHz (only 6 GHz are shown), and the peak spacing 200 MHz, leading to 5 ns-long storage. The variation of the AFC's envelope is an artifact. **c) Photon storage.** 1532 nm wavelength photons in a single temporal mode are stored and retrieved after 5 ns with ∼1% efficiency (for more details see the Supplementary Information), and detected by an SNSPD. Also shown are detections due to directly transmitted (i.e. not absorbed) photons. The detection-time jitter of the detector used for this measurement is around 800 ps, which restricts one from observing the true duration of the original and re-emitted photons (around 44 and 55 ps, respectively).

b) Analyzers (see also Fig. 7.1c). The quantum states of the 795 and 1532 nm photons are projected onto time-bin qubit states spanned by two, 1.4 ns-separated temporal modes: we employ either MZIs featuring path-lengths differences of 1.4 ns followed by single photon detectors (SPDs) (allowing projections onto $|\varphi\rangle = (|e\rangle + e^{i\varphi}|l\rangle)/\sqrt{2}$), or a delay line followed by an SPD (allowing projections onto $|e\rangle$ and $|l\rangle$, not shown). The SPDs for the 795 nm photons are based on silicon avalanche photo diodes and feature detection efficiencies around 60% and dark counts around 100 Hz, and the 1532 nm photons are detected using superconducting nano-wire single photon detectors (SNSPDs) with efficiency around 90% and dark counts around 10 Hz [[24]] (see the Supplementary Information for more details). A coincidence unit and a PC allow assessing the rates with which certain combination of projections occur, e.g. the rate with which the 795 nm photon is projected onto $|e\rangle$ and the

1532 nm photon is projected onto $(|e\rangle + |l\rangle)/\sqrt{2}$.

c) Quantum memory (see also Fig. 7.1d). The light from an extended-cavity continuous wave (CW) laser at 1532 nm wavelength is frequency and intensity modulated using a phase modulator and acousto-optic modulator (AOM), respectively. After passing a switch and a circulator, it is sent into the erbium-doped fibre, which is exposed to a ∼600 Gauss magnetic field to split erbium energy levels into magnetic sub levels (see Fig. 7.2a). Erbium-light interaction then leads to frequency-selective persistent spectral hole burning with hole life times up to 10 seconds (more information will be published elsewhere[25]) and, after repetition of the burning sequence during 400 ms, to an 8 GHz wide atomic frequency comb (see Fig. 7.2b; for additional details see the Supplementary Information). After spectral tailoring, we wait 300 ms before storing and retrieving entangled photons – this is necessary to allow excited atoms to decay, i.e. ensure that recalled photons are not masked by spontaneously emitted photons. To remove the light used for spectral hole burning during waiting and photon storage (700 ms during each experimental cycle), the position of the switch is toggled.

7.3 Measurements and Results

To experimentally demonstrate our memory's ability to preserve entanglement, we perform a set of projection measurements (see the Methods section) that allows reconstructing the quantum state of the photon pairs before storage in terms of its density matrix using a maximum likelihood method[26]. We then repeat the same measurements after having stored and retrieved the 1532 nm photon. The resulting matrices are shown in Figure 7.3, and table 7.1 lists various parameters that quantify relevant properties of the two-photon system for each case.

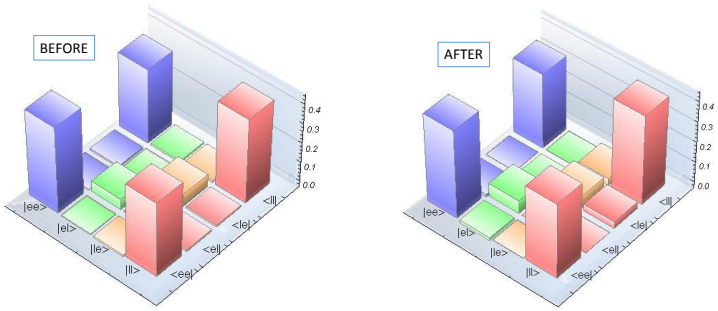

Figure 7.3: **Reconstructed density matrices.** The figure shows the measured density matrices of the photon pairs before (in) and after (out) storage of the telecom photon. Only the real components are shown – the absolute values of all imaginary components are below 0.025.

The first parameter of interest is the fidelity, which quantifies the overlap between two quantum states. We find that the fidelities of the photon pair states before and after storage with respect to the maximally entangled $|\phi^+\rangle$-state given in Eq. 7.1 are 0.825±0.004 and 0.808 ±0.048, respectively. Furthermore, we calculate the purity of the photon pair states before and after storage, yielding 0.694 ± 0.007 and 0.673 ± 0.047, respectively. The deviation from the optimum value of one in all cases (i.e. concerning the fidelity and the purity) is due to SPDC not creating individual photon pairs, but rather a distribution over even numbers of photons. However, we note that the two measured fidelities, as well as both purities, are equal to within the statistical uncertainty, suggesting that the state has not been altered during storage. To verify this conjecture, we also calculate the input-output fidelity of the quantum state after storage with respect to the state before storage. We find $F_{\mathrm{in/out}}$= 0.971 ±0.049, confirming that the state did indeed not change.

Another important parameter is the entanglement of formation E_F, which we use to quan-

tify the amount of entanglement in our photon pairs. (Values for E_F range from zero for a separable state to one for a maximally entangled state.) We find E_F=0.531 ±0.011 before storage and, similarly, 0.499 ±0.105 after storage. This reflects that the state does not change during storage, and furthermore shows that it is — and remains — entangled.

In addition to the tomographic reconstruction, we also perform a Clauser–Horne–Shimony–Holt (CHSH) Bell-inequality test[27] before and after storage. This test reveals whether or not the correlations between outcomes of measurements on a bi-partite system can be explained by local realistic theories (LRT). Assuming local realistic theories, CHSH derived that

$$S = |E(\boldsymbol{a},\boldsymbol{b}) - E(\boldsymbol{a},\boldsymbol{b'}) + E(\boldsymbol{a'},\boldsymbol{b}) + E(\boldsymbol{a'},\boldsymbol{b'})| \tag{7.4}$$

has an upper bound of two:

$$S_{\mathrm{LRT}} \leq 2, \tag{7.5}$$

while quantum mechanics predicts a maximum value of $S_{\mathrm{QM}}^{\mathrm{max}} = 2\sqrt{2} \approx 2.82$. Here, $E(\boldsymbol{x},\boldsymbol{y})$ is the correlation coefficient measured when projecting particle one (i.e. the 795 nm photon) onto $|x\rangle$, and particle two (i.e. the 1532 nm photon) onto $|y\rangle$. For more details see the Methods section and the Supplementary Information. Before storage, we find S_{in}= 2.38 ±0.05, and, crucially, S_{out}= 2.33 ±0.22 after storage (see Table 7.1). Hence, we find a violation of the maximum value allowed by local realistic theories by 7.5 and 1.5 standard deviations, respectively.

a) Density matrices. To analyze the bi-photon states, we perform joint-projection measurements with the 795 nm and the 1532 nm photons onto time-bin qubit states characterized by $\boldsymbol{a}$, $\boldsymbol{b}$, respectively, where $\boldsymbol{a},\boldsymbol{b} \in [\pm\sigma_x, \pm\sigma_y, \pm\sigma_z]$. This is done by means of suitably adjusted qubit analyzers, and by counting the number $C(\boldsymbol{a},\boldsymbol{b})$ of detected photon pairs per

Quantity	Before storage	After storage
Fidelity with $\|\phi^+\rangle$ (%)	82.5±0.4	80.8 ±4.8
Purity (%)	69.4 ± 0.7	67.3 ±4.7
Input/Output fidelity (%)	97.1 ±4.9	
Entanglement of formation (%)	53.1 ±1.1	49.9 ±10.5
Expected S_{th}	2.39 ±0.01	2.35 ±0.10
Measured S	2.38 ±0.05	2.33 ±0.22

Table 7.1: **Characterization of the two-photon state.** Using reconstructed and ideal density matrices, we calculate the fidelity of our two-photon state before and after storage with the maximally entangled $|\phi^+\rangle$-state, its purity, the fidelity of ρ_{out} with respect to ρ_{in}, and the entanglement of formation. The table also shows expected and experimentally obtained values for tests of the CHSH Bell inequality. Uncertainties (one standard deviation) are estimated from Poissonian detection statistics using Monte Carlo simulation. For more details see the Supplementary Information.

time. Recall that, for time-bin quits, projecting a photon's state onto $\pm\sigma_z$ corresponds to detecting the photon in an early or late time bin, respectively, while projections onto $\pm\sigma_x$, $\pm\sigma_y$ and any linear combinations of these correspond to detecting the photon in a specific output of a widely unbalanced interferometer with appropriately set phase. The phases of the three interferometers (one in the photon pair source plus one per analyzer) are individually locked using a frequency-stabilized laser (not shown in Fig.**??**) and adjusted using a procedure described previously[21].

From two joint projection measurement, we calculate the normalized joint-detection probability

$$P(\boldsymbol{a},\boldsymbol{b}) = \frac{C(\boldsymbol{a},\boldsymbol{b})}{C(\boldsymbol{a},\boldsymbol{b}) + C(\boldsymbol{a},-\boldsymbol{b})} \tag{7.6}$$

where $\boldsymbol{b}$ and $-\boldsymbol{b}$ refer to projections onto orthogonal states. The values of nine different joint-detection probabilities (stemming from all combinations of $\boldsymbol{a},\boldsymbol{b} \in [\sigma_x, \sigma_y, \sigma_z]$) allow constructing the density matrices for our bi-partite quantum system[26] (see Figure 7.3).

b) Bell inequality. To test the CHSH-Bell-inequality, we perform four sets of measurements, each consisting of four joint measurements with projections onto any combination of $\pm\boldsymbol{a}$ (measured on one particle) and $\pm\boldsymbol{b}$ (measured on the other particle), respectively, where $\boldsymbol{a}\otimes\boldsymbol{b} \in [\sigma_y\otimes(\sigma_x+\sigma_y), \sigma_y\otimes(\sigma_x-\sigma_y), \sigma_x\otimes(\sigma_x+\sigma_y), \sigma_x\otimes(\sigma_x-\sigma_y)]$ (the chosen settings allow violating the CHSH-Bell inequality maximally). For each set, we calculate the correlation coefficient

$$E(\boldsymbol{a},\boldsymbol{b}) = \frac{C(\boldsymbol{a},\boldsymbol{b}) - C(\boldsymbol{a},-\boldsymbol{b}) - C(-\boldsymbol{a},\boldsymbol{b}) + C(-\boldsymbol{a},-\boldsymbol{b})}{C(\boldsymbol{a},\boldsymbol{b}) + C(\boldsymbol{a},-\boldsymbol{b}) + C(-\boldsymbol{a},\boldsymbol{b}) + C(-\boldsymbol{a},-\boldsymbol{b})}, \tag{7.7}$$

which, in turn, allows calculating S according to Eq. 7.4.

7.4 Conclusion and Discussion

Our results show that photon-photon entanglement can be reversibly mapped onto entanglement between a photon and a collective atomic excitation that is delocalized over $\sim 10^{13}$ erbium atoms spread over twenty meters. Being based on the same material as a classical erbium fibre amplifier, our memory is the first to store non-classical states of light at telecom wavelength, and, furthermore, it is the first quantum memory that employs light-atom interaction in an optical fibre. We note that the ease of integration into fibre networks, and its large time-bandwidth product and multimode storage capacity make our light-matter interface attractive for quantum information processing tasks in addition to storage[28]. Furthermore, erbium-based memories may allow interfacing telecommunication photons with superconducting qubits[29].

From a more fundamental point of view, as the length of our atomic medium exceeds the pulse length of the light that the absorbers collectively interact with, our results open the path towards a new kind of cavity QED-type experiments[30]. In addition, they raise the

interesting question of whether there is an upper limit to the separation between atomic absorbers — e.g. the light's wavelength[31] — after which the entanglement inherent in Eq. 7.2 breaks down. This decoherence would manifest itself as an unusual decrease of storage efficiency. While our demonstration falls short to answer this question (the average distance was around 10 nm, i.e. $\sim \lambda/100$), the possibility to use impurity-doped optical fibres opens the path towards kilometre-long, very weakly doped memory materials with large inter-dopand separation, i.e. the possibility for an experimental test. We anticipate that our investigation will benefit the realization of quantum networks, and also trigger more fundamental research towards improved understanding of light-matter interaction in glassy hosts, and collective atomic effects in unconventional materials.

Bibliography

[1] Kimble, H. J. The quantum Internet. *Nature* **453**, 1023-1030 (2008).

[2] Lvovsky, A. I., Tittel, W. & Sanders, B. C. Optical quantum memory. *Nature Photon.* **3**, 706-714 (2009).

[3] Ladd, T. D. et al. Quantum computers. *Nature* **464**, 45-53 (2010)

[4] Gisin, N., Ribordy, G., Tittel, W. $ Zbinden, H. Quantum cryptography. *Rev. Mod. Phys.* **74** (2002).

[5] Giovannetti, V., Lloyd, S. & Maccone, L. Advances in quantum metrology. *Nature Photon.* **5**, 222–229 (2011)

[6] Sangouard, N., Simon, C., de Riedmatten, H., & Gisin, N. Quantum repeaters based on atomic ensembles and linear Optics. *Rev. Mod. Phys.* **83**, 1:3380 (2011).

[7] Bussières, F. et al. Prospective applications of optical quantum memories. *J. Mod. Opt.* **60**, 1519-1537 (2013).

[8] Lauritzen B. et al. Telecom-wavelength solid-state memory at the single photon level *Phys. Rev. Lett.* **104,** 080502 (2010)

[9] Dajczgewand, J., Le Gouët J. L., Louchet-Chauvet, A. & Chanelière, T. Large efficiency at telecom wavelength for optical quantum memories. *Opt. Lett.* **39**, 9, 2711-2714 (2014)

[10] Sprague, M. R. et al. Broadband single-photon-level memory in a hollow-core photonic crystal fibre. *Nature Photon.* **8**, 287–291 (2014).

[11] de Riedmatten, H., Afzelius, M., Staudt, M. U., Simon, C. & Gisin, N. A solid-state light matter interface at the single-photon level. *Nature* **456**, 773 (2008).

[12] Afzelius, M., Simon, C., de Riedmatten, H. & Gisin, N. Multimode quantum memory based on atomic frequency combs *Phys. Rev. A* **79** 052329 (2009).

[13] Afzelius, M. et al. Demonstration of atomic frequency comb memory for light with spin-wave storage. *Phys. Rev. Lett.* **104**, 040503 (2010).

[14] Sinclair, N. et al. A solid-state memory for multiplexed quantum states of light with read-out on demand. arXiv:1309.3202v1 [quant-ph] (2013).

[15] Afzelius, M., & Simon, C. Impedance-matched cavity quantum memory, *Phys. Rev. A* **82**, 022310 (2010).

[16] Zhou Z-Q., Lin W-B., Yang M, Li C-F., and Guo G-C., Realization of reliable solid-state quantum memory for photonic polarization qubit. *Phys. Rev. Let.* **108,** 190505 (2012).

[17] Sabooni, M., Li, Q., Kröll, S., and Rippe, L. Efficient quantum memory using a weakly absorbing sample *Phys. Rev. Lett.* **110**, 133604 (2013).

[18] Saglamyurek, E. et al. Broadband waveguide quantum memory for entangled photons. *Nature* **469**, 513-518 (2011).

[19] Usmani, I., Afzelius, M., de Riedmatten, H., & Gisin, N. Mapping multiple photonic qubits into and out of a solid-state atomic ensemble. *Nature Commun.* **1,** 12 (2010).

[20] Bonarota, M., Le Gouët, J. L. & Chanelière, T. Highly multimode storage in a crystal *New J. Phys.* **13**, 013013 (2010).

[21] Jin, J. et al. Two-photon interference of weak coherent laser pulses recalled from separate solid-state quantum memories. *Nature Commun.* **4**, 2386 (2013).

[22] Clausen, C. et al. Quantum storage of photonic entanglement in a crystal. *Nature* **469,** 508-512 (2011).

[23] Bussières, F. et al. Quantum teleportation from a telecom-wavelength photon to a solid-state quantum memory. arXiv:1401.6958v1 [quant-ph] (2014).

[24] Marsili F. et al. Detecting single infrared photons with 93 % system efficiency. *Nature Photon.* **7**, 210-214 (2013).

[25] Saglamyurek, E. et al. Investigations of persistent spectral hole burning in an erbium-doped silicate fibre for quantum information processing applications. *In preparation* (2014).

[26] Altepeter, J. B., Jeffrey, E. R., &. Kwiat, P. G. Photonic state tomography. *Adv. At. Mol. Opt. Phys.* **52**, 105–159 (2005).

[27] Clauser J. F., Horne M. A., Shimony A. & Holt, R. A. Proposed experiment to test local hidden-variable theories, *Phys. Rev. Lett.* **23**, 15,880 (1969).

[28] Saglamyurek, E. et al. An integrated processor for photonic quantum states using a broadband light-matter interface. *New J. Phys.* (accepted) (2014).

[29] O'Brien, C., Lauk, N., Blum, S., Morigi & G. Fleischhauer, M. Interfacing Superconducting qubits and telecom photons via a rare-earth doped crystal. arXiv:1402.5405v1 [quant-ph] (2014).

[30] Scully, M. O. & Svidzinsky, A. A. The Super of Superradiance. *Science* **325**, 1510 (2009).

[31] Dicke, R. H. Coherence in Spontaneous Radiation Processes. *Phys. Rev.* **93**, 99 (1954)

Chapter 8

Bell-State Measurement with Photons Recalled from Memories

The Bell-state measurement (BSM) is the key part of a quantum repeater as it entangles elementary links as explained in Chapter 1. Furthermore, the BSM is a crucial ingredient for scalable optical quantum computation and secure quantum communication protocols including the measurement-device-independent quantum key distribution protocol [1]. A BSM projects two partaking photons onto a maximally entangled two-photon state, i.e. *Bell* state. The BSM, as for all two-photon measurements, requires two independent photons that are indistinguishable in all their degrees of freedom, i.e. spatial, spectral, temporal, and polarization modes. A natural method for investigating the indistinguishabilty of two independent photons is to interfere them on a single beam splitter. The visibility of the ensuing two-photon interference, known as the Hong-Ou-Mandel (HOM) effect [2], quantifies the degree of indistinguishability of the two photons.

This Chapter describes two-photon measurements, i.e. two-photon interference and BSM, between single-photon level coherent light pulses recalled from separate quantum memories. As the obtained visibility of two-photon interference is near the theoretical maximum and within experimental errors the same whether or not the photons were stored in the quantum memory, we conclude that our solid-state quantum memories are capable of preserving the photonic wavefunction, in addition to quantum bits and entanglement. Moreover, this implementation has been done with two memories that experiences dissimilar magnetic fields, thus revealing the robustness of the applied quantum memory protocol, i.e. atomic frequency comb (AFC), against different environmental configurations. Furthermore, BSM is success-

fully performed between two time-bin qubits that are mapped into and out of our memories.

In this Chapter, the experiment was conducted in collaboration with Joshua A. Slater, Erhan Saglamyurek, Neil Sinclair and Daniel Oblak. Mathew George, Raimund Ricken and Wolfgang Sohler fabricated and investigated our memory material, i.e. Tm:$LiNbO_3$, at room temperature. Wolfgang Tittel conceived and directed the expeirment. I contributed to this study in the following stages : building the source of single-photon level coherent light, time-bin qubits and measurement setups, performing the measurements, analyzing the results, computing a theoretical expectation for a BSM visibility with time-bin qubits and for quantum storage fidelity, and writing the manuscript.

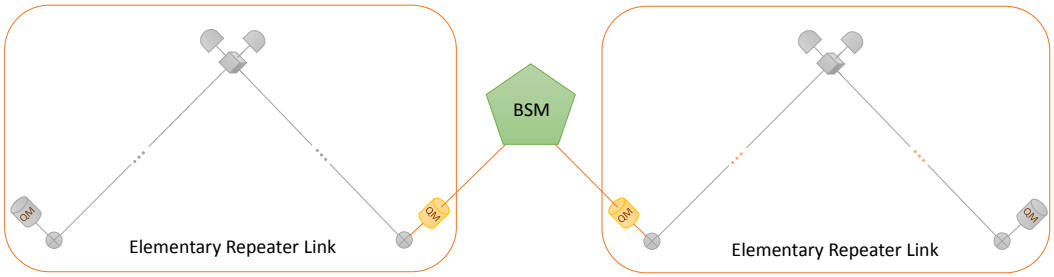

Figure 8.1: **Interconneting two elementary links of quantum repeater.** Two neighboring links are connected by means of Bell-state measurement between two photons, one from each link, recalled from quantum memories.

Nature Communications 4, 2386 (2013)

Two-photon Interference of Weak Coherent Laser Pulses Recalled From Separate Solid-state Quantum Memories

Jeongwan Jin[1], Erhan Saglamyurek[1], Neil Sinclair[1], Joshua A. Slater[1], Mathew George[2], Raimund Ricken[2], Daniel Oblak[1], Wolfgang Sohler[2], and Wolfgang Tittel[1]

[1]*Institute for Quantum Information Science, and Department of Physics and Astronomy, University of Calgary, 2500 University Drive NW, Calgary, Alberta T2N 1N4, Canada*

[2]*Department of Physics - Applied Physics, University of Paderborn, Warburger Str. 100, 33095 Paderborn, Germany*

Abstract

Quantum memories allowing reversible transfer of quantum states between light and matter are central to quantum repeaters, quantum networks, and linear optics quantum computing. Significant progress regarding the faithful transfer of quantum information has been reported in recent years. However, none of these demonstrations confirm that the re-emitted photons remain suitable for two-photon interference measurements, such as C-NOT gates and Bell-state measurements, which constitute another key ingredient for all aforementioned applications. Using pairs of laser pulses at the single-photon level, we demonstrate two-photon interference and Bell-state measurements after either none, one, or both pulses have been reversibly mapped to separate thulium-doped lithium niobate waveguides. As the interference is always near the theoretical maximum, we conclude that our solid-state quantum memories, in addition to faithfully mapping quantum information, also preserve the entire photonic wavefunction. Hence, our memories are generally suitable for future applications of quantum information processing that require two-photon interference.

8.1 Introduction

When two indistinguishable single photons impinge on a 50/50 beam-splitter (BS) from different input ports, they bunch and leave together by the same output port. This two-photon interference, named the Hong-Ou-Mandel (HOM) effect[**?**], is due to destructive interference between the probability amplitudes associated with both input photons being transmitted or both reflected, see Fig. 8.2. Since no such interference occurs for distinguishable input photons, the interference visibility V provides a convenient way to verify that two photons are indistinguishable in all degrees of freedom, i.e. spatial, temporal, spectral, and polarization modes.

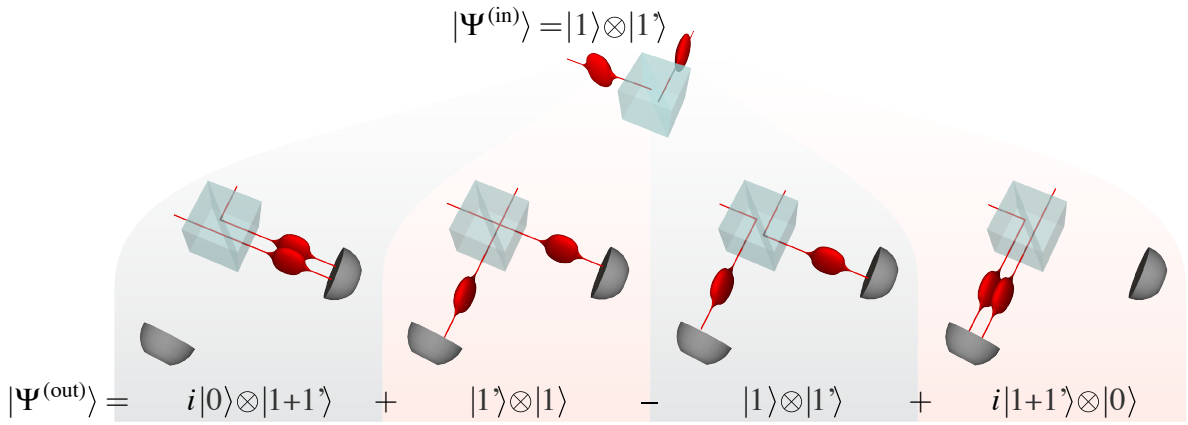

Figure 8.2: **Principle of HOM interference.** Illustration of HOM-interference in the case of single photons at BS input $|\psi^{(\mathrm{in})}\rangle = |1, 1'\rangle$, where the prime on the latter input indicates the possibility to distinguish that input photon from the other in some degree of freedom e.g. by being polarized orthogonally. The four possible paths of the photons are illustrated, together with their corresponding output states. If the input photons are indistinguishable with respect to all degrees of freedom we can ignore the primes in the output states and the paths shown in the two central pictures are identical and, due to the different signs, thus cancel. This leaves in the output state $|\psi^{(\mathrm{out})}\rangle$ only the possibilities in which photons bunch. For distinguishable photons, e.g. having orthogonal polarizations, all paths are distinguishable and all terms remain in $|\psi^{(\mathrm{out})}\rangle$.

The visibility is defined as

$$V = (\mathcal{R}_{\max} - \mathcal{R}_{\min})/\mathcal{R}_{\max}, \tag{8.1}$$

where $\mathcal{R}_{\min}$ and $\mathcal{R}_{\max}$ denote the rate with which photons are detected in the two output ports in coincidence if the incoming photons are indistinguishable and distinguishable, respectively. Consequently, the HOM effect has been employed to characterize the indistinguishability of photons emitted from a variety of sources, including parametric down-conversion crystals[3], trapped neutral atoms[4, 5], trapped ions[6], quantum dots[7, 8, 9], organic molecules[10], nitrogen-vacancy centres in diamond[11, 12], and atomic vapours[13, 14, 15, 16, 17]. Furthermore, two-photon interference is at the heart of linear optics Bell-state measurements[18], and, as such, has already enabled experimental quantum dense coding, quantum teleportation, and entanglement swapping[19]. In parallel, recent reports have shown notable progress in mapping light to and from atoms, e.g. demonstrating the faithful transfer of quantum information from photons in pure and entangled qubit states[20, 21, 22, 23, 5, 24]. However, to date, the possibility to perform Bell-state measurements with photons that have previously been stored in a quantum memory, as required for advanced applications of quantum information processing, has not yet been established. For these measurements to succeed, photons need to remain indistinguishable in all degrees of freedom, which is more restrictive than the faithful recall of quantum information encoded into a single degree of freedom. Indeed, taking into account that photons may or may not have been stored before the measurement, this criterion amounts to the requirement that a quantum memory preserves a photon's wavefunction during storage. Similar to the case of photon sources, the criterion of indistinguishability is best assessed using HOM interference, provided single-photon detectors are employed.

When using single photon Fock states at the memory inputs, the HOM visibility given in (8.1) theoretically reaches 100% as illustrated in Fig. 8.2. However, with phase randomized laser pulses obeying Poissonian photon-number statistics, as in our demonstration, the maximally achievable visibility is 50%[25], irrespective of the mean photon number (see Supplementary

Note 1). Nevertheless, attenuated laser pulses are perfectly suitable for assessing the effect of our quantum memories on the photonic wavefunction. Any reduction of indistinguishability due to storage causes a reduction of visibility, albeit from maximally 50%.

Here we demonstrate two-photon interference as well as a Bell-state measurement after either none, one, or both weak coherent pulses have been reversibly mapped to separate thulium-doped lithium niobate (Ti:Tm:$LiNbO_3$) waveguides using the atomic frequency comb (AFC) memory protocol[26, 21, 22]. The measured interference visibility is always near the theoretical maximum, which verifies that the reversible mapping of the pulses to our solid-state quantum memories preserves the entire photonic wavefunction. Thus we show that our memories are generally suitable for use in all quantum information processing applications that rely on two-photon interference[27, 28]. This approach extends the characterization of quantum memories using attenuated laser pulses[29] from assessing the preservation of quantum information during storage to assessing the preservation of the entire wavefunction, and from first- to second-order interference.

8.2 Experiment

Our experimental setup, depicted in Fig. 8.3, consists of two cryogenically cooled solid-state quantum memories, elements used to generate optical pulses (that either allow preparing, or probing the quantum memories), and devices used to analyze the probe pulses after storage. Light from a 795.43 nm wavelength CW laser passes through an acousto-optic modulator (AOM) driven by a sinusoidally varying signal. For the memory preparation we use the AOM's first negative diffraction order, which is fibre coupled into a phase modulator and, via a beam-splitter (BS), two polarization controllers (PCs) and two micro-electromechanical switches (MEMS), injected from the back into two Ti:Tm:$LiNbO_3$ waveguides (labelled A and B) cooled to 3 K [[30]]. Waveguide A is placed inside a superconducting solenoid. Using

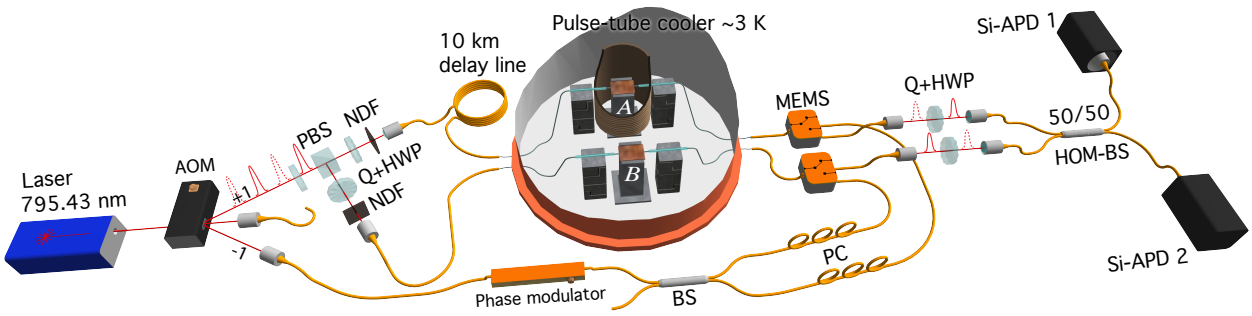

Figure 8.3: **Experimental setup.** We employ solid-state quantum memories, more precisely thulium-doped lithium-niobate waveguides, in conjunction with the atomic frequency comb (AFC) quantum memory protocol[26] (see Methods). Using an acousto-optic modulator (AOM) followed by a polarizing beam splitter (PBS) and a neutral density filter (NDF) we generate weak probe pulses that, after polarization adjustment by a quarter- and a half-wave plate (Q+HWP), are directed to our two memories. After passing through a set of micro electro-mechanical switches (MEMS) we interfere various combinations of recalled and non-stored (i.e. directly transmitted) pulses on a 50/50 BS (HOM-BS) and detect them on silicon avalanche-photo-diode (Si-APD) based detectors as described in the main text.

a linear frequency-chirping technique[21] we tailor AFCs with 600 MHz bandwidth and a few tens of MHz peak spacing, depending on the experiment, into the inhomogeneously broadened absorption spectrum of the thulium ions, as shown in Fig. 8.4. After 3 ms memory preparation time and 2 ms wait time we have a 3 ms period during which we store and recall many probe pulses. The 8 ns long probe pulses with $\approx$ 60 MHz Fourier-limited bandwidth are derived from the first positive diffraction order of the AOM output at a repetition rate of 2.5-3 MHz. Each pulse is divided into two spatial modes by a half-wave plate (HWP) followed by a polarizing beam-splitter (PBS). Pulses in both spatial modes are attenuated by neutral-density filters (NDFs) and coupled into optical fibres and injected from the front into the Ti:Tm:$LiNbO_3$ waveguides. After exiting the memories (i.e. either after storage or direct transmission), the pulses pass quarter- and half-wave plates used to control their polarizations at the 50/50 BS (HOM-BS) where the two-photon interference occurs.

Note that, to avoid first-order interference, pulses passing through memory A propagate through a 10 km fibre to delay them with respect to the pulses passing through memory B

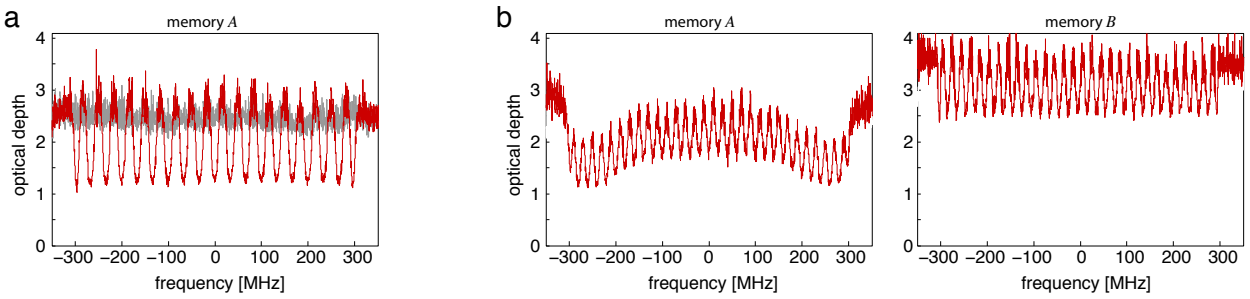

Figure 8.4: **Absorption spectra of quantum memories.** Measured absorption spectra of atomic frequency combs (AFCs) prepared in Ti:Tm:$LiNbO_3$ waveguides using frequency selective optical pumping for the (a) single-memory and (b) two-memory configurations (red traces). The light grey trace in (a) shows the optical depth when the memory is inactive, i.e. no AFC is prepared. The AFC bandwidths are set to 600 MHz, which is much wider than that of the stored pulses (about 60 MHz). The AFC peak spacing in (a) is $\Delta = 33$ MHz and in (b) $\Delta = 20$ MHz yielding storage times of $1/\Delta = 30$ ns and 50 ns, respectively. In the depicted AFC for the single memory configuration (a), a 133 Gauss magnetic field is applied along the c-axis of crystal A – located inside the magnet solenoid (see Fig. 8.3) – causing the excited and ground states to split into two long-lived nuclear Zeeman sub-levels. The resulting splitting difference of $\Delta/2 \approx 17$ MHz gives the optimal memory efficiency. In the two-memory configuration (b) it is important to note that memory B is located outside the solenoid and thus experiences a different field than memory A. To obtain recall efficiencies that are reasonably similar, at the expense of being non-optimal, we set the magnetic field at memory A to 900 G (see Methods).

by more than the laser coherence length, thus randomizing the mutual phase between pulses from the two memories. Finally, pulses are detected by two single-photon detectors (actively quenched silicon avalanche photodiodes, Si-APDs) placed at the outputs of the beam-splitter, and coincidence detection events are analyzed with a time-to-digital convertor (TDC) and a computer.

8.3 Measurement and Results

We first deactivate both quantum memories (see Methods) to examine the interference between directly transmitted pulses, and thereby establish a reference visibility for our experimental setup. We set the mean photon number per pulse before the memories to 0.6, i.e. to the single-photon level. Using the wave plates, we rotate the polarizations of the pulses at the two HOM-BS inputs to be parallel (indistinguishable) or orthogonal (distinguishable) and in both cases record the coincidence detection rates of the detectors at the HOM-BS outputs. Employing (8.1) we find a visibility of $(47.9 \pm 3.1)\%$.

Subsequently, we activate memory A while keeping memory B off, and adjust the timing of the pulse preparation so as to interfere a recalled pulse from the active memory with a directly transmitted pulse from the inactive memory (see Methods). Pulses are stored for 30 ns in memory A prepared with the AFC shown in Fig. 8.4a, and the mean photon number per pulse at the quantum memory input is 0.6. Taking the limited storage efficiency of $\approx 1.5\%$ and coupling loss into account, this results in 3.4×10^{-4} photons per pulse at the HOM-BS inputs. As before, changing the pulse polarizations from mutually parallel to orthogonal, we find $V = (47.7 \pm 5.4)\%$, which equals our reference value within the measurement uncertainties.

As the final step, we activate both memories to test the feasibility of two-photon interference

in a quantum-repeater scenario. We note that in a real-world implementation, memories belonging to different network nodes are not necessarily identical in terms of material properties and environment. This is captured by our setup where the two Ti:Tm:$LiNbO_3$ waveguides feature different optical depths and experience different magnetic fields (see Fig. 8.4b and Methods). To balance the ensuing difference in memory efficiency we set the mean photon number per pulse before the less efficient and more efficient memories to 4.6 and 0.6, respectively, so that, as before, the mean photon numbers are 3.4×10^{-4} at both HOM-BS inputs. With the storage time of both memories set to 30 ns, we find $V = (47.2 \pm 3.4)\%$, in excellent agreement with the values from the previous measurements. The consistently high visibilities, compiled in the first column of Table 8.1, hence confirm that our storage devices do not introduce any degradation of photon indistinguishability during the reversible mapping process, and that two-photon interference is feasible with photons recalled from separate quantum memories, even if the memories are not identical.

Storage	Single-photon level	Few-photon level		
configuration	Polarization	Polarization	Temporal	Spectral
No-storage	$(47.9 \pm 3.1)\%$	$(51.0 \pm 5.6)\%$	$(42.4 \pm 2.3)\%$	$(43.7 \pm 1.7)\%$
Single-storage	$(47.7 \pm 5.4)\%$	$(55.5 \pm 4.1)\%$	$(47.6 \pm 3.0)\%$	$(42.4 \pm 3.5)\%$
Double-storage	$(47.2 \pm 3.4)\%$	$(53.1 \pm 5.3)\%$	$(46.1 \pm 3.2)\%$	N. A.

Table 8.1: Experimental two-photon interference visibilities for different degrees of freedom

We now investigate in greater detail the change in coincidence count rates as photons gradually change from being mutually indistinguishable to completely distinguishable with respect to each degree of freedom accessible for change in single-mode fibres, i.e. polarization, temporal, and spectral modes (see Methods). To acquire data more efficiently we increase the mean number of photons per pulse at the memory input to between 10 and 50 (referred to as few-photon-level measurements). However, the mean photon number at the HOM-BS remains below one. Example data plots are shown in Fig. 8.5, while the complete set of plots

is supplied in Supplementary Figures S1-S3.

In Fig. 8.5a we show the coincidence counts rates as a function of the polarization of the recalled pulse for the case of one active memory. The visibilities for all configurations (i.e. zero, one, or two active memories) extracted from fits to the experimental data are listed in column 2 of Table 8.1. They are – as in the case of single-photon-level inputs – equal to within the experimental uncertainty.

Next, in Fig. 8.5b, we depict the coincidence count rates as a function of the temporal overlap (adjusted by the timing of the pulse generation) for the two-memory configuration. Column 3 of Table 8.1 shows the visibilities extracted from Gaussian fits to the data, reflecting the temporal profiles of the probe pulses, for all configurations. Within experimental uncertainty, they are equal to each other. Alternatively, in the single-memory configuration, we also change the temporal mode overlap by adjusting the storage time of the pulse mapped to the quantum memory. Again the measured visibility of $V = (44.4 \pm 6.9)\%$ (see Fig. 8.5c) is close to the theoretical maximum.

Finally, we vary the frequency difference between the two pulses to witness two-photon interference with respect to spectral distinguishability. For this measurement, we consider only the configurations in which neither, or a single memory is active. In both cases the visibilities, listed in the last column of Table 8.1, are around 43%. While this is below the visibilities found previously, for reasons discussed in the Supplementary Note 2, the key observation is that the quantum memory does not affect the visibility. We have now demonstrated several experiments that consistently yield high two-photon interference visibilities, however we wish to point out that the two-photon interference visibility *can* be substantially reduced by imperfect preparation or operation of our quantum memory. This is further discussed in the

Supplementary Note 3.

As stated in the introduction, Bell-state measurements (BSM) with photonic qubits recalled from separate quantum memories are key ingredients for future applications of quantum communication. To demonstrate this important element, we consider the asymmetric (and arguably least favourable) configuration in which only one of the qubits is stored and recalled.

Appropriately driving the AOM in Fig. 8.3, we alternately prepare the states $|\Psi_a\rangle$ and $|\Psi_b\rangle$, which describe time-bin qubits[19] of the form $\cos(\frac{\theta_k}{2})\,|e\rangle + e^{i\phi_k}\sin(\frac{\theta_k}{2})\,|l\rangle$, where e and l, respectively, label photons in early or late temporal modes, which are separated by 25 ns. The parameter θ_k determines the relative amplitude of and ϕ_k the relative phase between the two temporal modes composing the time-bin qubit for $k = a, b$. The qubits are directed to the memories of which only one is activated. The mean photon number of the qubit that is stored is set to 0.6, yielding a mean photon number of both qubits at the HOM-BS input of 6.7×10^{-4}. We ensure to overlap pulses encoding the states $|\Psi_a\rangle$ and $|\Psi_b\rangle$ at the HOM-BS and count coincidence detections that correspond to a projection onto the $|\psi^-\rangle = \frac{1}{\sqrt{2}}(|e\rangle\,|l\rangle - |l\rangle\,|e\rangle)$ Bell state. This projection occurs if the two detectors click with 25 ns time difference[19]. The count rate $\mathcal{R}$ of the projection can be generalized for any given states of two incoming time-bin qubits as (see Supplementary Note 4)

$$\mathcal{R}(\theta_a, \phi_a, \theta_b, \phi_b) \propto \frac{\mu^2 e^{-2\mu}}{8}\left[4\sin^2\left(\frac{\theta_a + \theta_b}{2}\right) + \sin^2\big(\theta_a\big) + \sin^2\big(\theta_b\big) - 2\sin\big(\theta_a\big)\sin\big(\theta_b\big)\Big(1 + \cos\big(\phi_a - \phi_b\big)\Big)\right], \tag{8.2}$$

where we assume equal mean photon numbers μ at the two HOM-BS inputs.

Because $|\psi^-\rangle$ is antisymmetric with respect to any basis, the count rate is expected to reach a minimum value $\mathcal{R}_\parallel$ if the two input pulses are prepared in equal states ($\langle\Psi_a|\Psi_b\rangle = 1$), and a maximum value $\mathcal{R}_\perp$ if prepared in orthogonal states ($\langle\Psi_a|\Psi_b\rangle = 0$). Accordingly, we define

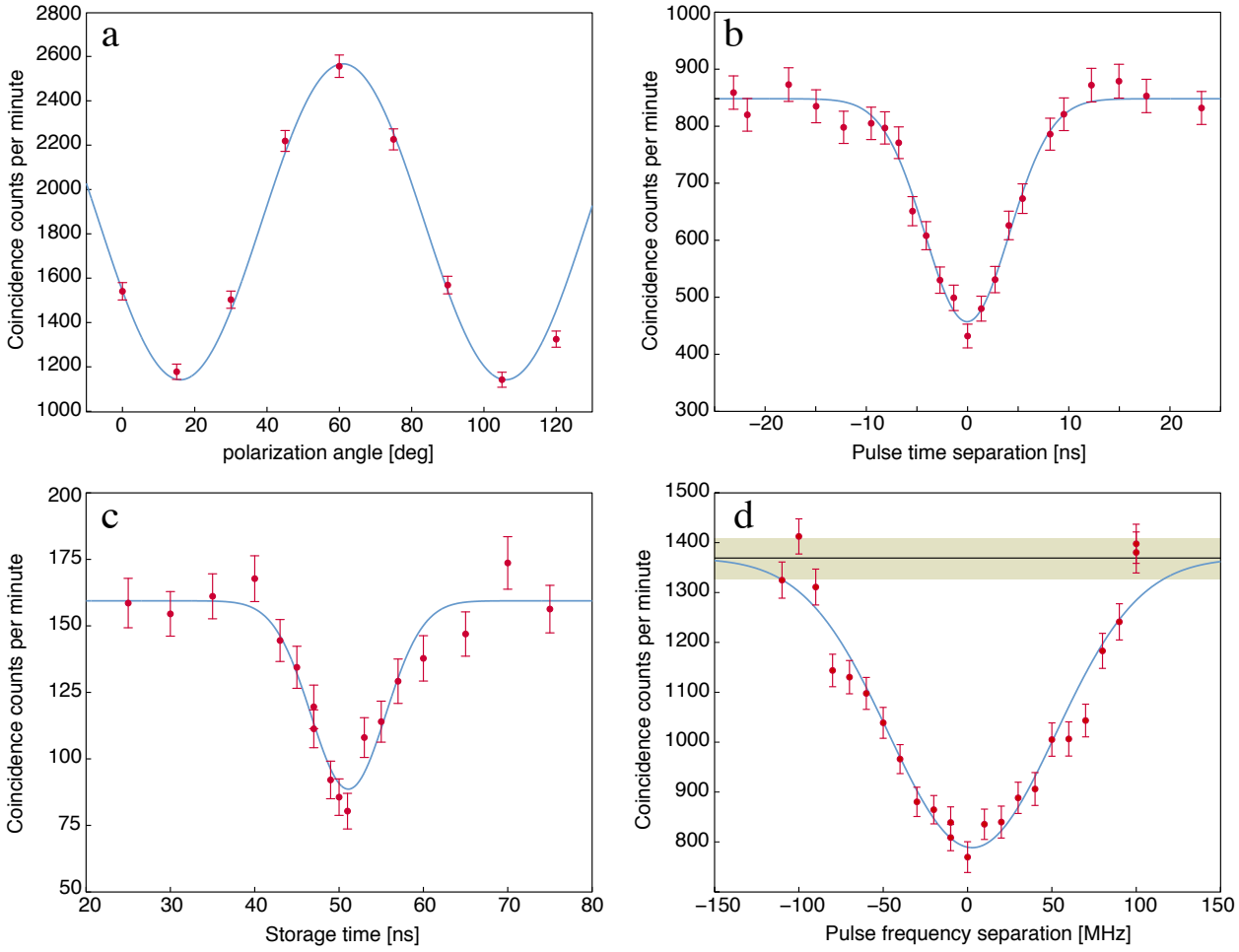

Figure 8.5: **Examples of measured HOM interference.** HOM interference plot examples for one or two active memory configurations. a) Varying mutual polarization difference with one active memory and 30 ns storage time. b) Varying temporal overlap by changing timing of pulse generation with two active memories and 50 ns storage time. c) Varying temporal overlap by changing storage time of one active quantum memory from 25-75 ns. d) Varying spectral overlap for one active quantum memory and 50 ns storage time. Due to the limited frequency tuning range of our AOM we determine a reference level by additionally making the pulse polarizations orthogonal. The resulting count rate is shown with the black line and error band in dark yellow. All error bars are calculated – assuming Poissonian counting statistics – as the square-root of the total counts. Some additional scattering is due to intensity fluctuations at the HOM-BS inputs, which can not be normalized away using the counts from the individual detectors due to the manifestation of the HOM interference in these counts (see Supplementary Note 5). The data in a) is fitted to a sinus function. The data in b),c),d) are fitted to a Gaussian function. The acquisition time per data point is 60 s in a),b),d) and 120 s in c).

an error rate that quantifies the deviation of the minimum count rate from its ideal value of zero:

$$e \equiv \frac{\mathcal{R}^{\parallel}}{\mathcal{R}^{\parallel} + \mathcal{R}^{\perp}} \,. \tag{8.3}$$

We now consider two important cases for which we will compute the error rates both in theory and from our experiment.

For qubits with $\phi_a = \phi_b = 0$ (i.e. encoded onto the xz-plane of the Bloch sphere) we are interested in the rate $\mathcal{R}^{\parallel}$ for the case in which the input qubits are parallel ($\theta_a = \theta_b$) and $\mathcal{R}^{\perp}$ for the case in which the input qubit states are orthogonal ($\theta_a = \theta_b - \pi$). Specifically, when we prepare two qubits (one at each input of the BS) in state $|e\rangle$, or two qubits in state $|l\rangle$, we expect $\mathcal{R}^{\parallel} = 0$ from the expression given in the (8.2). The count rate for observing a projection onto $|\psi\rangle$ increases as we change θ_a (or θ_b), and reaches a maximum $\mathcal{R}^{\perp}$ if one qubit is in state $|e\rangle$ and the other one in $|l\rangle$. Hence, using the expression for the error rate from (8.3), we find $e_{e/l}^{(\mathrm{att})} = 0$, where the superscript (att) indicates that this result applies to attenuated laser pulses. We now turn to measuring the coincidence rates for all combinations of $|e\rangle$ and $|l\rangle$ input states, thus extracting $\mathcal{R}^{\parallel}$ and $\mathcal{R}^{\perp}$, using 0.6 photons per qubit at the memory input. More precisely, we prepare the input qubit state $|e\rangle_a \otimes |e\rangle_b$ to measure $\mathcal{R}^{\parallel(1)}$ and then $|e\rangle_a \otimes |l\rangle_b$ to measure $\mathcal{R}^{\perp(1)}$. Subsequently, we prepare the input qubit state $|l\rangle_a \otimes |l\rangle_b$ to measure $\mathcal{R}^{\parallel(2)}$ and then $|l\rangle_a \otimes |e\rangle_b$ to measure $\mathcal{R}^{\perp(2)}$. These yield the average values $\mathcal{R}^{\parallel} = (\mathcal{R}^{\parallel(1)} + \mathcal{R}^{\parallel(2)})/2$ and $\mathcal{R}^{\perp} = (\mathcal{R}^{\perp(1)} + \mathcal{R}^{\perp(2)})/2$, from which we compute the experimental error rate $e_{e/l}^{(\mathrm{exp})} = 0.039 \pm 0.037$, which is near the theoretical value of $e_{e/l}^{(\mathrm{att})} = 0$.

Next, we consider the case in which two input qubits are in equal superpositions of early and late bins, $|+\rangle \equiv \frac{1}{\sqrt{2}}(|e\rangle + |l\rangle)$ and $|-\rangle \equiv \frac{1}{\sqrt{2}}(|e\rangle - |l\rangle)$, that is on the xy-plane of the Bloch sphere ($\theta_a = \theta_b = \pi/2$). Using (8.2), we find that the $|\psi^-\rangle$ Bell-state projection count rate

is smallest – but nonzero – when $\phi_a - \phi_b = 0$, i.e. the qubit states are parallel, and largest when the phases differ by π, i.e. the qubit states are orthogonal. Inserting the respective values for $\mathcal{R}^{\parallel}$ and $\mathcal{R}^{\perp}$ into (8.3) results in an expected error rate of $e_{+/-}^{(\mathrm{att})} = 0.25$. Using again 0.6 photons per qubit, we measure the coincidence counts for $\phi_a - \phi_b = 0$ and π, giving us $R^{\parallel}$ and $R^{\perp}$, respectively. From these we get an experimental error rate of $e_{+/-}^{(\mathrm{exp})} = 0.287 \pm 0.020$, which is slightly above the theoretical bound. This indicates that either the measurement suffers from imperfections such as detector noise, or the modes at the BS are not completely indistinguishable, which, in turn, could be due to imperfectly generated qubit states or imperfect storage of the qubit in the quantum memory. In the following we will use the measured error rates to asses our quantum memory and thus make the most conservative assumption that the entire differences between the expected and measured values for the error rates are due to the memory fidelity being less than one.

As a first step we derive lower bounds for the error rates when the best-known classical storage strategy is applied, and then compare it to the outcomes of our Bell-state measurements. In order to accommodate this scenario we suppose that the memory performs the following operation $|\psi\rangle\langle\psi| \to F|\psi\rangle\langle\psi| + (1-F)|\psi^{\perp}\rangle\langle\psi^{\perp}|$, where F denotes the fidelity of the stored state and $|\psi^{\perp}\rangle$ is the state orthogonal to the input state $|\psi\rangle$.

For storing a photon in an unknown qubit state the fidelity is bounded from above by $F^{\mathrm{CM}} = 0.667$ when using a classical memory [[31]], whereas for a quantum memory the upper bound is $F^{\mathrm{QM}} = 1$. The former bound strictly only applies to the storage of single-photon states, whereas, for coherent states, the bound is higher. Indeed, the best classical storage approach is optimized with respect to the mean number of photons per qubit and derives additional information about an input state by measuring individual photons from signals containing multiple photons in different bases. Furthermore, if the quantum memory features limited efficiency, then the best classical memory would selectively discard signals

containing one (or few) photons and measure only signals containing large numbers of photons. This would allow keeping the total recall efficiency unaffected while maximizing the fidelity. The adjusted bound, $\tilde{F}^{\mathrm{CM}}$, has been derived in[5, 32]. Given our mean photon number per pulse of 0.6 together with 0.3% system efficiency (1.5% memory and 20% waveguide coupling efficiencies) we compute $\tilde{F}^{\mathrm{CM}} = 0.841$.

The fidelity of the memory operation modifies the Bell-state measurement count rates as $\mathcal{R}^{\parallel} \rightarrow F\mathcal{R}^{\parallel} + (1-F)\mathcal{R}^{\perp}$, and likewise for $\mathcal{R}^{\perp}$. This allows us to express the error rate expected after imperfect storage of one of the pulses partaking in the Bell-state measurement:

$$e = \frac{F\mathcal{R}^{\parallel} + (1-F)\mathcal{R}^{\perp}}{\mathcal{R}^{\parallel} + \mathcal{R}^{\perp}}\,, \tag{8.4}$$

where the count rates $\mathcal{R}^{\parallel}$ and $\mathcal{R}^{\perp}$ are those expected without the memory. After simple algebra using (8.2) and (8.4), we find that $e_{e/l}^{(\mathrm{att})} = 1 - F$ for the qubits encoded in the e/l basis, and, using $\tilde{F}^{\mathrm{CM}} = 0.841$, this yields a lower bound of $\tilde{e}_{e/l}^{(\mathrm{att,CM})} = 0.159$ with a classical memory. Hence, our experimentally observed value of $e_{e/l}^{(\mathrm{exp})} = 0.039 \pm 0.037$ clearly violates the bound. In the $+/-$ basis we derive $e_{+/-}^{(\mathrm{att})} = (3-2F)/4$, which, in the case of an optimized classical memory, yields the lower bound $\tilde{e}_{+/-}^{(\mathrm{att,CM})} = 0.330$. Our measured value of $e_{+/-}^{(\mathrm{exp})} = 0.287 \pm 0.020$ is again below the classical limit.

We can also reverse the equations and estimate our memory's fidelity based on the measured error rates. In this case, inserting $e_{e/l}^{(\mathrm{exp})}$ and $e_{+/-}^{(\mathrm{exp})}$ into the appropriate expressions in the previous paragraph, we deduce the values $F_{e/l}^{\mathrm{exp}} = 0.961 \pm 0.037$ and $F_{+/-}^{\mathrm{exp}} = 0.926 \pm 0.041$. The measured estimates of the memory fidelity $F_{e/l}^{\mathrm{exp}}$ and $F_{+/-}^{\mathrm{exp}}$ in the two bases are equal to within the experimental error and well above the upper bound $\tilde{F}^{\mathrm{CM}} = 0.841$ for an optimized classical memory.

Although we do not use single photon sources for the experiments reported here, it is interesting to determine how well our results measure up to those that could have been obtained if single photon sources had been employed. For this, one can simply compute the count rate for the projection onto $|\psi^-\rangle$ for arbitrary two input qubits encoded into single photons (see Supplementary Note 4). We find that for any two parallel input qubit states ($\theta_a = \theta_b$ and $\phi_a = \phi_b$) we get $R^{\parallel} = 0$. Therefore, irrespective of the projection count rate for orthogonal input qubit states the expected error rate is always $e^{(\mathrm{sing})} = 0$, where *sing* identifies this value as belonging to the single photon case. Gauging the effect of storing one of the single photons partaking in the Bell-state measurement in a memory is thus independent of the basis and, using (8.4), we derive $e^{(\mathrm{sing})} = 1 - F$ and specifically compute the bound $e^{(\mathrm{sing,CM})} = 0.333$. We recognize that the two values $e^{(\mathrm{exp})}_{e/l} = 0.039 \pm 0.037$ and $e^{(\mathrm{exp})}_{+/-} = 0.287 \pm 0.020$ obtained experimentally are both well below $e^{(\mathrm{sing,CM})}$. This means that even with a single photon source at ones disposal the error rates that we measured could not have been attained with a classical memory.

Preparation and properties of our quantum memories. The fabrication of the Ti:Tm:$LiNbO_3$ waveguides and spectroscopic properties of Tm atoms in this material have been reported in ref. [[30]]. The two waveguides are fabricated identically but differ in terms of overall length, yielding optical depths of 2.5 for memory A and 3.6 for memory B.

To prepare an AFC memory, we perform frequency selective optical pumping on the inhomogeneously broadened transition of Tm at 795.5 nm wavelength. This process is determined by two factors, namely the spectrum of the pumping light, averaged over many pumping cycles, and the level structure of Ti:Tm:$LiNbO_3$. As detailed in ref. [[21]], the optical pumping is achieved by chirping the laser frequency while periodically modulating its intensity. Resonant atoms are excited and subsequently decay to a long-lived shelving state, yielding a spectral hole at the exitation wavelength. Hence, repeating this process a sufficiently long

time using pump light with (time-averaged) periodic spectrum results in periodic persistent spectral holes that form the troughs of the AFC. The atoms that are not excited by the pump light remain in the ground state and form the peaks of the AFC. Once the AFC is prepared, an incident photon is mapped onto a collective excitation of thulium ions and subsequently re-emitted after a pre-set storage time given by $t = 1/\Delta$, where Δ is the comb tooth spacing[26]. As the spectrum of the optical pumping light controls Δ, it allows one to set the storage (delay) time.

In our storage devices, Ti:Tm:$LiNbO_3$ crystals, the ground and shelving states are formed by the two nuclear Zeeman-levels that become non-degenerate with the application of a magnetic field along the C_3 axis of the crystals. To optimally prepare an AFC, we adjust the magnetic field such that the difference of the ground and excited level splittings matches the frequency separation between the AFC's troughs and peaks. The AFC in memory A for the single memory configuration is shown in Fig. 8.4a.

Note that, since memory A is located at the centre of the setup's solenoid while memory B is outside the solenoid (see Fig. 8.3), it is not possible to apply the same magnetic field across the two crystals. Hence, we cannot, in the two-memory configuration, generate the optimal level-splittings for both memories simultaneously. Instead, we apply a magnetic field that provides a reasonable balance in recall efficiencies but is not optimal for either memory. This is reflected by the different optical-depth profiles and reduced contrasts of the AFCs shown in red in Fig. 8.4b.

Memory operation. A quantum memory is said to be activated when we configure the MEMS to allow the optical pumping light to reach the memory during the preparation stage and thus tailor an AFC into the inhomogeneously broadened absorption spectrum of thulium

(see Fig. 8.3). If the optical pumping is blocked, the memory is said to be deactivated and light entering the waveguide merely experiences constant attenuation over its entire spectrum. In all cases, we adjust the mean photon number at the memory inputs so that mean photon numbers are equal at the HOM-BS inputs. This is required for achieving maximum visibility with attenuated laser pulses (see Supplementary Note 1).

Changing degrees of freedom. The polarization degree is easily adjusted using the free-space half- and quarter-wave plates set at each HOM-BS input. For our measurements we rotate the half-wave plate in steps of either 45 or 7.5 degrees. The temporal separation δt between a pulse arriving at one of the HOM-BS inputs and the next pulse in the train arriving at the other input can be expressed as $\delta t = \{nl/c\} \bmod \delta t_r$, where n is the refractive index of the fibres, $l \approx 10$ km is the path-length difference for pulses interacting with memory A and B, and δt_r is the repetition period of the pulse train from the AOM, which is set in the range of 350-400 ns. As we can change δt_r with 10 ps precision, we can tune δt on the ns scale. For the storage time scan, the recall efficiency decreases with storage time due to decoherence. Hence, we balance the mean photon number per pulse for stored and transmitted pulses for each storage time. Finally, to change the spectral overlap of the pulses input to the HOM-BS we can utilize that these pulses were generated at different times in the AOM and thus we can chose their carrier frequencies independently. We interchangeably drive the AOM by frequencies ν_a and ν_b and thus create two interlaced trains of pulses with different frequencies. By adjusting the pulse timing we can ensure that the pulses overlapped at the HOM-BS belong to different trains and thus have a spectral overlap given by $\delta\nu = \nu_a - \nu_b$. Due to the limited bandwidth of the AOM we are only able to scan $\delta\nu$ by 100 MHz, which, when compared to the 50 MHz pulse bandwidth, is not quite sufficient to make the pulses completely distinguishable. To achieve complete distinguishability, we supplement with a measurement using orthogonal polarizations at the inputs (see Supplementary Note 2).

Preparing states for Bell-state measurement. For the Bell-state projection measurement we interchangeably prepare time-bin qubits in either $|e\rangle$ or $|l\rangle$, or in $\frac{1}{\sqrt{2}}(|e\rangle + |l\rangle)$ and $\frac{1}{\sqrt{2}}(|e\rangle - |l\rangle)$ by setting the relative phase and intensity of the AOM drive signal. Adjusting the timing of the pulse preparation we ensure that qubits in different states overlap at the HOM-BS.

8.4 Conclusion and Discussion

In this study, we demonstrate two-photon interference of weak coherent laser pulses recalled from separate AFC-based waveguide quantum memories. Our measurement results show that the two-photon interference visibility stays near the theoretical maximum of 50% regardless of whether none, one, or both pulses have been recalled from our quantum memories. In addition, we demonstrate for the first time a Bell-state projection measurement with one of the two partaking qubits having been reversibly mapped to a quantum memory – a key element for advanced applications of quantum information processing. Our results show that solid-state AFC quantum memories are suitable for two-photon interference experiments, even in the general case of storing the two photons an unequal number of times.

Furthermore, we analyze quantum and classical bounds of the storage fidelity for Bell-state measurements with weak laser pulses and assess the quantum nature of our storage device by comparing our experimental results to the derived theoretical bounds. This approach follows the practice of employing attenuated laser pulses to characterize quantum memories[29, 5, 32], however, extending it from assessing the preservation of quantum information encoded in a single degree of freedom to assessing the preservation of all degrees of freedom of the photonic wavefunction. As long as the dark count rate is low, our mem-

ories' efficiencies do not affect the measured error rates as these are based on post-selected coincidence detection events. Thus our results pertain to the numerous applications, such as quantum repeaters, which incorporate post-selection.

Given these results, our quantum memories may soon be used as synchronization devices in multi-photon experiments. This will require an improvement of the system efficiency[33] and implementation of multi-mode storage supplemented by read-out on demand. The latter requirement can be achieved by storing photons occupying different temporal modes and adjusting the recall time of the photons[34]. Alternatively, it can be achieved by simultaneously storing photons in different spectral modes and selectively recalling photons in certain frequency modes (N.S., manuscript in preparation), which does not require adjustable storage time. This will allow increasing the number of photons that can be harnessed simultaneously for quantum information processing or fundamental tests beyond the current limit of eight[35]. A further goal is to develop workable quantum repeaters or, more generally, quantum networks, for which longer storage times are additionally needed. Depending on the required value, which may range from a hundred micro-seconds[36] to seconds[27], this may be achieved by storing quantum information in optical coherence, or it may require mapping of optical coherence onto spin states[26].

Bibliography

[1] H. -K. Lo, M. Curty, and B. Qi, Phys. Rev. Lett. 108, 130503 (2012)

[2] C. K. Hong, Z. -Y. Ou, and L. Mandel, Phys. Rev. Lett. 59, 2044 (1987)

[3] Kaltenbaek, R., Blauensteiner, B., Żukowski, M., Aspelmeyer, M. & Zeilinger, A. Experimental interference of independent photons. *Phys. Rev. Lett.* **96**, 240502 (2006).

[4] Beugnon, J. *et al.* Quantum interference between two single photons emitted by independently trapped atoms. *Nature* **440**, 779–782 (2006).

[5] Specht, H. P. *et al.* A single-atom quantum memory. *Nature* **473**, 190–193 (2011).

[6] Maunz, P. *et al.* Quantum interference of photon pairs from two remote trapped atomic ions. *Nat Phys* **3**, 538–541 (2007).

[7] Sanaka, K., Pawlis, A., Ladd, T. D., Lischka, K. & Yamamoto, Y. Indistinguishable photons from independent semiconductor nanostructures. *Phys. Rev. Lett.* **103**, 053601 (2009).

[8] Patel, R. B. *et al.* Two-photon interference of the emission from electrically tunable remote quantum dots. *Nat Photon* **4**, 632–635 (2010).

[9] Flagg, E. B. *et al.* Interference of single photons from two separate semiconductor quantum dots. *Phys. Rev. Lett.* **104**, 137401 (2010).

[10] Lettow, R. *et al.* Quantum interference of tunably indistinguishable photons from remote organic molecules. *Phys. Rev. Lett.* **104**, 123605 (2010).

[11] Bernien, H. *et al.* Two-photon quantum interference from separate nitrogen vacancy centers in diamond. *Phys. Rev. Lett.* **108**, 043604 (2012).

[12] Sipahigil, A. *et al.* Quantum interference of single photons from remote nitrogen-vacancy centers in diamond. *Phys. Rev. Lett.* **108**, 143601 (2012).

[13] Felinto, D. *et al.* Conditional control of the quantum states of remote atomic memories for quantum networking. *Nat Phys* **2**, 844–848 (2006).

[14] Chanelière, T. *et al.* Quantum interference of electromagnetic fields from remote quantum memories. *Phys. Rev. Lett.* **98**, 113602 (2007).

[15] Yuan, Z.-S. *et al.* Synchronized independent narrow-band single photons and efficient generation of photonic entanglement. *Phys. Rev. Lett.* **98**, 180503 (2007).

[16] Chen, Y.-A. *et al.* Memory-built-in quantum teleportation with photonic and atomic qubits. *Nat Phys* **4**, 103–107 (2008).

[17] Yuan, Z.-S. *et al.* Experimental demonstration of a bdcz quantum repeater node. *Nature* **454**, 1098–1101 (2008).

[18] Weinfurter, H. Experimental bell-state analysis. *Europhysics Letters* **25**, 559–564 (1994).

[19] Tittel, W. & Weihs, G. Photonic entanglement for fundamental tests and quantum communication. *Quant. Inf. Comp.* **1**, 3–56 (2001).

[20] Lvovsky, A. I., Sanders, B. C. & Tittel, W. Optical quantum memory. *Nat Photon* **3**, 706–714 (2009).

[21] Saglamyurek, E. *et al.* Broadband waveguide quantum memory for entangled photons. *Nature* **469**, 512–515 (2011).

[22] Clausen, C. *et al.* Quantum storage of photonic entanglement in a crystal. *Nature* **469**, 508–511 (2011).

[23] Zhang, H. *et al.* Preparation and storage of frequency-uncorrelated entangled photons from cavity-enhanced spontaneous parametric downconversion. *Nat Photon* **5**, 628–632 (2011).

[24] England, D. G. *et al.* High-fidelity polarization storage in a gigahertz bandwidth quantum memory. *Journal of Physics B: Atomic, Molecular and Optical Physics* **45**, 124008 (2012).

[25] Mandel, L. Photon interference and correlation effects produced by independent quantum sources. *Phys. Rev. A* **28**, 929–943 (1983).

[26] Afzelius, M., Simon, C., de Riedmatten, H. & Gisin, N. Multimode quantum memory based on atomic frequency combs. *Phys. Rev. A* **79**, 052329 (2009).

[27] Sangouard, N., Simon, C., de Riedmatten, H. & Gisin, N. Quantum repeaters based on atomic ensembles and linear optics. *Rev. Mod. Phys.* **83**, 33–80 (2011).

[28] Kok, P. *et al.* Linear optical quantum computing with photonic qubits. *Rev. Mod. Phys.* **79**, 135–174 (2007).

[29] de Riedmatten, H., Afzelius, M., Staudt, M. U., Simon, C. & Gisin, N. A solid-state light-matter interface at the single-photon level. *Nature* **456**, 773–777 (2008).

[30] Sinclair, N. *et al.* Spectroscopic investigations of a ti:tm:linbo3 waveguide for photon-echo quantum memory. *Journal of Luminescence* **130**, 1586 – 1593 (2010).

[31] Massar, S. & Popescu, S. Optimal extraction of information from finite quantum ensembles. *Phys. Rev. Lett.* **74**, 1259–1263 (1995).

[32] Gündoğan, M., Ledingham, P. M., Almasi, A., Cristiani, M. & de Riedmatten, H. Quantum storage of a photonic polarization qubit in a solid. *Phys. Rev. Lett.* **108**, 190504 (2012).

[33] Afzelius, M. & Simon, C. Impedance-matched cavity quantum memory. *Phys. Rev. A* **82**, 022310 (2010).

[34] Afzelius, M. *et al.* Demonstration of atomic frequency comb memory for light with spin-wave storage. *Phys. Rev. Lett.* **104**, 040503 (2010).

[35] Yao, X.-C. *et al.* Observation of eight-photon entanglement. *Nat Photon* **6**, 225–228 (2012).

[36] Munro, W. J., Harrison, K. A., Stephens, A. M., Devitt, S. J. & Nemoto, K. From quantum multiplexing to high-performance quantum networking. *Nat Photon* **4**, 792–796 (2010).

Chapter 9

Summary and Outlook

Secure communication is extremely important as our life becomes more dependent on public electronic systems, e.g, e-mail or internet banking, whose current security only relies on the assumption of limited computational power of an adversary. Ironically, in 1949, the *One Time Pad* (OTP) algorithm had been already proved to be information-theoretically secure presuming a random and serect key is used to encrypt a message, thus making the security of communication independent of any devices involved. Unfortunately, practical difficulties of creating such a secure random key have prevented the OTP from being widely used. However, a new technology, *Quantum Key Distribution* (QKD), promises to distribute a random and secret key with different users without revealing information to unauthorized parties and its security is guaranteed by the fundamental laws of quantum physics! In other words, the emergence of QKD opens doors towards invulnerable secure communications. Due to this powerful security, numerous QKD systems have already been tested in real world applications and some of them have even been commercialized.

Owing to transmission loss of physical channels, QKD is limited to practical distance of the order of a hundred kilometers. Fortunately, a beautiful idea, allowing one to overcome the distance limit, was proposed in 1998 : *the Quantum Repeater*. The protocol describes how distant users, e.g. Alice and Bob separated by 1,000 kilometers, can share a secret key with the aid of *Quantum Entanglement*. The long distance communication link is first segemented into several short-distance elementary links over which entanglement is established. Second, neighboring elementary links are entangled by means of entanglement swapping and the swapping operations continue until entanglement is distributed over the entire link between

Alice and Bob. In order to outperform direct transmission, each elementary link needs to prepare entanglement in a heralded manner and to map entangled photons in and out of quantum memories. Adjacent links are bridged via a *Bell State Measurement* (BSM). Thus, these three components are necessary for building a quantum repeater, i.e. generation of heralded entanglement, storage of entangled photons into quantum memories, and a BSM between recalled photons from quatnum memories. This thesis has mainly focused on experimental implementations of those three components.

First, it is important to understanding quantum entanglement qualitatively and quantitatively as it plays a key role not only in secure communication protocols including a device-independent QKD but also in fundamental tasks such as quanutm teleportation and a random number certification. For this reason, quantum entanglement verification tools, e.g. the Bell inequality and quantum state tomography, were extensively explained in Chapter 2. In the context of a quantum repeater, entanglement is the fundamental resource that allows establishing secure keys between distant users as well as distributing entanglement over long distances. Chapter 3 demonstrated the nonlocal nature of entangelment distributed in a real-world fibre link, and thereby its suitability for entanglement-based quantum key distribution. In Chapter 4, entanglement swapping with quantum-memory compatible photons was demonstrated, as requied for building an elementary link of a quantum repeater. Secondly, a quantum memory is an important ingredient in quantum computing and in the architecture of quantum repeaters. To understand how quantum storage is implemented, materials and protocol for quantum storage as well as its figures of merit were discussed in Chapter 2. The basic functioning of a quantum memory, i.e. storage of quantum bits, has been demonstrated in Chapter 5. Our solid-state quantum memories that interface with 795 nm- and telecommunication wavelength photons reveal their abilities of preserving entanglement during storage as introduced in Chapter 6 and 7, respectively. This confirms that

our quantum memories are suitable for a quantum repeater. Finally, Bell-state measurements between photons recalled from separate quantum memories were been demonstrated in Chapter 8, as required for bridging neighboring elementary links of a quantum repeater. As the obtained visibility of two-photon interference was near the theoretical maximum and the same with and without quantum memory storage our memories are able to preserve entire photonic wavefunctions, in addition to faithful storage of quantum bits and entanglement. Basic facts of two-photon interference and Bell-state measurement was discussed in Chapter 2.

This thesis studies the basic ingredients for building a quantum repeater. The next step is obviously to entangle two solid-state quantum memories, thereby establishing a complete elementary link of a quantum repeater. With Bell-state measurements, many elementary links can then be concatenated to establishing long-distance entangelment. From the practical point of view, all individual ingredients in the quantum repeater, including sources of entanglement, quantum memories, and Bell-state measurements, need to be operated efficiently in order to outperfrom the entanglement distribution rate of direct transmission over a long distance. One way is simply to develop technologies that allow increasing the efficiences of the individual components. Another idea is to multiplex many modes per attempt of entanglement distribution. As multiplexing can be done, in principle, in any degree of freedom, i.e. spatial, spectral, temporal, and polarization mode, multiple-mode multiplexing can significantly benefit on the communication rate. For instance, toward this goal, our group theoretically showed that, assuming high efficiencies of individual components, a 100 spectral-mode multiplexed quantum repeater can distribute entanglement faster than direct transmission of entanglement if the total communication distance is longer than only 200 kilometers [1]. In addition, they also experimentally demonstrated spectral multiplexing with 26 modes using an atomic freqeuncy comb (AFC) based quantum memory, thus taking

a further step towards realizing a practical real-world quantum repeater.

Bibliography

[1] N. Sinclair, E. Saglamyurek, H. Mallahzadeh, J. A. Slater, M. George, R. Ricken, M. P. Hedges, D. Oblak, C. Simon, W. Sohler, and W. Tittel, arXiv : 1309.3202 (2013)

Appendix A

Supplementary Information for Chapter 6

Preparation of the Atomic Frequency Comb (AFC)

The AFC amounts to a periodic modulation in frequency of the optical density of the inhomogeneously broadened $^3H_6 \leftrightarrow ^3H_4$ thulium absorption line. It can be generated by optically pumping atoms to off-resonant shelving levels - in our case nuclear Zeeman levels [1, 2]. To that end, we modulate the intensity of the 795 nm memory laser while scanning its frequency [3] . The frequency sweep is implemented using a lithium niobate phase modulator driven by a 20 GS/s arbitrary waveform generator. To avoid overlap of first and higher order modulation, the sweep extends from 5 GHz to 10 GHz, thus efficiently preparing a 5 GHz-bandwidth AFC memory. The laser intensity modulation is achieved by beating two frequency components, generated in an acousto-optic modulator (AOM) placed before the phase-modulator.

The memory storage time T_s is set by the frequency spacing between the teeth of the AFC, and is determined by $T_s = \delta/\alpha$, where $\delta = 0.35$ MHz is the difference between the two frequency components and $\alpha = 50 \times 10^{12}$ MHz/s is the sweep rate. This yields 142.85 MHz spacing between the AFC teeth, which translates into 7 ns memory storage time. For a high contrast AFC, the chirp cycle is repeated 100 times leading to a 10 ms overall optical pumping duration. The 2.2 ms wait time following the preparation corresponds to 27 times the radiative lifetime of the $^3H_4$ excited level, and ensures no fluorescence masks the retrieved photons.

The optical pumping involves population transfer between ground-state sublevels. As the

comb structure extends over all these levels, we carefully chose the magnetic field to make sure that those ions that initially absorb at frequencies where we desire a trough are transferred to frequencies where we desire a peak.

The Ti:Tm:$LiNbO_3$ waveguide

To fabricate the Ti:Tm:$LiNbO_3$ waveguide, a commercially available 0.5 mm thick Z-cut wafer of undoped, optical grade congruent lithium niobate (CLN) was cut into samples of 12 mm x 30 mm size. Tm doping was achieved by indiffusing a vacuum-deposited (electron-beam evaporated) Tm layer of 19.6 nm thickness. The diffusion was performed at 1130 °C during 150 h in an argon-atmosphere followed by a post treatment in oxygen (1 h) to get a full re-oxidization of the crystal. Tm occupies regular Li-sites when incorporated in CLN by diffusion [4]. The Tm indiffusion leads to a 1/e penetration depth of about 6.5 μm. The maximum Tm concentration of about 1.35×10^{20} cm^{-3} corresponds to a concentration of 0.74 mole %, which is considerably below the solid solubility of Tm in CLN [5]. Subsequently, the waveguide was formed by the well-known Ti–indiffusion technique. At first, a 40 nm thick titanium layer was electron-beam deposited on the Tm-doped surface of the CLN substrate. From this layer, 3.0 μm wide Ti stripes were defined by photo-lithography and chemical etching and subsequently in-diffused at 1060°C for 5 h to form 30 mm long optical strip waveguides. In the wavelength range around 795 nm, the waveguides are single mode for TE- and TM-polarization. To finish the fabrication, the waveguide was cut to 15.7 mm and end faces were carefully polished normal to the waveguide axis.

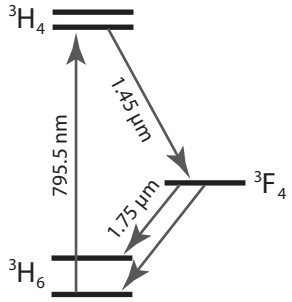

Figure A.1: Simplified level diagram for Tm:$LiNbO_3$.

Limitation to efficiency

While the current system efficiency (characterizing the probability for a photon that enters the cryostat to leave it after recall) of around 0.2% is sufficient to show the entanglement-preserving nature of the storage process, it is clear that this number has to be improved to make the memory more practical and to allow for more involved fundamental measurements.

First, we note that better optical mode matching between the fibre and the $LiNbO_3$ waveguide can be expected to improve the fibre-to-fibre transmission from 10% to 50%.

Second, assuming storage in optical coherence and Gaussian-shaped teeth, the efficiency of the first recall in the forward direction is given by

$$\epsilon = (d_1/F)^2 e^{-d_1/F} e^{-7/F^2} e^{-d_0} \tag{A.1}$$

where $F = \Delta/\gamma$ denotes the finesse of the comb, and d_1/F and d_0 are the reversible and irreversible optical depth [6] (see supplementary figure A.1). As discussed above, our comb structure extends over all ground state levels. This fixes the fidelity of the comb to two, as ions can only be "shuffled around" but not removed from the spectral region covered by the SPDC photons. This impacts on the memory efficiency and sets, according to Eq. A.1, an upper bound of $\approx 10\%$. Yet, we note that the memory efficiency can be increased

when applying a phase-matching operation that results in backward emission of the stored photon. Further improvement is expected when changing the teeth shape from Gaussian to square [7]. All options combined, it seems possible to achieve a system efficiency of around 15%, which is 75 times larger than in the current implementation. We point out that the limitation due to the comb finesse is not necessarily a consequence of generating broadband combs, but of the small Zeeman splitting of the thulium ground state levels relative to the storage bandwidth. Provided the splitting between the long-lived atomic levels involved in the optical pumping procedure exceeds the storage bandwidth, the finesse can be increased beyond two, and memory efficiencies up to 100% are possible. This may be possible when using the $^3F_4$ level as shelving level, or for other RE impurities featuring greater sensitivity to magnetic fields [8].

Longer storage time and on-demand readout

Currently, the maximum storage time of our memory is approximately 300 ns. This value is determined by the minimum tooth spacing of the AFC, which is limited by spectral diffusion [1, 2] . However, spectroscopic investigation of a Tm:$LiNbO_3$ bulk crystal shows that spectral diffusion decreases when lowering the temperature, similar to the observed improvement of the optical coherence time [2]. This implies the possibility to extend the storage time.

In addition, it may be possible to further improve the storage time and achieve on-demand recall by temporarily transferring the optical excited coherence between the $^3H_6$ and $^3H_4$ levels to coherence between the $^3H_6$ and $^3F_4$ electronic levels, similar to storage of coherence in spin-waves [9]. However, the coherence properties and the suitability of the $^3F_4$ state for such a transfer remains to be investigated. Furthermore, combining the AFC protocol with a quantum memory approach based on controlled reversible inhomogeneous broadening

(CRIB) [8] allows one to inhibit the pre-set rephasing of coherence by adding additional, controlled inhomogeneous broadening of each line in the AFC. Rephasing would occur only after reversing, i.e. undoing, the additionally introduced dephasing, and readout would be possible after any multiple of the AFC recall time determined by the tooth spacing.

The measurement

First, we stabilize the pump interferometer and the 1532 nm interferometer to arbitrarily chosen phase values. We define the phase introduced by the pump interferometer to be zero, i.e. we absorb it into the definition of the "early" and "late" qubit states, leading to the maximally entangled state

$$\left|\phi^{+}\right\rangle = \frac{1}{\sqrt{2}}\left(|e,e\rangle + |l,l\rangle\right) \tag{A.2}$$

Furthermore, we define the measurement performed by the 1532 nm qubit analyzer to be $+\sigma_x$. Next, we change the phase of the 795 nm interferometer and maximize the normalized *joint detection probability*

$$P(\boldsymbol{a},\boldsymbol{b}) = \frac{C(\boldsymbol{a},\boldsymbol{b})}{C(\boldsymbol{a},\boldsymbol{b}) + C(\boldsymbol{a},-\boldsymbol{b})} \tag{A.3}$$

with a fibre delay line in place of the memory. We define this setting to correspond to a projection onto $+\sigma_x$, and we measure $P_{in}(\sigma_x \otimes \sigma_x)$ over 5 minutes. This measurement (without the memory) is taken as being on the state ρ_{in}, i.e. the bi-photon state before storage. Next, we add the memory and similarly measure $P_{out}(\sigma_x \otimes \sigma_x)$ over approximately 5 hours. When necessary to change the setting of either qubit analyzer to σ_y, we increase the phase difference introduced by the respective interferometer by $\pi/2$. For projection measurements onto σ_z, we use the delay line in the qubit analyzer. Each joint projection measurement is done with and without memory; the results, given in supplementary table A.1, allow calculating

	$\sigma_x \otimes \sigma_x$	$\sigma_x \otimes \sigma_y$	$\sigma_x \otimes \sigma_z$	$\sigma_x \otimes -\sigma_z$	$\sigma_y \otimes \sigma_x$	$\sigma_y \otimes \sigma_y$	$\sigma_y \otimes \sigma_z$	$\sigma_y \otimes -\sigma_z$
P_{in} [%]	90±2	49±1	49±1	51±1	52±1	10±2	51±1	49±1
P_{out} [%]	89±6	49±8	48±4	52±4	49±6	14±5	49±4	51±4
	$\sigma_z \otimes \sigma_x$	$\sigma_z \otimes \sigma_y$	$\sigma_z \otimes \sigma_z$	$\sigma_z \otimes -\sigma_z$	$-\sigma_z \otimes \sigma_x$	$-\sigma_z \otimes \sigma_y$	$-\sigma_z \otimes \sigma_z$	$-\sigma_z \otimes -\sigma_z$
P_{in} [%]	46±1	46±1	94.2±0.1	5.8±0.1	46±1	45±1	7.6±0.2	93.0±0.2
P_{out} [%]	51±6	56±6	94±1	6±1	48±5	52±5	6±1	94±1

Table A.1: **Joint-detection probabilities for density matrix reconstruction:** Measured joint-detection probabilities for all projection measurements required to calculate the density matrices for the bi-photon state emitted from the source (P_{in}), and after storage and recall of the 795 nm photon (P_{out}). Uncertainties indicate one-sigma standard deviations based on Poissonian detection statistics.

the density matrices ρ_{in} and ρ_{out} describing the photon pair states before and after storage, respectively [10].

To measure the correlation coefficients

$$E(\boldsymbol{a},\boldsymbol{b}) = \frac{C(\boldsymbol{a},\boldsymbol{b}) - C(\boldsymbol{a},-\boldsymbol{b}) - C(-\boldsymbol{a},\boldsymbol{b}) + C(-\boldsymbol{a},-\boldsymbol{b})}{C(\boldsymbol{a},\boldsymbol{b}) + C(\boldsymbol{a},-\boldsymbol{b}) + C(-\boldsymbol{a},\boldsymbol{b}) + C(-\boldsymbol{a},-\boldsymbol{b})} \tag{A.4}$$

required for testing the Clauser-Horne-Shimony-Holt (CHSH) Bell inequality [11]. we chose, $\boldsymbol{a} = \sigma_x$, $\boldsymbol{a'} = \sigma_y$, $\boldsymbol{b} = \sigma_x + \sigma_y$, and $\boldsymbol{b'} = \sigma_x - \sigma_y$. Projections onto $\sigma_x \pm \sigma_y$ require changing phase differences by $\pm\pi/4$ as compared to those defining projections onto σ_x. For this measurement we added a detector to the second output of the interferometer in the 795 nm qubit analyzer so that C(**a**,**b**), C(**-a**,**b**), C(**a**,**-b**) and C(**-a**,**-b**) could be measured simultaneously. Measurements without memory are done over 15 min, those with memory over 12-15 hours. The resulting correlation coefficients are detailed in supplementary table A.2. From these we calculate $S_{in} = 2.379 \pm 0.034 > 2$ before storage and $S_{out} = 2.25 \pm 0.06 > 2$ after storage. Both are approximately equal, larger than 2, and hence violate the CHSH Bell inequality, proving again the presence of entanglement and, beyond that, the suitability of the bi-photon states for quantum key distribution [12] . Moreover, the measured S–values

	$\sigma_y \otimes (\sigma_x + \sigma_y)$	$\sigma_y \otimes (\sigma_x - \sigma_y)$	$\sigma_x \otimes (\sigma_x + \sigma_y)$	$\sigma_x \otimes (\sigma_x - \sigma_y)$
E_{in} [%]	59.7±1.7	-55.4±1.9	52.0±1.5	70.8±1.8
E_{out} [%]	54±3	-64±4	53±3	53±3

Table A.2: **Correlation coefficients for Bell-inequality tests:** Measured correlation coefficients (see Eq. A.4) required to test the CHSH Bell inequality. Uncertainties indicate one-sigma standard deviations based on Poissonian detection statistics.

are in good agreement with the respective theoretical values of $S_{th} = 2.235 \pm 0.085$ and $S_{th} = 2.2 \pm 0.22$ calculated using the measured density matrix with uncertainties estimated from Monte-Carlo simulations.

Calculation of purity, entanglement measures [13] and fidelities

Assuming an arbitrary two-qubit input state ρ, the *concurrence* is defined as $C(\rho) = \max\{0, \lambda_1 - \lambda_2 - \lambda_3 - \lambda_4\}$, where the λ_i's are, in decreasing order, the square roots of the eigenvalues of the matrix $\rho(\sigma_y \otimes \sigma_y)\rho^*(\sigma_y \otimes \sigma_y)$ and ρ^* is the element wise complex conjugate of ρ. The *entanglement of formation* is then calculated as

$$E_F(\rho) = H\left(0.5 + 0.5\sqrt{1 - C^2(\rho)}\right) \tag{A.5}$$

where $H(x) = -x\log_2 x - (1-x)\log_2(1-x)$. Finally, fidelity between ρ and σ is

$$F(\rho, \sigma) = \left(tr\sqrt{\sqrt{\rho}\sigma\sqrt{\rho}}\right)^2 \tag{A.6}$$

and the *purity* of a state ρ is

$$P = \mathrm{tr}(\rho^2) \tag{A.7}$$

Bibliography

[1] Plenio, M. B. & Virmani, S. An introduction to entanglement measures. Quant. Inf. Computation 7, 1 (2007)

[2] Thiel, C.W., Sun, Y., Bottger, T., Babbitt, W.R. and Cone, R.L. Optical decoherence and persistent spectral hole burning in Tm^{3+}:$LiNbO_3$. J. Lumin, 130 (9), 1603-1609 (2010).

[3] Reibel R.R., Barber, Z.W., Fischer, J.A., Tian, M. and Babbitt, W.R. Broadband demonstrations of true-time delay using linear sideband chirped programming and optical coherent transients. J. Lumin. 107, 103-113 (2004)

[4] Novikov, D. V. et al. Plane wave GID topography of defects in lithium niobate after diffusion doping, Nuclear Instruments and Methods in Physics Research B 97, 342-345 (1995)

[5] Quintanilla, M., Cantelar, E., Sanz-Garca, J.A. Cusso, F. Growth and optical characterization of Tm^{3+}-doped $LiNbO_3$. Optical Materials 30, 1098-1102 (2008)

[6] Afzelius, M., Simon, C., de Riedmatten, H. and Gisin, N. Multimode quantum memory based on atomic frequency combs. Phys. Rev. A 79, 052329 (2009)

[7] Bonarota, M., Ruggiero, J., Le Gouet, J.-L. and Chaneliere, T. Efficiency optimization for Atomic Frequency Comb storage. Preprint at http://arxiv.org/abs/0911.4359 (2009)

[8] Tittel, W. et al. Photon-echo quantum memory in solid state systems. Laser and Photon. Rev. 4, (2), 244-267 (2010)

[9] Afzelius, M. et al. Demonstration of Atomic Frequency Comb Memory for Light with Spin-Wave Storage. Phys. Rev. Lett. 104, 040503 (2010)

[10] Altepeter, J. B., Jeffrey, E. R., &. Kwiat, P. G. Photonic state tomography. Adv. At. Mol. Opt. Phys. 52, 105 (2005)

[11] Clauser, J.F., Horne, M.A., Shimony, A. and Holt, R.A. Proposed experiment to test local hidden-variable theories. Phys. Rev. Lett. 23, 880-884 (1969)

[12] Gisin, N., Ribordy, G., Tittel, W. & Zbinden, H. Quantum cryptography. Rev. Mod. Phys. 74, 145 (2002)

[13] Plenio, M. B. & Virmani, S. An introduction to entanglement measures. Quant. Info. Comput. 7, 1 (2007)

Appendix B

Supplementary Information for Chapter 7

Superconducting nanowire single photon detector

A critical component in our demonstration is the superconducting nanowire single photon detector (SNSPD), which allows for highly efficient detection of the recalled telecom photons with very low dark count rate. Our detector is based on a superconducting tungsten silicide (WSi) nanowire meander and has been developed by some of us at the National Institute for Standards and Technology (NIST) and the Jet Propulsion Laboratory (JPL). Its performance, including high detection efficiency, has been detailed before [1]. In our experiments the detector is mounted on the ADR stage of the cryostat and kept at the same temperature as the fibre memory (0.8–1K). For the detector used for the majority of the measurements [2] we found the system detection efficiency to be $\sim$60%, which includes transmission loss through coiled fibres inside the cryostat and splice loss. We measured a dark count rate of around 10 Hz and a dead time of $\sim$35 ns. Furthermore, we found the timing jitter of the detector used for the time-bin projection measurements to be around 250 ps, which allows us to resolve the two, 1.4 ns separated temporal modes that constitute our time-bin qubits. We note that, as opposed to widely used InGaAs-based single photon detectors, our detector does not require any gating signals. Employing the SNSPD in our quantum memory demonstration allows substantially reduced measurement times and increased signal-to-noise ratio.

The erbium-doped silicate fibre

We use a twenty-meter-long, single-mode, erbium doped silica fibre manufactured by INO, Canada. In addition to Er, the fibre contains Ge, P and Al co-dopants. The concentration of the erbium atoms is 80 ppm-wt, leading to 0.6 dB/m absorption at 1532 nm and at room temperature. The fibre is spooled in layers around a copper cylinder with ∼4 cm diameter that is thermally contacted with the base plate of an adiabatic demagnetization refrigerator maintained at 0.8-1 K and exposed to a magnetic field of ∼600 G. The fibre is fusion-spliced to standard SMF-28 single mode fibres, resulting in less than 5% loss per splice.

AFC memory

Efficiency

When triggering a forward propagating echo, as in our investigation, the recall efficiency of an AFC quantum memory, η, is limited to 54% [3]. However, it can reach unity by either satisfying a phase matching condition that leads to re-emission in the backward propagation [3, 4], or by embedding the storage material into an impedance-matched cavity [5, 6]. The comb finesse F, defined as the ratio of the comb peak spacing to the width of the peaks, the optical depth of the peaks (referred to as d_1), and the optical depth of the remaining background (due to imperfect persistent spectral hole burning and referred to as d_0) are the main parameters that determine the recall efficiency η [3]. Assuming forward recall, the efficiency is given by:

$$\eta = \left(\frac{d_1}{F}\right)^2 e^{-d_1/F} e^{-7/F^2} e^{-d_0} \tag{B.1}$$

where we assumed Gaussian-shaped comb teeth. At temperatures between 0.8 and 1K, we find d_0 to be 1–1.3, which results in around 70% of the input photons being irreversibly absorbed. Together with a finesse of 2 and d_1 of 1, Eq. SB.1 yields a recall efficiency of

around 1%, which we confirmed by comparing the number of input and recalled photons.

As will be further described in [7], we observe a strong temperature dependence of the hole-burning efficiency, i.e the percentage of the atomic population transferred to other magnetic sub-levels. In addition, spin mixing and stimulated emission during spectral hole burning [8] are expected to further decrease d_0 and thus to increase the efficiency of our AFC memory. Moreover, we observe that the quality of the hole burning significantly depends on the doping concentration of erbium as well as the co-dopants in the fibre. Finally, we note that the strong laser beam used for spectral hole burning propagates in the opposite direction compared to the photons to be stored, which results in reduced pumping efficiency due to imperfect polarization overlap in the non polarization-maintaining fibre. In summary, we expect that a substantial decrease in d_0, and hence a substantial increase in efficiency can be achieved under optimized experimental conditions.

Storage time

The storage time in an AFC memory using a two-level atomic system is pre-determined by the spacing Δ between the teeth of the AFC [3]:

$$t_{\text{storage}} = 1/\Delta. \tag{B.2}$$

Longer storage times require smaller spacing of the AFC peaks, which is limited by laser jitter and power broadening during spectral hole burning, spectral diffusion [9] and, fundamentally, the homogeneous linewidth Γ_{hom}(which is inversely proportional to the coherence time T_2), setting an upper limit to the storage time.

While rare-earth-ion doped glasses have not received as much attention as rare-earth-ion doped crystals, there are several studies of their low-temperature coherence properties (see,

e.g., [10, 11, 12, 13, 14, 15]). For silicate fibres with high erbium doping concentration, coherence times up to 3.8 μs have been reported at 0.15 K and 2 T magnetic field [14] — they are limited by spectral diffusion and coupling to two-level systems (which are specific to amorphous materials such as glass). The application of (relatively high) magnetic fields can suppress these mechanism to some extent. In addition, it has been suggested that reducing the doping concentration may yield longer coherence times due to reduced magnetic interactions between erbium ions [14]. Under our experimental conditions (a magnetic field of ∼600 Gauss and a temperature of 0.8–1 K), we have stored photons up to 35 ns using an 8 GHz-wide AFC, yielding a time-bandwidth product of ∼300.

We note that, while the storage time in our investigation was pre-set, there are several, not yet investigated possibilities that may allow deciding the moment of recall after a photon has been absorbed. First, erbium features a large number of hyperfine states, which may allow reversible mapping of optically excited coherence onto spin waves [16]. In turn, this would allow selecting the recall time on demand [3]. Second, given the here-demonstrated possibility for persistent spectral hole burning, together with the possibility for reversible broadening using the DC Stark effect [17], one can turn to the photon echo quantum memory protocol based on controlled reversible inhomogeneous broadening (CRIB)[18, 19]. And finally, we emphasize that every application that requires read-out on demand in the temporal domain can be realized using read-out on demand in the spectral domain (where, instead of being localized in time bins, photons occupy specific frequency bins) [20]. Our memory can readily be employed for the latter.

Bandwidth

The generally large inhomogeneously broadened absorption lines of rare-earth-ion doped solids, in our case around 1.3 THz (equivalent to 10 nm bandwidth), allow tailoring wide-bandwidth AFCs. However, the frequency spacing between the ground state and the shelving

	$\sigma_x \otimes \sigma_x$	$\sigma_x \otimes \sigma_y$	$\sigma_x \otimes \sigma_z$	$\sigma_x \otimes -\sigma_z$	$\sigma_y \otimes \sigma_x$	$\sigma_y \otimes \sigma_y$	$\sigma_y \otimes \sigma_z$	$\sigma_y \otimes -\sigma_z$
P_{in} [%]	89±1	46±1	49±1	51±1	51±1	12±1	49±1	51±1
P_{out} [%]	87±5	51±5	49±5	51±5	46±5	13±5	54±5	46±5
	$\sigma_z \otimes \sigma_x$	$\sigma_z \otimes \sigma_y$	$\sigma_z \otimes \sigma_z$	$\sigma_z \otimes -\sigma_z$	$-\sigma_z \otimes \sigma_x$	$-\sigma_z \otimes \sigma_y$	$-\sigma_z \otimes \sigma_z$	$-\sigma_z \otimes -\sigma_z$
P_{in} [%]	49±1	49±1	89±1	11±1	51±1	51±1	13±1	87±1
P_{out} [%]	47±3	49±3.	87±2	13±2	53±3	51±3	12±1	88±1

Table B.1: **Joint-detection probabilities for density matrix reconstruction:** Measured joint-detection probabilities for all projection measurements required to calculate the density matrices for the bi-photon state emitted from the source (P_{in}), and the state after storage and recall of the telecom photon (P_{out}). Uncertainties indicate one-sigma standard deviations calculated from Poissonian detection statistics.

level used for persistent hole burning (assumed here to be neighbouring) sets a limit to the bandwidth over which high recall efficiencies can be achieved (see the Supplementary Information of [21]). Hence, the use of shelving levels of magnetic origin is very attractive, in particular in the case of large magnetic sensitivity as in erbium, because they allow for variable and large level-splitting using small magnetic fields.

However, the magnetic field also affects the persistence of the tailored spectral holes [22, 23] — large fields often lead to reduced persistence. This creates a trade-off between having a long AFC life-time (which benefits the creation of a high-quality AFC through repeated hole burning) and a large splitting (i.e. large bandwidth over which photons can be stored efficiently).

For our AFC preparation, we operate at 0.8 - 1K and apply a magnetic field of 600 Gauss, which results in sufficiently long-lived AFCs. However, as we increase the AFC bandwidth beyond 4 GHz, we see a level-spacing induced increase of d_0, which limits our recall efficiency.

	$\sigma_y \otimes (\sigma_x + \sigma_y)$	$\sigma_y \otimes (\sigma_x - \sigma_y)$	$\sigma_x \otimes (\sigma_x + \sigma_y)$	$\sigma_x \otimes (\sigma_x - \sigma_y)$
E_{in} [%]	55.4±1.4	58.8±1.3	65.3±1.3	58.7±1.4
E_{out} [%]	55.4±6.2	0.65±6.0	57.9±5.5	54.9±4.9

Table B.2: **Measurement settings and correlation coefficients for Bell-inequality tests.** We measure four correlation coefficients using photon pairs before (in) and after (out) storage of the telecommunication photon. The local measurements are described by superpositions of Pauli operators, and are chosen to maximally violate the CHSH inequality. Uncertainties indicate one-sigma standard deviations and are based on Poissonian detection statistics.

Experimental data

The following tables detail the results of the measurements related to the reconstruction of density matrices (Table. SB.1), and the CHSH Bell inequality tests (Table. SB.2).

Calculation of purity, entanglement measures [24] and fidelities

Assuming an arbitrary two-qubit input state ρ, the *concurrence* is defined as

$$C(\rho) = \max\{0, \lambda_1 - \lambda_2 - \lambda_3 - \lambda_4\} \tag{B.3}$$

where the λ_i's are, in decreasing order, the square roots of the eigenvalues of the matrix $\rho(\sigma_y \otimes \sigma_y)\rho^*(\sigma_y \otimes \sigma_y)$ and ρ^* is the element-wise complex conjugate of ρ. The *entanglement of formation* is then calculated as

$$E_F(\rho) = H\left(0.5 + 0.5\sqrt{1 - C^2(\rho)}\right) \tag{B.4}$$

where $H(x) = -x\log_2 x - (1-x)\log_2(1-x)$. The fidelity between ρ and σ is

$$F(\rho, \sigma) = \left(tr\sqrt{\sqrt{\rho}\sigma\sqrt{\rho}}\right)^2 \tag{B.5}$$

and the *purity* of a state ρ is

$$P = \mathrm{tr}(\rho^2) \tag{B.6}$$

Finally, the optimum value for S in CHSH Bell-inequality tests (which is the value we expect to measure using optimized measurement settings) can be found from the concurrence:

$$S_{th} = 2\sqrt{1 + C^2}. \tag{B.7}$$

Bibliography

[1] Marsili F. et al. Detecting single infrared photons with 93 % system efficiency. *Nature Photon.* **7**, 210-214 (2013).

[2] Only the data in Fig. 2 in the main text was acquired using the SNSPD-variant described in [**?**].

[3] Afzelius, M., Simon, C., de Riedmatten, H. & Gisin, N. Multimode quantum memory based on atomic frequency combs *Phys. Rev. A* **79** 052329 (2009)

[4] Tian, M., Vega, D., & Dilles, J. Quantum memory based on a spatiospectral atomic comb *Phys. Rev. A* **87,** 042338 (2013).

[5] Afzelius, M. & Simon C Impedance matched cavity quantum memory *Phys. Rev. A* **82**, 022310 (2010).

[6] Moiseev, S. A., Andrianov, S. N., and Gubaidullin, F. F. Efficient multimode quantum memory based on photon echo in an optimal QED cavity *Phys. Rev. A* **82**, 022311 (2010).

[7] Saglamyurek, E. et al. Investigations of persistence spectral hole burning in erbium doped silicate fibre for quantum information processing applications. *In preparation.* (2014)

[8] Lauritzen B., Hastings–Simon, S. R., de Riedmatten H., Afzelius, M., Gisin, G. State preparation by optical pumping in Erbium doped solids using stimulated emission and spin mixing. *Phys. Rev. A*, **78**, 043402 (2008)

[9] Liu, G. & Jacquier, B. *Spectroscopic Properties of Rare Earths in Optical Materials* (Springer, 2006).

[10] Huber, D. L., Broer, M. M., Golding, B. Low-temperature optical dephasing rare-earth ions in glass. *Phys. Rev. Lett.* **52**, 2281 (1984)

[11] Broer, M. M., Golding, B., Heammerle, H., Simpson, J. R., Huber, D. L. Low-temperature optical dephasing of rare-earth ions in inorganic glasses *Phys. Rev. B* **33**, 4160 (1986)

[12] Geva, E. & Skinner, J. L. Theory of photon echoes and hole burning in low temperature glasses: How good are the standard approximations?, *J. Chem. Phys.* **107**, 7630 (1997).

[13] McFarlane, R. M, Sun, Y., Sellin, P. B., Cone, R. L. Optical decoherence in Er^{3+}–doped silicate fiber: Evidence for coupled spin-elastic tunneling systems.*Phys. Rev. Lett.* **96**, 033602 (2006)

[14] Staudt, M. U. et al. Investigations of optical coherence properties in an erbium-doped silicate fiber for quantum state storage. *Opt. Commun.* **266**, 2, 720-726 (2006).

[15] McFarlane, R. M, Sun, Y., Sellin, P. B., Cone, R. L. Optical decoherence times and spectral diffusion in an Er-doped optical fibre measured by two-pulse echoes, stimulated photon echoes, and spectral hole burning. *J. Lumin.* **127**, 1, 61-64 (2007)

[16] Afzelius, M. et al. Demonstration of atomic frequency comb memory for light with spin-wave storage. *Phys. Rev. Lett.* **104**, 040503 (2010).

[17] Hastings–Simon, S.R. et al. Controlled Stark shifts in Er^{3+}–doped crystalline and amorphous waveguides for quantum state storage *Opt. Commun.*, **266**, 2, 716-719 (2006).

[18] Kraus, B. et al. Quantum memory for nonstationary light fields based on controlled reversible inhomogeneous broadening. *Phys. Rev. A* **73** 020302 (2006)

[19] Alexander, A. L., Longdell, J. J., Sellars M. J. & Manson, N. B. Photon echoes produced by switching electric fields. *Phys. Rev. Lett.* **96**, 043602 (2006)

[20] Sinclair, N. et al. A solid-state memory for multiplexed quantum states of light with read-out on demand. arXiv:1309.3202v1 [quant-ph] (2013).

[21] Saglamyurek, E. et al. Broadband waveguide quantum memory for entangled photons. *Nature*, **469**, 513-518 (2011).

[22] Hastings–Simon, S. R. et al. Zeeman-level lifetimes in Er^{3+}:Y_2SiO_5. *Phys. Rev. B*, **78**, 085410 (2008).

[23] Thiel, C. W. et al. Optical decoherence and persistent spectral hole burning in Er^{3+}:$LiNbO_3$. *J. Lumin.*, **130**,9, 1603-1609 (2010).

[24] Plenio, M. B. & Virmani, S. An introduction to entanglement measures. Quant. Inf. Comput. 7, 1–51 (2007)

Appendix C

Supplementary Information for Chapter 8

In the following theoretical treatment we will derive expressions for the coincidence and single-detector counts in terms of probabilities. By multiplying these probabilities with the average experimental repetition rate we can easily calculate the predicted experimental count rates. To a large extent though, we will mainly be interested in relative probabilities or count rates between different settings of the degrees of freedom of pulses.

It is reasonably straightforward to derive the rates of detection of photons at the outputs of a BS (note that in this Supplementary Information, the HOM-BS of the main text will be referred to as just BS) In our case coherent states $|\alpha\rangle$ and $|\beta\rangle$, characterized by mean photon numbers $\langle\hat{a}^\dagger\hat{a}\rangle = |\alpha|^2$ and $\langle\hat{b}^\dagger\hat{b}\rangle = |\beta|^2$, occupy the two spatial input modes of the BS. In the Fock-basis the coherent state can be represented as

$$|\alpha\rangle = \sum_{n=0}^{\infty} e^{-\frac{|\alpha|^2}{2}} \frac{\alpha^n}{\sqrt{n!}}|n\rangle = \sum_{n=0}^{\infty} e^{-\frac{|\alpha|^2}{2}} \frac{\alpha^n}{n!}(\hat{a}^\dagger)^n|0\rangle, \tag{C.1}$$

and similarly for $|\beta\rangle$.

To account for the cases of photons being distinguishable and indistinguishable at the BS we must allow for an additional degree of freedom in each of the spatial modes, e.g. polarization, frequency, or time. Thus we write the input state at one of the BS inputs as $|\alpha_1, \alpha_2\rangle \equiv |\alpha_1\rangle \otimes |\alpha_2\rangle$, where α_1 and α_2 are the coherent state amplitudes in the two orthogonal modes of the auxiliary degree of freedom within the same spatial mode. We treat the coherent state at the other BS input in a similar way.

For the case in which the fields at the inputs of the BS are distinguishable with respect to the auxiliary degree of freedom, the inputs to the BS are described as being in the state

$|\alpha,\, 0\rangle|0,\, \beta\rangle \equiv |\alpha,\, 0\rangle \otimes |0,\, \beta\rangle$, whereas in the case of them being indistinguishable (up to a difference in the mean photon number) the input fields are written as $|\alpha,\, 0\rangle|\beta,\, 0\rangle$.

The BS is characterized by its reflection amplitude r and transmission amplitude $t = \sqrt{1-|r|^2}$, which cause the input creation operators to transform as $\hat{a}^\dagger \to t\hat{c}^\dagger + ir\hat{d}^\dagger$ and $\hat{b}^\dagger \to ir\hat{c}^\dagger + t\hat{d}^\dagger$. With this in hand, we can compute the state in the BS outputs for any combination of Fock states at the inputs. When the two input states are indistinguishable, i.e. in the same auxiliary degree of freedom, we get[1]

$$|n,0\rangle|m,0\rangle \to \sum_{j=0}^{n}\sum_{k=0}^{m} K_{\|}(n,m,j,k)\,|j+k,\,0\rangle|n+m-j-k,\,0\rangle \tag{C.2}$$

$$K_{\|}(n,m,j,k) = t^{m-k+j}(ir)^{n-j+k}\sqrt{\binom{n}{j}\binom{m}{k}\binom{j+k}{j}\binom{n+m-j-k}{n-j}},$$

where the binomial coefficient $\binom{x}{y} = \frac{x!}{y!(x-y)!}$. For distinguishable input fields the output state is slightly simpler

$$|n,0\rangle|0,m\rangle \to \sum_{j=0}^{n}\sum_{k=0}^{m} K_{\perp}(n,m,j,k)\,|j,\,k\rangle|n-j,\,m-k\rangle \tag{C.3}$$

$$K_{\perp}(n,m,j,k) = t^{m-k+j}(ir)^{n-j+k}\sqrt{\binom{n}{j}\binom{m}{k}}.$$

The above calculated output modes impinge on the single photon detectors (SPDs). These may be characterized by the probability of detecting an incident single photon. From this single photon detection probability η it is also possible to deduce the probability of detecting a pulse consisting of multiple photons, keeping in mind that, irrespective of the number of photons, only a single detection event can be generated. We write $p_1(n)$ for the probability for generating one detector event given n incident photons, and it is useful to note that it relates to the probability $p_0(n)$ of detecting nothing as $p_1(n) = 1 - p_0(n)$. The probability for not detecting n photons is, on the other hand, easily computed as $p_0(n) = (1-\eta)^n$. Since

the two detectors at the BS outputs are independent, the probability $p_{11}(n,m)$ of generating a coincidence event, i.e. having simultaneous detection events in each of the detectors, given n and m photons in one and the other output is simply $p_{11}(n,m) = p_1(n)p_1(m)$. Thus the probability for a coincidence detection becomes

$$p_{11}(n,m) = \left[1-(1-\eta_1)^n\right]\left[1-(1-\eta_2)^m\right] , \tag{C.4}$$

where η_1 and η_2 are the single photon detection probabilities for detector 1 and 2, respectively. Expressing the coincidence detection probability in terms of Fock states at the BS input we have

$$\begin{aligned} P_{11}^{\parallel}(n,m) &= \sum_{j=0}^{n}\sum_{k=0}^{m} |K_{\parallel}(n,m,j,k)|^2 \; p_{11}(j+k,\, n+m-j-k) \\ &= \sum_{j=0}^{n}\sum_{k=0}^{m} |K_{\parallel}(n,m,j,k)|^2 \; \left[1-(1-\eta_1)^{j+k}\right]\left[1-(1-\eta_2)^{n+m-j-k}\right] , \end{aligned} \tag{C.5}$$

where $K_{\parallel}(n,m,j,k)$ should be substituted with the factor from (C.2). For distinguishable inputs we find a similar expression for $P_{11}^{\perp}(n,m)$ using the factor $K_{\perp}(n,m,j,k)$ from (C.3). It is assumed that the detector at a given spatial output mode is equally sensitive to photons in both auxiliary modes, i.e. it detects the states $|k,\, j\rangle$ and $|j,\, k\rangle$ with equal probability. We are now in the position to formulate an expression for the different detection probabilities given a particular set of coherent input fields. The probability to generate a detection event in both detectors, given coherent input fields of amplitudes α and β, is

$$\mathcal{P}_{11}^{\parallel(\perp)}(\alpha,\beta) = \sum_{n=0}^{\infty}\sum_{m=0}^{\infty} e^{-|\alpha|^2-|\beta|^2}\frac{(\alpha^n\beta^m)^2}{n!\,m!}P_{11}^{\parallel(\perp)}(n,m)\,. \tag{C.6}$$

(Note that to distinguish the probability in (C.5), which is applicable to Fock states, from that in (C.6), which applies to coherent state inputs, we use P to denote the former and $\mathcal{P}$ for the latter.) This allows us to derive the visibility of the HOM interference on the two

detectors as

$$\mathcal{V}_{11}(\alpha,\beta,\eta_1,\eta_2,r) = \frac{\mathcal{P}_{11}^{\perp}(\alpha,\beta) - \mathcal{P}_{11}^{\parallel}(\alpha,\beta)}{\mathcal{P}_{11}^{\perp}(\alpha,\beta)}\,, \tag{C.7}$$

where we have spelled out the parameters that affect the value of the visibility. The quantity $\mathcal{V}_{11}$ is referred to as the *HOM visibility*.

Simplified model for HOM visibility

To gain some intuitive understanding of the way the HOM visibility is affected by the experimental parameters we resort to a couple of approximations. Firstly, we assume equal mean photon numbers at the inputs of the beam-splitter, $|\alpha|^2 = |\beta|^2 \equiv \mu$, the BS ratio to be 50:50 (i.e. $r = t = 1/\sqrt{2}$), and the detectors to have equal single photon detection probability $\eta_1 = \eta_2 \equiv \eta$. Secondly, since we normally work at very low mean photon numbers $\mu < 1$ only the first couple of terms of (C.1) need to be included. Specifically, we Taylor expand $e^{-\mu/2}$ and keep only terms in the sum up to 2^{nd} order in μ. Thus, for the coincidence detection events we get the probabilities

$$\mathcal{P}_{11}^{\parallel} = \eta^2 \frac{\mu^2}{2} \tag{C.8}$$

$$\mathcal{P}_{11}^{\perp} = \eta^2 \mu^2\,, \tag{C.9}$$

which results in a HOM visibility of

$$\mathcal{V}_{11} = \frac{1}{2}\,. \tag{C.10}$$

A key point is that the HOM visibility of 50% is independent of the mean photon number μ. This observation can be explained by noting that in this low order treatment the coincidences in the case of indistinguishable input modes stem mostly from events in which two photons are present at the same input, which occurs with probability $p_0p_2 + p_2p_0$. For distinguishable input modes the coincidences stem from all events that contain two photons at the input, i.e. $p_1p_1 + p_0p_2 + p_2p_0$. Since, according to (C.1), for coherent input states, all of these

probabilities scale in the same way with the mean photon number, their ratio, and thus the visibility of (C.7), is constant for all mean photon numbers.

Here we show the plots of coincidence count rates on which the few-photon values in Table 8.1 of the main text are based. We restate that coincidence count rates are proportional to coincidence probabilities by a factor that is given by the average experimental repetition rate. Moreover, when calculating the HOM visibility, only the relative probabilities or count rates in a measurement are important. In the experiments we change the mutual polarization, time separation, or frequency difference of the pulses at the BS (in the main text referred to as HOM-BS) input as explained in the Methods.

Deactivated memories

We present the data in order of the number of activated memories starting with none, i.e. pulses merely pass through attenuated to the BS. In Supplementary Figure C.1a) we show the coincidence counts as we vary the polarization difference of the pulses at the two inputs of the BS. Fitting the data to a sine function we obtain a visibility of $\mathcal{V} = 50.96 \pm 5.56\%$. In Supplementary Figure C.1b) we display the coincidence counts as we step the temporal separation between the pulses at the two inputs of the BS. The count rates for these measurements are generally higher than all the other count rates presented. This is because this data was acquired by looking at coincidences between the transmitted part of the probe pulses in the configuration of two active quantum memories (shown in Supplementary Figure C.3b)). Hence, the balancing of the mean photon number in the transmitted pulses done less meticulously, which is the most likely reason for the observed lower visibility of $\mathcal{V} = 42.43 \pm 2.27\%$ in this case.

Supplementary Figure C.1c) shows the coincidence count rates as function of the frequency

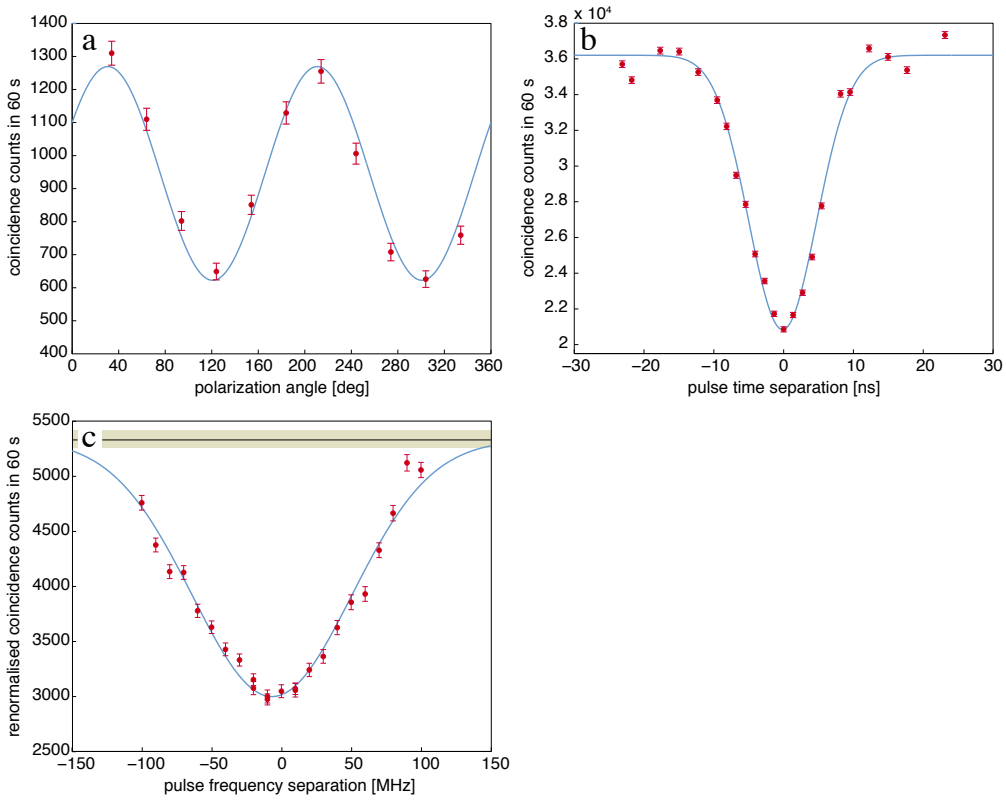

Figure C.1: **HOM interference with inactive memories.** HOM interference manifested in coincidence counts between BS outputs with inactive memories. a) Changing the polarization angle between the pulses yields a HOM visibility of $\mathcal{V} = 50.96 \pm 5.56\%$. b) Varying the temporal overlap of the pulses produces $\mathcal{V} = 42.43 \pm 2.27\%$. c) Altering the frequency overlap of the pulse spectra results in $\mathcal{V} = 43.72 \pm 1.70\%$. All error bars are calculated as the square-root of the total counts, corresponding to Poissonian counting statistics.

difference of the two pulses at the BS inputs. The horizontal line and surrounding shaded band shown in Supplementary Figure C.1c) – as well as in Supplementary Figure C.2c) – give the coincidence counts for completely distinguishable input photons as obtained by making the polarizations orthogonal. As noted in the Methods, it is necessary to resort to the polarization degree of freedom in order to make the pulses completely distinguishable. The visibility from the fit is noticeably lower than that obtained when we change the other degrees of freedom. There are two main reasons for this. The first is that, in order to generate pulses with different frequencies, we drive the AOM at the limits of its bandwidth. This, in turn, necessitates setting the RF drive signal amplitude high whereby the frequency purity of the signal is contaminated by higher-order harmonics. Although it is not expected

to change the maximal interference value occurring when the pulses are generated with the same modulation frequency, it will alter the shape of the interference as a function of the pulse frequency difference. Hence, the fitted Gaussian curve, assuming a Fourier limited pulse, may not correctly reproduce the actual frequency dependence of the interference. Indeed, the minimum coincidence rates consistently fall below the fitted curve. A second factor reducing the observed visibility is related to the need to adjust the AOM drive amplitude to balance the bandwidth limitation. The limited accuracy with which we are able to estimate the appropriate RF amplitude results in significant scattering of the coincidence counts due to variations in input pulse intensities. To amend this we have found that it is necessary to normalize the points to the count rates on the individual detectors, as indicated on the y-axis of plot Supplementary Figure C.2c. Unfortunately, the manifestation of the HOM interference in the single-detector count rates – which will be elaborated later – means that such a normalization procedure tends to reduce the visibility in the coincidence counts.

One active memory:

Next in line are the plots for the case in which only memory A is activated, while the other is left inactive. In Supplementary Figure C.2 we present the coincidence count rates when changing the same degrees of freedom as in case of both memories being inactive. Additionally, in Supplementary Figure C.2d, we plot the coincidence count rates when changing the storage time in the quantum memory.

Two active memories

Lastly, we present the plots for the case in which both memories are activated. Due to limitations in our current setup it is not possible to simultaneously generate two quantum memories with different storage times, and therefore we do not acquire a storage time scan when both memories are active. Furthermore, we skip the characterization with respect to

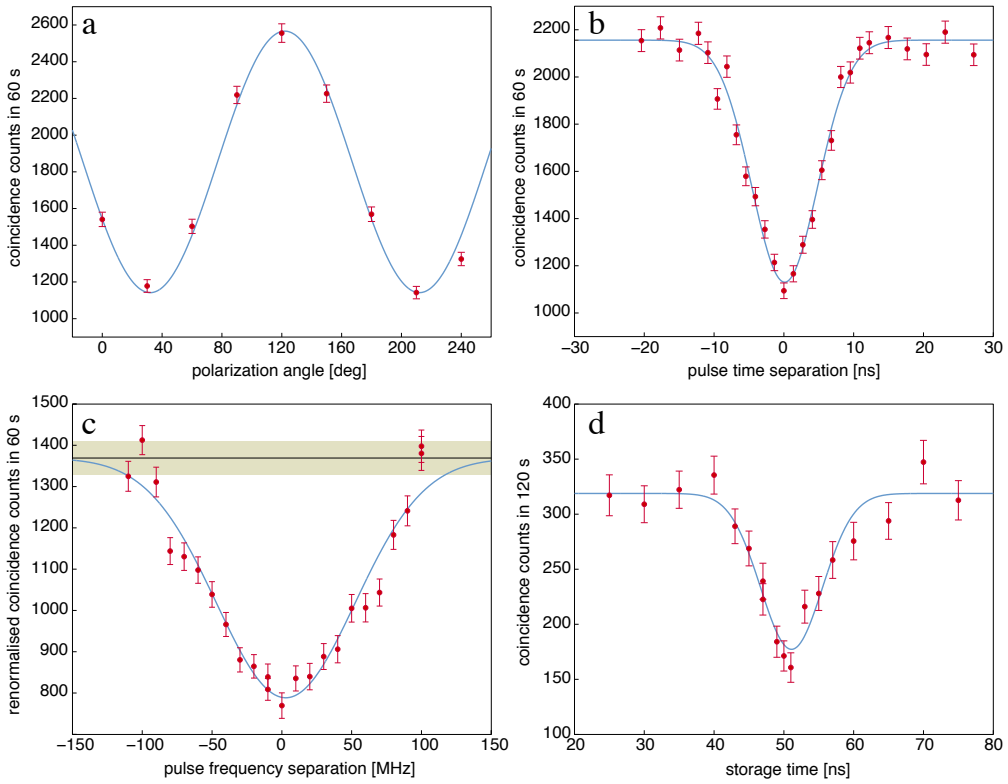

Figure C.2: **HOM interference with one active memory.** HOM interference manifested in coincidence counts between BS outputs with one active memory. a) Changing the polarization angle between the pulses yields a HOM visibility of $\mathcal{V} = 55.51 \pm 4.09\%$. b) Varying the temporal overlap of the pulses produces $\mathcal{V} = 47.57 \pm 2.96\%$. c) Altering the frequency overlap of the pulse spectra results in $\mathcal{V} = 42.40 \pm 3.51\%$. d) Varying the storage time of the quantum memory and thus the temporal overlap of the pulses yields $\mathcal{V} = 44.4 \pm 6.9\%$. All error bars are calculated as the square-root of the total counts, corresponding to Poissonian counting statistics.

the spectral degree of freedom. The coincidence count data for the remaining two degrees of freedom are plotted in Supplementary Figure C.3, which also includes the appropriate fits.

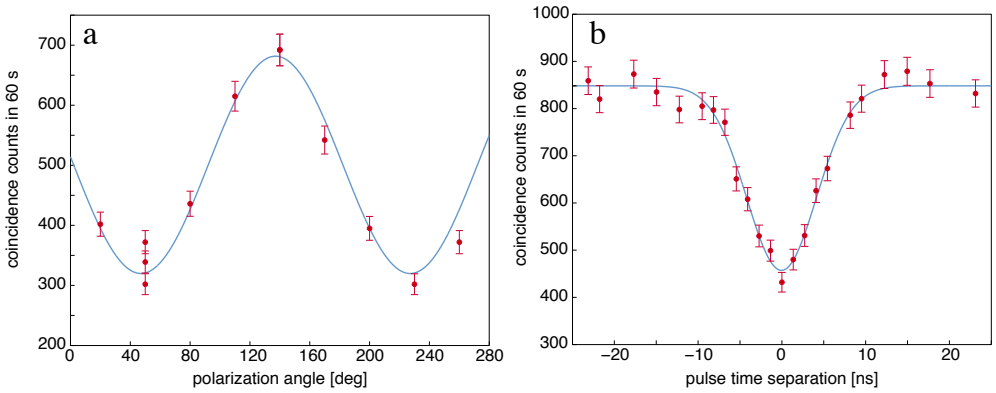

Figure C.3: **HOM interference with two active memories.** HOM interference manifested in coincidence counts between BS outputs with two active memories. a) Changing the polarization angle between the pulses yields a HOM visibility of $\mathcal{V} = (53.1 \pm 5.3)\%$. b) Varying the temporal overlap of the pulses produces $\mathcal{V} = (46.1 \pm 3.2)\%$. All error bars are calculated as the square-root of the total counts, corresponding to Poissonian counting statistics.

Two-photon interference in imperfectly prepared memories

In all our demonstrations of the HOM interference we consistently observe that the HOM visibility is close to the theoretical maximum for coherent states. Yet, it is important to realize that an improperly configured AFC quantum memory does alter a stored photon's wavefunction, resulting in imperfect HOM interference with a non-stored photon.

To support this claim we activate only memory A, whose performance we change by varying the bandwidth of the AFC, and interfere the recalled pulses with pulses directly transmitted through the deactivated memory B. As the AFC bandwidth decreases below that of the probe pulses, the AFC effectively acts as a bandpass filter for the stored photons and we thus expect the recalled pulses to be temporally broadened w.r.t. the original pulse. This is observed in the insert of Supplementary Figure C.4, which shows smoothed histograms of photon detection events as a function time. It is worth noting that the small bandwidth AFC also acts as a bandpass filter for the transmitted pulse by virtue of the different effective optical depths inside and outside the AFC. Thus the broadened transmitted pulse starts to

overlap with the echo for the narrow AFC bandwidth traces, as is also observed in the insert of Supplementary Figure C.4.

Another consequence of reducing the AFC bandwidth is that the overall efficiency of the quantum memory decreases, which causes an imbalance between the mean photon numbers at the HOM-BS inputs and thus reduces HOM interference visibility. We circumvent the change to the echo efficiency by adapting the mean photon number at the memory input so as to keep the mean photon number of the recalled pulse constant. With this remedial procedure, we assess the HOM visibility by changing the HOM-BS inputs from parallel to orthogonal polarizations for a series of different AFC bandwidths. The HOM visibility in Supplementary Figure C.4 is steady for bandwidths from around 100 MHz and up. However, below 100 MHz the visibility begins to drop significantly. The dashed line is a fit of the visibilities to a Gaussian function with full-width at half-maximum (FWHM) of $79 \pm 4\ MHz$. Note, that the reason for the visibility being limited to around 40% is solely that, for this measurement, we do not go through the usual careful optimization steps.

With these measurements we have illustrated how a quantum memory could alter the photonic wavefunction resulting in a reduced HOM interference visibility. A combination of spectral and temporal distortion of the photonic wavefunction is indeed a common type of perturbation by quantum memories.[2, 3] It is particularly worth noting that the gradient-echo memory (GEM) quantum memory protocol, though similar to the AFC protocol, imparts a frequency chirp to the recalled pulse[4]. If not corrected, this feature constitutes a perturbation of the wavefunction of the recalled pulse, which may render it unsuitable for applications relying on two-photon interference.

We also evaluate the effect of the two-photon interference on the counts registered by a single detector. This is easily done by amending the detection probability to the case of

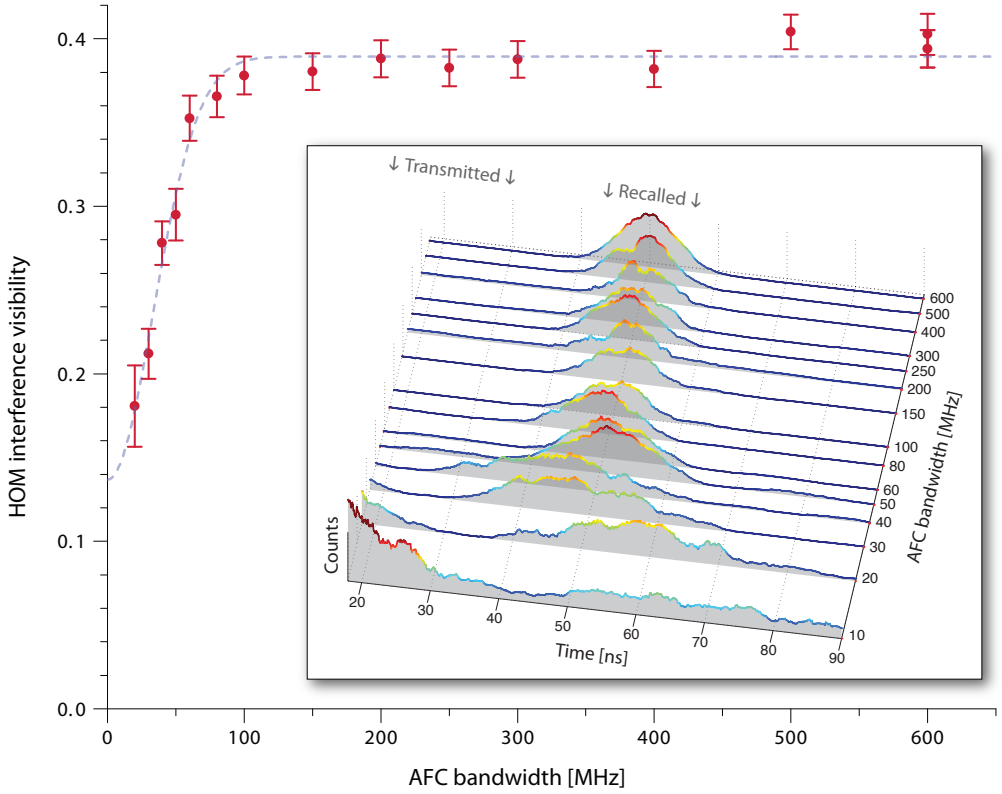

Figure C.4: **HOM interference for imperfectly prepared memory.** HOM interference visibility if HOM-BS input pulses are recalled from AFCs with varying bandwidths. Insert: Histograms of recalled pulse detection times for different AFC bandwidths clearly showing broadening of recalled (and transmitted) pulses for bandwidths below 100 ns. All error bars are calculated as the square-root of the total counts, corresponding to Poissonian counting statistics.

one detection event in one detector and any number of events x (i.e. $x = 0, 1$) in the other detector. We arrive at

$$p_{1x}(n, m) = 1 - (1 - \eta_1)^n \,. \tag{C.11}$$

This expression can be inserted into (C.5) to calculate $P_{1x}^{\parallel(\perp)}(n, m)$, which, through (C.6), gives us $\mathcal{P}_{1x}^{\parallel(\perp)}(\alpha, \beta)$, and from which the *single-detector visibility* $\mathcal{V}_{1x}$ is defined analogous to (C.7).

We can formulate a simplified expression by using the same approximations as in the case

of coincidence detections:

$$\mathcal{P}_{1x}^{\parallel} = \eta\mu + \eta\left(2 - \frac{3\eta}{4}\right)\mu^2 \tag{C.12}$$

$$\mathcal{P}_{1x}^{\perp} = \eta\mu + \eta\left(2 - \frac{\eta}{2}\right)\mu^2\,, \tag{C.13}$$

from which we get the single-detector visibility

$$\mathcal{V}_{1\mathrm{x}} = \frac{\eta\mu}{4 + 2(4-\eta)\mu}\,. \tag{C.14}$$

In the limit of low detector efficiency, $\mathcal{V}_{1\mathrm{x}} \approx 0$, since, in that case, the probability of detecting two photons impinging on the detector is simply twice that of detecting one. This nulls the limitation that only a single detection event can be generated per pulse. Furthermore, the single-detector visibility also goes to zero for very low mean photon numbers. In this case it is very unlikely to have two photons either at the *same* or at *different* input ports of the BS, hence most of the single detector counts stem from single photons from either one or the other input of the BS. It is interesting to note that if η is known for a detector, then, from observing the single-detector visibility (see (C.14)), it is in principle possible to estimate the mean photon number per pulse μ.

Another important consequence of the manifestation of two-photon interference in the single-detector counts is that the single-detector counts cannot generally be used to normalize the coincidence counts w.r.t. fluctuations in the input pulse intensities. Only for detectors with low detection efficiency or very low mean photon numbers, in which case $\mathcal{V}_{1\mathrm{x}} \approx 0$, is this normalization possible.

Experimental results on HOM interference manifested in single-detector counts

First, in Supplementary Figure C.5, we present the single-detector counts corresponding to the coincidence counts depicted in Supplementary Figure C.2a,b.

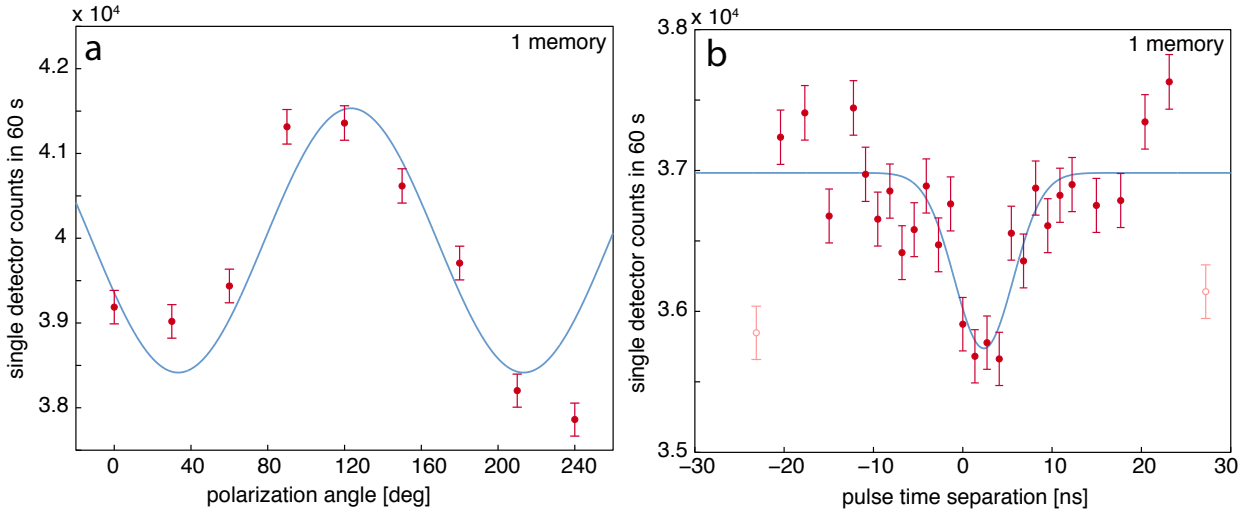

Figure C.5: **Experimental HOM interference is single detector counts for one active memory.** HOM interference manifested in single-detector counts in the case of one active quantum memory when changing a) polarization and b) time difference between pulses at BS input. For the polarization scan in a) we find $\mathcal{V}_{1x} = (7.51 \pm 3.80)\%$ and for the time scan in b) we get $\mathcal{V}_{1x} = (7.75 \pm 3.25)\%$. For this measurement we only recorded the single-detector counts from Si-APD 1. All error bars are calculated as the square-root of the total counts, corresponding to Poissonian counting statistics.

In the case where we vary the polarization and time separation we see a clear change in the single-detector counts, which, moreover, is evidently correlated with the change in coincidence counts. The count variation due to the two-photon interference is somewhat masked by the single-detector count scatter, which is due to intensity fluctuations mainly in the light going through the 10 km delay line. We fit the data in Supplementary Figs. C.5a and b with a sine and Gaussian function, respectively. For the former we find a mean photon number of $\mu = 0.52$ while from the latter we estimate $\mu = 0.54$. From the number of single-detector counts there is some evidence to conclude that the light intensity is about 15% higher. To

this should be added about 25% uncertainty for the intensity at the BS w.r.t. the intensity at the detector due to variation in the loss in the fibre mating sleeves. Finally, the scatter of the counts makes the fits themselves rather uncertain. Nevertheless, the mere fact that the two-photon interference is manifested in the single-detector counts validates the order of magnitude of the mean photon number, as depicted in Supplementary Figure C.6.

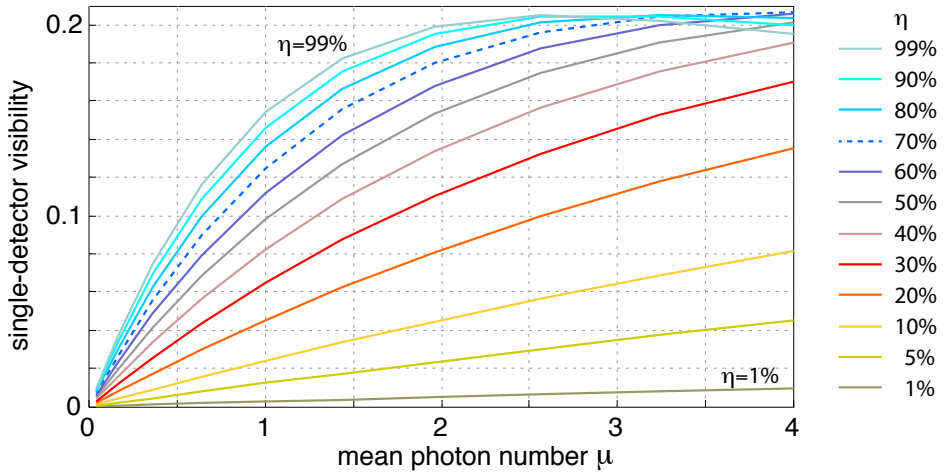

Figure C.6: **Theoretical visibility of HOM interference is single detector counts.** Plots of single-detector visibility as a function of the mean photon number for detectors with a range of single photon detection probabilities η. The $\eta = 70\%$ trace, highlighted with a dashed line, corresponds approximately to our detectors, which have $65\% \leq \eta \leq 75\%$.

Supplementary Figure C.7 depicts the single-detector counts corresponding to the coincidence counts depicted in Supplementary Figure C.3a,b. Again, from fitting the appropriate functions to the polarization and time data yields visibilities around 7%, corresponding to mean photon numbers of around $\mu = 0.5$.

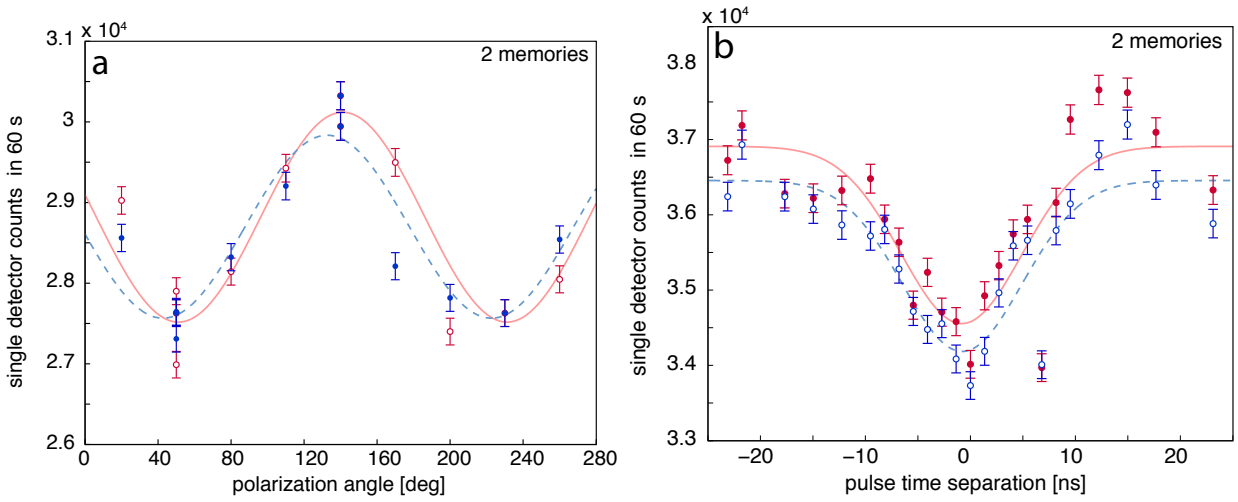

Figure C.7: **Experimental HOM interference is single detector counts for two active memories.** HOM interference manifested in single-detector counts in the case of two active quantum memories when changing a) polarization and b) time difference between pulses at BS input. For the polarization scan in a) we find $\mathcal{V}_{1x} = (8.64 \pm 2.50)\%$ and $\mathcal{V}_{1x} = (7.60 \pm 2.36)\%$ for Si-APD 1 and 2, respectively. For the time scan in b) we measure $\mathcal{V}_{1x} = (6.38 \pm 2.01)\%$ and $\mathcal{V}_{1x} = (6.23 \pm 1.61)\%$ for Si-APD 1 and 2, respectively. All error bars are calculated as the square-root of the total counts, corresponding to Poissonian counting statistics.

Bell state measurement

In this section we derive an analytical expression for the coincidence count rates corresponding to projections onto the $|\psi^-\rangle$ Bell state for time-bin qubits detected by the two detectors at the output of the HOM-BS. To that end, we will introduce a number of approximations as we did previously in order to calculate the HOM interference in the coincidence counts. In the limit of low mean photon numbers, two coherent states impinging onto the two inputs of a 50:50 BS can be represented in terms of Fock states as

$$\begin{aligned} |\psi\rangle_{ab} &= \sqrt{p(1,1)}|11\rangle_{a,b} + \sqrt{p(2,0)}|20\rangle_{a,b} + \sqrt{p(0,2)}|02\rangle_{a,b} \\ &= \left(\sqrt{p(1,1)}(\hat{a}^\dagger \otimes \hat{b}^\dagger) + \frac{1}{\sqrt{2!}}\left[\sqrt{p(2,0)}((\hat{a}^\dagger)^2 \otimes I) + \sqrt{p(0,2)}(I \otimes (\hat{b}^\dagger)^2)\right]\right)|00\rangle_{a,b} \quad , \end{aligned} \tag{C.15}$$

where the subscripts on the state vector refer to the order of listing the input modes, i.e.

$|00\rangle_{a,b} \equiv |0\rangle_a \otimes |0\rangle_b$. The factors written as $p(n,m)$ denote the probability of having n and m photons in mode a and b, and are given by $p(n,m) = |({}_a\langle n| \otimes_b \langle m|)(|\alpha\rangle_a \otimes |\beta\rangle_b)|^2 = \frac{e^{-(|\alpha|^2+|\beta|^2)}}{n!m!}(|\alpha|^2)^n(|\beta|^2)^m$. Stemming from the low mean photon number assumption, we do not include terms with more than two photons. Assuming that our detectors are noiseless, terms with a total of one or no photons are also left out as they cannot generate any coincidence counts.

For a time-bin qubit, the Fock state is created in a superposition of two temporal modes, i.e., an *early* (e) and a *late* (l) mode, by the creation operators for the spatial input mode $x^\dagger$ ($x^\dagger = a^\dagger, b^\dagger$) of the beam-splitter, as

$$(\hat{x}^\dagger)^n|0\rangle_x \rightarrow \left[\cos\Big(\frac{\theta_x}{2}\Big)\ \hat{x}_e^\dagger \otimes I + e^{i\phi_x}\sin\Big(\frac{\theta_x}{2}\Big)\ I \otimes \hat{x}_l^\dagger\right]^n |00\rangle_{xe,xl} \quad , \tag{C.16}$$

where $\cos\big(\frac{\theta_x}{2}\big)$ and $\sin\big(\frac{\theta_x}{2}\big)$ are the amplitudes of, and ϕ_x is the relative phase between, the two temporal modes composing the time-bin qubit. The subsript xe refers to the early time-bin of the spatial mode x and similarly for xl. Note, that we sometimes simplify the notation for the time-bin qubit states as $|e\rangle_x \equiv |10\rangle_{xe,xl} = (\hat{x}_e^\dagger \otimes I)|00\rangle_{xe,xl}$. If we insert the expression in (C.16) in place of the $\hat{a}$ and $\hat{b}$ operators in (C.15) we get the expression for the wavefunction $|\psi(\theta_a,\phi_a,\theta_b,\phi_b)\rangle_{ab}$ for time-bin qubits at the HOM-BS inputs. We split this expression into the various contributions given in (C.15)

$$
\begin{aligned}
(\hat{a}^\dagger \otimes \hat{b}^\dagger)|00\rangle_{ab} \rightarrow \frac{1}{2}\Bigg[& \left(ie^{i\phi_b}\cos\left(\frac{\theta_a}{2}\right)\sin\left(\frac{\theta_b}{2}\right) + ie^{i\phi_a}\sin\left(\frac{\theta_a}{2}\right)\cos\left(\frac{\theta_b}{2}\right)\right)\left(\hat{c}_e^\dagger\hat{c}_l^\dagger + \hat{d}_e^\dagger\hat{d}_l^\dagger\right) \\
& + \left(e^{i\phi_b}\cos\left(\frac{\theta_a}{2}\right)\sin\left(\frac{\theta_b}{2}\right) - e^{i\phi_a}\sin\left(\frac{\theta_a}{2}\right)\cos\left(\frac{\theta_b}{2}\right)\right)\left(\hat{c}_e^\dagger\hat{d}_l^\dagger - \hat{c}_e^\dagger\hat{d}_l^\dagger\right) \\
& + ie^{i(\phi_a+\phi_b)}\sin\left(\frac{\theta_a}{2}\right)\sin\left(\frac{\theta_b}{2}\right)\left((\hat{c}_l^\dagger)^2 + (\hat{d}_l^\dagger)^2\right) \\
& + i\cos\left(\frac{\theta_a}{2}\right)\cos\left(\frac{\theta_b}{2}\right)\left((\hat{c}_e^\dagger)^2 + (\hat{d}_e^\dagger)^2\right)\Bigg]|0000\rangle_{ce,cl,de,dl}
\end{aligned} \tag{C.17}
$$

$$
\begin{aligned}
((\hat{a}^\dagger)^2 \otimes I)|00\rangle_{ab} \rightarrow \frac{1}{2}\Bigg[& 2e^{i\phi_a}\cos\left(\frac{\theta_a}{2}\right)\sin\left(\frac{\theta_a}{2}\right)\left(\hat{c}_e^\dagger\hat{c}_l^\dagger - \hat{d}_e^\dagger\hat{d}_l^\dagger\right) \\
& + i2e^{i\phi_a}\cos\left(\frac{\theta_a}{2}\right)\sin\left(\frac{\theta_a}{2}\right)\left(\hat{c}_e^\dagger\hat{d}_l^\dagger + \hat{c}_l^\dagger\hat{d}_e^\dagger\right) \\
& + \cos^2\left(\frac{\theta_a}{2}\right)\left((\hat{c}_e^\dagger)^2 + i2\hat{c}_e^\dagger\hat{d}_e^\dagger - (\hat{d}_e^\dagger)^2\right) \\
& + e^{i2\phi_a}\sin^2\left(\frac{\theta_a}{2}\right)\left((\hat{c}_l^\dagger)^2 + i2\hat{c}_l^\dagger\hat{d}_l^\dagger - (\hat{d}_l^\dagger)^2\right)\Bigg]|0000\rangle_{ce,cl,de,dl}
\end{aligned} \tag{C.18}
$$

and similarly for $(I \otimes (\hat{b}^\dagger)^2)|00\rangle_{ab}$. Again, the subscripts on the state vector refer to the order of listing the temporal and spatial modes, e.g. *ce* labels the early bin of the spatial output mode *c*.

We will look for coincidence detection events that correspond to projections onto the Bell state $|\psi_-\rangle_{cd} = \frac{1}{\sqrt{2}}(\hat{c}_e^\dagger\hat{d}_l^\dagger - \hat{c}_l^\dagger\hat{d}_e^\dagger)|0000\rangle_{ce,cl,de,dl}$. Such projections correspond to a detection event in the early time-bin in one detector followed by a detection event in the late time-bin in the other detector. This projection occurs with a probability $\mathcal{P}_-(\theta_a, \phi_a, \theta_b, \phi_b) = |\,{}_{cd}\langle\psi_-|\psi(\theta_a, \phi_a, \theta_b, \phi_b)\rangle_{cd}|^2$, which can be computed by combining (C.17) and (C.18) with (C.15). Assuming equal mean photon numbers at the two inputs $|\alpha|^2 = |\beta|^2 \equiv \mu$ and averaging over the coherent state phases, i.e. the complex angle between α and β, we get the expression

$$\mathcal{P}_-(\theta_a,\phi_a,\theta_b,\phi_b) \propto \frac{\mu^2 e^{-2\mu}}{8}\Bigg[4\sin^2\!\left(\frac{\theta_a+\theta_b}{2}\right) + \sin^2\big(\theta_a\big) + \sin^2\big(\theta_b\big) \\ - 2\sin\big(\theta_a\big)\sin\big(\theta_b\big)\Big(1+\cos\big(\phi_a-\phi_b\big)\Big)\Bigg]\,. \tag{C.19}$$

With this we are able to calculate the probabilities of projection onto $|\psi^-\rangle$ for different combinations of qubits at the two BS inputs, i.e. for different choices of the angles θ_x and ϕ_x. In turn, this allows us to calculate the $|\psi^-\rangle$ Bell-state measurement error rate as

$$e \equiv \frac{\mathcal{P}_-^{\parallel}}{\mathcal{P}_-^{\parallel}+\mathcal{P}_-^{\perp}}\,, \tag{C.20}$$

where $\mathcal{P}_-^{\parallel}$ is the projection probability when the two input qubit states are identical, i.e. $\phi_a=\phi_b$ and $\theta_a=\theta_b$, while $\mathcal{P}_-^{\perp}$ is the projection probability for two orthogonal input qubit states. This is also defined in terms of count rates in (8.3) in the main text. We will now treat a number of relevant cases.

Firstly, we compute expected error rates in the case of $\phi_a=\phi_b=0$. Using the simplified notation this corresponds to the case were the input qubit states are of the form $|\psi\rangle=\cos\left(\frac{\theta_x}{2}\right)|e\rangle+\sin\left(\frac{\theta_x}{2}\right)|l\rangle$. When depicted on the Bloch sphere these qubits span the xz-plane. Using (C.19) we compute the projection probability as

$$\mathcal{P}_-(\theta_a,0,\theta_b,0) \propto \frac{\mu^2 e^{-2\mu}}{8}\left[4\sin^2\!\left(\frac{\theta_a+\theta_b}{2}\right) + \sin^2\big(\theta_a\big) + \sin^2\big(\theta_b\big) - 4\sin\big(\theta_a\big)\sin\big(\theta_b\big)\right]\,. \tag{C.21}$$

We are interested in the probability $\mathcal{P}_-^{\parallel}$ for the case in which the input qubits are parallel ($\theta_a=\theta_b=0$) and $\mathcal{P}_-^{\perp}$ for the case in which the input qubit states are orthogonal ($\theta_a=$

$0, \theta_b = \pi$). Simple algebra gives $\mathcal{P}_-^{\parallel} = 0$ and $\mathcal{P}_-^{\perp} = \frac{\mu^2 e^{-2\mu}}{2}$, thereby providing the theoretical bound of the error rate to be $e_{e/l}^{(\mathrm{att})} = 0$.

The case of $\theta_a = \theta_b = \pi/2$ is secondly considered. In this case the two input qubits are in equal superpositions of early and late bins, that is of the form $|\psi\rangle = \frac{1}{\sqrt{2}}\big(|e\rangle + e^{i\phi_x}|l\rangle\big)$. On the Bloch sphere these are qubits that lie in the xy-plane. In this case we compute

$$\mathcal{P}_-(\pi/2, \phi_a, \pi/2, \phi_b) \propto \frac{\mu^2 e^{-2\mu}}{4}\big(2 - \cos(\phi_a - \phi_b)\big)\,, \tag{C.22}$$

Thus the $|\psi^-\rangle$ Bell-state projection probability is smallest – but nonzero – when $\phi_a - \phi_b = 0$, i.e. the qubit states are parallel, and largest when the phases differ by π, i.e. the qubit states are orthogonal. Using (C.22), we get $\mathcal{P}_-^{\parallel} = \frac{\mu^2 e^{-2\mu}}{4}$ and $\mathcal{P}_-^{\perp} = \frac{3\mu^2 e^{-2\mu}}{4}$. Inserting these values for $\mathcal{P}_-^{\parallel}$ and $\mathcal{P}_-^{\perp}$ into (C.20) results in an expected error rate of $e_{+/-}^{(\mathrm{att})} = 0.25$.

Bounds for attenuated laser pulses stored in quantum and classical memories

We now compare the performance of our Bell-state measurement to a number of relevant bounds assuming always that any imperfections arise from the imperfect storage of the photon in the memory. We will derive bounds to the error rate in the case of one qubit being stored in either a classical memory (CM) or quantum memory (QM). To accommodate this scenario we assume that the memory performs the following operation $|\psi\rangle\langle\psi| \rightarrow F|\psi\rangle\langle\psi| + (1-F)|\psi^\perp\rangle\langle\psi^\perp|$, where F denotes the fidelity of the stored state and $|\psi^\perp\rangle$ is the state orthogonal to $|\psi\rangle$. For a quantum memory, $F^{\mathrm{QM}} = 1$ whereas for a classical memory $F^{\mathrm{CM}} = 2/3$ [**??**]. The latter bound strictly only applies to the storage of single-photon states, whereas, for coherent states, the bound is higher[??,??]. One can imagine

an optimal classical storage approach that is optimized with respect to the mean number of photons per qubit. This optimal storage approach derives additional information about an input state by measuring individual photons from signals containing multiple photons in different bases. Furthermore, if the quantum memory features limited efficiency, then the best classical memory would selectively discard signals containing one (or few) photons and measure only signals containing large numbers of photons. This would allow keeping the total recall efficiency unaffected while maximizing the fidelity. For the Bell-state measurements we used a mean photon number per pulse of 0.6 and together with 0.3% system efficiency (1.5% memory and 20% waveguide coupling efficiencies) we compute the fidelity for an optimal classical storage approach $\tilde{F}^{\mathrm{CM}} = 0.841$.

With the transformation $\mathcal{P}_-^{\parallel} \to F\mathcal{P}_-^{\parallel} + (1-F)\mathcal{P}_-^{\perp}$ and likewise for $\mathcal{P}_-^{\perp}$ we can express the error rate expected after imperfect storage of one of the pulses partaking in the Bell-state measurement:

$$e = \frac{F\mathcal{P}_-^{\parallel} + (1-F)\mathcal{P}_-^{\perp}}{\mathcal{P}_-^{\parallel} + \mathcal{P}_-^{\perp}}\,, \tag{C.23}$$

where in this case the probabilities $\mathcal{P}_-^{\parallel}$ and $\mathcal{P}_-^{\perp}$ refer to those expected without the memory. Since the expected values for $\mathcal{P}_-^{\parallel}$ and $\mathcal{P}_-^{\perp}$ differ between the e/l and $+/-$ bases we treat them separately.

Beginning with the e/l basis we use (C.23) with the values from (C.21) to derive a bound for the error rate of the Bell-state measurement for one of the two qubits being recalled from a quantum or a classical memory. We find that $e_{e/l}^{(\mathrm{att})} = 1 - F$, and hence we establish the three bounds $e_{e/l}^{(\mathrm{att,QM})} = 0$, $e_{e/l}^{(\mathrm{att,CM})} = 0.333$, and $\tilde{e}_{e/l}^{(\mathrm{att,CM})} = 0.159$ for the quantum ($F^{\mathrm{QM}} = 1$), classical ($F^{\mathrm{CM}} = 2/3$), and optimal classical ($\tilde{F}^{\mathrm{CM}} = 0.841$) storage approaches, respectively.

We now turn to the +/− basis. For attenuated laser pulses we insert into (C.23) the values $\mathcal{P}_-^{\parallel} = \frac{\mu^2 e^{-2\mu}}{4}$ and $\mathcal{P}_-^{\perp} = \frac{3\mu^2 e^{-2\mu}}{4}$ computed from (C.22), which enables us to relate the error rate to the memory fidelity as $e_{+/-} = (3 - 2F)/4$. Thus, one obtains the theoretical lower bound on the error rate $e_{+/-}^{(\mathrm{att,QM})} = 0.250$ for an ideal quantum memory, $e_{+/-}^{(\mathrm{att,CM})} = 0.417$ with a classical storage device, and $\tilde{e}_{+/-}^{(\mathrm{att,CM})} = 0.330$ with an optimal classical storage device.

Bounds for single photons stored in quantum and classical memories

Although we do not use single photon sources for the experiments reported here, it is interesting to determine how well our results measure up to those that could have been obtained if single photon sources had been employed. In the following we will derive the error rate for the Bell-state measurement using qubits encoded into single photons. To this end we step back to (C.15), and note that for single photon sources all probabilities are 0 except for $p(1,1)$, which describes the probability of having a single photon at each BS input. Thus, in the output state we only need to keep the terms from (C.17), which in turn means that the Bell-state projection probability can be written as

$$P_-(\theta_a, \phi_a, \theta_b, \phi_b) \propto \frac{1}{4}\left[\sin^2\left(\frac{\theta_a + \theta_b}{2}\right) + \sin^2\left(\frac{\theta_a - \theta_b}{2}\right) - \sin\big(\theta_a\big)\sin\big(\theta_b\big)\cos\big(\phi_a - \phi_b\big)\right]. \tag{C.24}$$

It is easily seen that for any two parallel input qubit states ($\theta_a = \theta_b$ and $\phi_a = \phi_b$) we get $P_-^{\parallel} = 0$. Therefore, irrespective of the projection probability for orthogonal input qubit states the expected error rate is always $e^{(\mathrm{sing})} = 0$, where *sing* identifies this value as belonging to the single photon case.

Experiments at mean photon numbers above one

In this final section we will explore in greater detail the HOM interference dependence on the angle $\phi_a - \phi_b$ between a set of equal superposition qubit states $|\psi\rangle_x = \frac{1}{\sqrt{2}}\big(|e\rangle + e^{i\phi_x}|l\rangle\big)$, which, in line with the preceding sections, belong to the $+/-$ basis. According to (C.22) the coincidence count rates vary as function of $\cos\big(\phi_a - \phi_b\big)$. In Supplementary Figure C.8 we show measured coincidence count rates as a function of $\phi_a - \phi_b$ for a mean photon number per qubit before the memory of around 20. As expected the coincidence detection probability reaches its maximum $\mathcal{P}_-^{\perp}$ when two input qubits are orthogonal ($\phi_a - \phi_b = \pi$) and when they are identical ($\phi_a - \phi_b = 0$) it reaches a minimum $\mathcal{P}_-^{\parallel}$. It is natural to define a Bell-state measurement visibility as

$$\mathcal{V} = \frac{\mathcal{P}_-^{\perp} - \mathcal{P}_-^{\parallel}}{\mathcal{P}_-^{\perp}} \tag{C.25}$$

analogous to (8.1) in the main text. Using values obtained from a cosine fit to the data in Supplementary Figure C.8 yields $\mathcal{V}_{+/-}^{\text{exp}} = (62.9 \pm 5.2)\%$. Comparing (C.25) with (C.20) it is easily seen that $\mathcal{V}$ and e are related as $e = (1 - \mathcal{V}_{+/-})/(2 - \mathcal{V}_{+/-})$. We can then use the expected error rates to find the corresponding Bell-state measurement visibilities. Using $e_{+/-}^{att} = 0.25$ we get a theoretical value $\mathcal{V}_{+/-}^{\text{att}} = 66.7\%$. In conclusion, our experimental Bell-state measurement visibility is only slightly below and within the experimental error actually equal to the expected value.

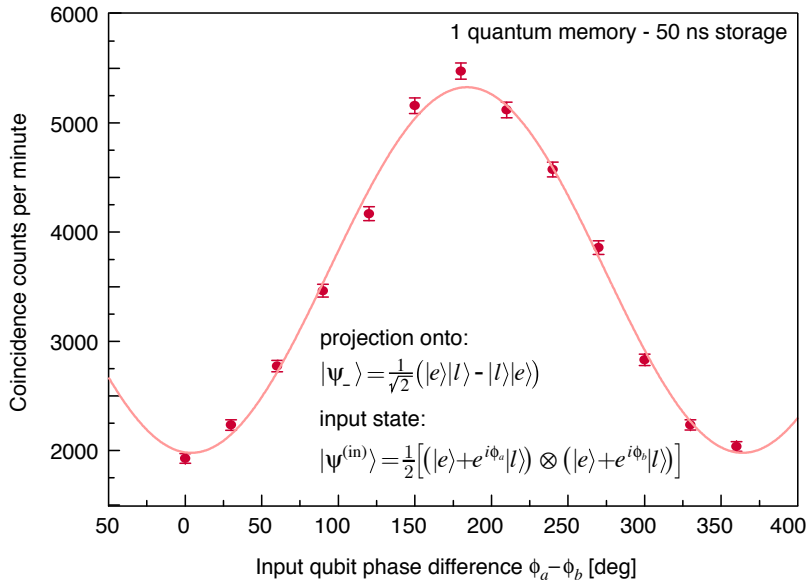

Figure C.8: **Bell state projection rate.** Rate of projection of pairs of time-bin qubits with relative phase $\phi_a - \phi_b$ onto $|\psi^-\rangle$. Each data point was acquired over 60 s. All error bars are calculated as the square-root of the total counts, corresponding to Poissonian counting statistics.

Bibliography

[1] Rarity, J. G., Tapster, P. R. & Loudon, R. Non-classical interference between independent sources. *Journal of Optics B: Quantum and Semiclassical Optics* **7**, S171 (2005).

[2] Chaneliere, T. *et al.* Storage and retrieval of single photons transmitted between remote quantum memories. *Nature* **438**, 833–836 (2005).

[3] Eisaman, M. D. *et al.* Electromagnetically induced transparency with tunable single-photon pulses. *Nature* **438**, 837–841 (2005).

[4] Moiseev, S. A. & Arslanov, N. M. Efficiency and fidelity of photon-echo quantum memory in an atomic system with longitudinal inhomogeneous broadening. *Phys. Rev. A* **78**, 023803 (2008).